Scanning Tunneling Microscopy and Luminescence of Individual Nanostructures

THÈSE N^{O} 4969 (2011)

PRÉSENTÉE LE 31 MARS 2011

À LA FACULTÉ SCIENCES DE BASE
LABORATOIRE DE SCIENCE À L'ÉCHELLE NANOMÉTRIQUE
PROGRAMME DOCTORAL EN PHYSIQUE

ÉCOLE POLYTECHNIQUE FÉDÉRALE DE LAUSANNE

POUR L'OBTENTION DU GRADE DE DOCTEUR ÈS SCIENCES

PAR

Theresa LUTZ

acceptée sur proposition du jury:

Prof. R. Schaller, président du jury
Prof. K. Kern, directeur de thèse
Prof. A. Fontcuberta i Morral, rapporteur
Prof. A. Mews, rapporteur
Prof. M. Morgenstern, rapporteur

ÉCOLE POLYTECHNIQUE
FÉDÉRALE DE LAUSANNE

Suisse
2011

Abstract

A detailed investigation and characterization of the local properties of individual nanoscopic structures is of great importance for the understanding of novel physical phenomena at the nanoscale as well as for the assessment of their possible use in future applications. A unique tool for the study of such structures are scanning probe methods. These methods do not only allow to obtain atomic scale information in both topographic and spectroscopic measurements at surfaces, but can also be employed for example to stimulate local photon emission. In this thesis the growth mechanism of inorganic and organic semiconductor nanostructures and the relation between their local structure and their electronic and optical properties is investigated by scanning probe techniques.

In the first part of this thesis, the growth as well as the local electronic and morphologic properties of InAs/GaAs(001) quantum dots grown by molecular beam epitaxy are described. The recorded spectra show evidence of the discretization of the density of states that can be attributed to the zero dimensional confinement of charge carriers to the quantum dots. Moreover, the shape evolution of the quantum dots during the controlled removal of material through an in situ etching gas is studied. High resolution topographic images reveal that hereby an island shape transition takes place. This shape evolution is found to be the reverse of the shape evolution that typically takes place during the growth, indicating that thermodynamic factors play an important role during the growth process and the etching process. In addition, the mechanism of the material removal from the quantum dots is investigated in detail by the analysis of the size evolution of the islands as a function of the nominal amount of etched material.

The second part of this thesis is dedicated to the study of individual CdSe nanowires grown by the solution-liquid-solid approach. These nanowires consist of small alternating sections of wurtzite and zincblende lattice structures. This structural arrangement also leads to an alternating electronic structure in the form of a type II band alignment along the long axis of the nanowires. The local electronic properties of the nanowires are analyzed by scanning tunneling spectroscopy. Tunneling current induced luminescence spectra from individual nanowires are acquired by the injection of holes and electrons and their subsequent radiative recombination. In contrast to previous studies on similar systems, the coupling of tip induced plasmons to the radiation process is not required. The shape and the position of the luminescence spectra is compared to photoluminescence spectra and Raman measurements. The

photon energy is found to decrease with increasing wire diameter indicating quantum confinement of the charge carriers to the wire. The bulk bandgap, that can be extrapolated from the energy vs. diameter dependence of the emission peaks, indicates that the photons are emitted from zincblende type CdSe sections. Moreover, the diameter dependence reveals that the emission stems from carriers that are confined to quantum dot like parts of the wires. The lack of light emission from the wurtzite type segments is also reflected in the appearance of non-luminescent regions in the NW as shown by spatially resolved light intensity maps. Possible mechanisms for the light excitation are discussed.
The investigation of single molecules of the luminescent organic emitter tris-(2-phenylpyridine)iridium(III) ($Ir(ppy)_3$) is the topic of the last part of this thesis. To this end, $Ir(ppy)_3$ molecules are deposited onto metal substrates and different types of thin insulating layers. Besides their structural and electronic characterization, the optical properties of single molecules are studied by tunneling current induced luminescence. No intrinsic light emission originating from the molecules can be observed neither on metal substrates nor on thin insulating layers. This indicates that in these systems, the molecules are still not sufficiently decoupled from the underlying metallic substrate. Preliminary results of tunneling current induced luminescence measurements of $Ir(ppy)_3$ molecules on multilayers of C_{60} show great promise for exciting light emission on single molecules.

Keywords: Scanning Probe Microscopy, Tunneling Current Induced Luminescence, InAs/GaAs(001) Quantum Dots, III-V Semiconductors, Self-Organized Growth, CdSe Nanowires, II-VI Semiconductors, $Ir(ppy)_3$, Iridium Compounds, Organic Semiconductors

Zusammenfassung

Die umfassende Untersuchung und Charakterisierung der lokalen Eigenschaften von einzelnen Nanostrukturen ist von großer Bedeutung für das Verständnis neuer physikalischer Phänomene auf der Nanoskala sowie um ihren möglichen Nutzen für zukünftige Anwendungen einschätzen zu können. Ein einzigartiges Instrument für die Untersuchung solcher Strukturen sind Rastersondenmethoden. Diese Methoden erlauben es nicht nur Informationen auf der atomaren Skala in topographischen sowie spektroskopischen Messungen an Oberflächen zu erhalten, sondern können beispielsweise auch dafür verwendet werden die lokale Emission von Photonen anzuregen. Die vorliegende Doktorarbeit beschäftigt sich mit dem Wachstumsmechanismus von inorganischen und organischen Halbleiternanostrukturen. Zudem wird der Zusammenhang der lokalen Struktur und der elektronischen und optischen Eigenschaften dieser Strukturen mit Rastersondentechniken untersucht.
Im ersten Teil dieser Arbeit sind das Wachstum sowie die lokalen elektronischen und morphologischen Eigenschaften von Molekularstrahlepitaxie gewachsenen InAs/GaAs(001) Quantenpunkten beschrieben. Die Diskretisierung der Zustandsdichte auf Grund der null-dimensionalen Einschränkung der Ladungsträger in den Quantenpunkten kann aus den Messergebnissen abgeleitet werden. Zudem wird die morphologische Entwicklung der Quantenpunkte, während dem kontrollierten Entfernen von Material durch ein in-situ Ätzgas, untersucht. Hochaufgelöste topographische Aufnahmen zeigen, dass dabei eine Transformation der Inselform stattfindet. Es stellt sich heraus, dass die Entwicklung der Inselform umgekehrt abläuft als die, die typischerweise während des Wachstums auftritt. Das zeigt, dass der Wachstumsprozess, als auch der Ätzprozess, stark von thermodynamischen Faktoren bestimmt wird. Des Weiteren wird der Mechanismus des Materialabtrags von den Quantenpunkten im Detail untersucht. Dies geschieht durch die Analyse der Größenentwicklung der Quantenpunkte als Funktion der nominellen Menge des abgetragenen Materials.
Der zweite Teil dieser Doktorarbeit ist der Studie einzelner CdSe Nanodrähte gewidmet, die mit dem sogenannten ‘solution-liquid-solid’ Verfahren hergestellt worden sind. Diese Nanodrähte bestehen aus alternierenden Abschnitten von Wurtzit- und Zinkblende-Kristallgittern. Diese strukturelle Anordnung hat eine ebenfalls alternierende elektronische Struktur in Form einer Typ II Bandstruktur in Richtung der Längsachse des Nanodrahtes zur Folge. Die lokalen elektronischen Eigenschaften der Nanodrähte werden mit Rastertunnelspektroskopie untersucht. Lumineszenz-Spektren, welche an einzel-

nen Nanodrähten durch den Tunnelstrom induziert werden, werden durch die Injektion von Löchern und Elektronen und deren darauffolgender Rekombination ermöglicht. Im Gegensatz zu bereits veröffentlichten Studien an ähnlichen Systemen ist die Kopplung von spitzeninduzierten Plasmonen an den Strahlungsprozess nicht notwendig. Die Form und die energetische Lage der Lumineszenzspektren wird des Weiteren mit Photolumineszenzspektren und Raman-Messungen verglichen. Es zeigt sich auerdem, dass die Energie der Photonen mit größer werdendem Drahtdurchmesser abnimmt, was auf Quantenconfinement der Ladungsträger im Draht hinweist. Mit Hilfe der Extrapolation der Abhängigkeit der Emissionsenergie vom Durchmesser, kann auf die Bandlücke geschlossen werden, welche sich im Falle eines dreidimensionalen System einstellen wird. Diese zeigt, dass die Photonen von den Zinkblende-Bereichen emittiert werden. Zudem kann man von dieser Durchmesserabhängigkeit ableiten, dass die Lichtemission von Ladungsträgern stammt, die auf Quantenpunktartige Abschnitte in den Drähten eingeschränkt sind. Die fehlende Lichtemission von den Wurtzit-Abschnitten spiegelt sich zudem im Auftreten nicht-strahlender Bereiche des Drahtes wider, was durch räumlich aufgelöste Messungen der Lichtintensität gezeigt werden kann. Mögliche Mechanismen der Lichtanregung werden diskutiert.
Die Untersuchung einzelner Moleküle des lumineszierenden organischen Materials Tris-(2-Phenylpyridin)Iridium(III) ($Ir(ppy)_3$) ist das Thema des letzten Teils dieser Doktorarbeit. Dazu werden $Ir(ppy)_3$-Moleküle auf Metallsubstrate und auf verschiedene dünne Isolatorschichten aufgedampft. Neben deren strukturellen und elektronischen Charakterisierung, werden die optischen Eigenschaften durch Verwendung tunnelstrominduzierter-Lumineszenz untersucht. Weder auf den Metallsubstraten noch auf den dünnen Isolatorschichten kann intrinsische Lichtemission, die von den Molekülen stammt, beobachtet werden. Dies deutet daraufhin, dass in diesen Systemen, die Moleküle noch nicht ausreichend von dem darunterliegenden Substrat entkoppelt sind. Vorläufige Ergebnisse zur tunnelstrominduzierten-Lumineszenz an $Ir(ppy)_3$-Molekülen auf Multilagen von C_{60} zeigen sich vielversprechend hinsichtlich der Anregung von Lichtemission von einzelnen Molekülen.

Schlagworte: Rastersondenmikroskopie, Tunnelstrom-induzierte Lumineszenz, InAs/GaAs(001) Quantenpunkte, III-V Halbleiter, Selbstorganisiertes Wachstum, CdSe Nanodrähte, II-VI Halbleiter, $Ir(ppy)_3$, Iridiumverbindungen, Organische Halbleiter

Contents

1 Introduction **7**

2 Experimental Techniques **11**
2.1 Atomic Force Microscopy 11
2.2 Scanning Tunneling Microscopy 13
2.2.1 Topography 14
2.2.2 Spectroscopy 16
2.2.3 Luminescence 17
2.2.4 Experimental Setup 19
2.3 Photoluminescence Spectroscopy 21
2.4 Raman Spectroscopy 21

3 Growth, Spectroscopy and Etching of InAs/GaAs(001) Quantum Dots **23**
3.1 Sample Preparation: Molecular Beam Epitaxy 24
3.2 General Concepts in Epitaxial Growth of InAs/GaAs Islands 27
3.2.1 Growth of Thin Films 28
3.2.2 Three Dimensional Island Formation and Morphological Transition 29
3.3 Morphologic and Spectroscopic Characterization of QDs by STM 34
3.4 Reversing the Shape Transition by Etching-Induced Lateral In Segregation 37
3.4.1 Backward Transformation of InAs Islands 38
3.4.2 Indirect Material Removal by Lateral In Diffusion . . . 41

4 Morphology and Spectroscopy of Individual Semiconducting CdSe Nanowires **45**
4.1 Growth and Sample Preparation 46
4.2 Morphologic Characterization 47
4.3 Mapping the Local Electronic Properties 49

4.4 Tunneling Current Induced Luminescence from Individual CdSe NWs 52

5 Topographic and Spectroscopic Studies of Iridium (III) Complexes on Metals and Thin Insulating Layers 61
5.1 Sample Fabrication 63
5.2 $Ir(ppy)_3$ on Au(111) Substrates 65
5.2.1 Structural Arrangement 66
5.2.2 Electronic Properties 69
5.2.3 Optical Properties 70
5.3 $Ir(ppy)_3$ on Thin Insulating Layers 71
5.3.1 $Ir(ppy)_3$ on KCl/Au(111) 71
5.3.2 $Ir(ppy)_3$ on h-BN-nanomesh/Rh(111) 72
5.4 Outlook: $Ir(ppy)_3$ on Multilayers of C_{60} 77

6 Summary and Outlook 79

Chapter 1

Introduction

Nanoscale structures are one of the most important topics in modern technology as well as in current areas of research. The miniaturization of the functional part of an object can lead to dramatic changes of its properties. For example, as soon as the size of the object becomes comparable with the Fermi wavelength of its charge carriers, the electronic and optical properties are determined by quantum mechanical effects. This can be seen best in the density of states: By decreasing the dimensionality of the system from three dimensions (3D) (bulk) to zero dimensions (0D) (quantum dot (QD)) the density of states changes from continuous to discrete [1]. This effect is of particular relevance for semiconductors, because their Fermi wavelength is in the range of 10 to 50 nm, and structures of this lengthscale are much easier accessible than, for example, in metals (Fermi wavelength $\sim$ 0.1 to 1 nm), where only the properties of very small structures ($<$1 nm) are determined by the mentioned quantum mechanical effects. A further aspect special to nanoscale systems stems from the increased surface-to-volume ratio, which allows the surface, the shape as well as the number of defects of nanoscale systems to strongly influence their electronic and optical properties.
The ongoing advancements in nanoscience and nanotechnology have enabled the investigation of a great variety of fascinating basic physical phenomena, e. g. quantum mechanical effects like the quantum Hall effect [2] or the Coulomb blockade in QDs [3]. At the same time, great effort is dedicated towards the development of novel potential applications that benefit from phenomena relevant at the nanoscale, for example in the fields of optoelectronics (e. g. single nanowire (NW) lasers [4, 5]), quantum computation (e. g. based on electrostatically defined QDs controlled by gate voltages [6, 7]) or biomedicine (e. g. 1D nanostructures for the detection of biomolecules [8]). In order to realize such devices on the nanometer level it is important to control the properties of nanostructures and thus, also their synthesis methods

to a large degree of perfection.
Nanoscale structures can consist of inorganic or organic materials. The fabrication and detailed investigation of inorganic semiconductor nanostructures were already performed in the second half of the twentieth century [9]. In particular, great efforts were dedicated towards the miniaturization of the functional elements of semiconductor devices. To this end the so-called top-down approach has been typically used. Here, nano-objects are built by reducing the size of larger systems, e. g. by lithographic or etching techniques [10]. These methods are well-established in semiconductor industrial processes. The disadvantage of this method is the inability to control the shape of the structure with atomic scale precision that leads to the unavoidable presence of a large density of defects. For this reason many research groups are focusing on finding new ways to build nanostructures by using so called bottom-up techniques. Here, the low-dimensional structures form atom by atom due to intrinsic physical or chemical processes. Such mechanisms can lead to highly ordered structures [11]. One bottom-up method that is based on self-organized growth is lattice mismatched heteroepitaxy, which allows the formation of strain-induced nanoscale islands (consisting of only several thousands of atoms) with high crystalline quality [12]. Another bottom-up method commonly used to grow inorganic nanostructures exploits the technique of colloidal chemistry, where for example a catalyst particle induces the unidirectional crystallization of precursor molecules and leads to the formation of NWs [13].
Recently, organic building blocks have proven to be an attractive alternative for the fabrication of electronic compounds. The synthesis of such organic building blocks is usually performed by wet chemistry. Since the highly sophisticated methods of organic chemistry allow to precisely arrange matter on the atomic scale, a great variety of tailor made organic structures can be formed [10]. On the one hand, the use of individual molecules is promising for future applications e. g. in the field of molecular electronics where the functional parts (wires, switches, storage elements) of the electronic devices consist of single molecules [14]. On the other hand, bulk organic systems made from individual molecules are attractive for applications in devices such as organic light emitting diodes or organic field effect transistors [15, 16]. In addition to the availability of an enormous number of custom made compounds, one unique advantage of organic structures compared to their inorganic counterparts is the possibility to build absolutely identical building blocks without a varying composition and number of atoms as is usually the case e. g. for heteroepitaxially grown QDs.
The broad range of fabrication methods leads to an enormous variety of different nanoscale structures. Because of the intimate relation between the

structure and the electronic and optical properties of nanoscale systems, a detailed understanding of the nanostructures as well as their growth processes is required. In the last decades great advancements have been made with respect to the sensitivity and the development of new methodologies of various non-local characterization techniques (e. g. ellipsometry [17], X-ray photoelectron spectroscopy (XPS) [18] or grazing-incidence small-angle X-ray scattering (GISAXS) [19]). However, the signal detected by all these techniques averages over a large ensemble of individual structures. Therefore, these non-local techniques do not allow to directly correlate the measured physical quantities to an individual object or to a local structure of the object. Moreover, some effects are only observable in single objects (e. g. single photon emission in molecules [20], fluorescence blinking in colloidal nanocrystals [21]) and thus can not be detected by methods which average over ensembles of structures. In order to locally analyze individual nanoscale structures, scanning probe methods can be employed which record a physical quantity as a function of the position on a surface at the atomic scale [22].
In this thesis individual inorganic and organic semiconductor nanostructures, which are produced by different growth methods, are investigated by means of scanning probe techniques. Common to all investigated systems is their ability to luminesce. The first system which is presented in this thesis are heteroepitaxially grown InAs/GaAs(001) QDs. QDs represent one of the most basic nanostructures. Because of their discrete electronic states they are often called 'artificial atoms' [11]. Besides the investigation of their structural and electronic properties also their growth process via lattice mismatched heteroepitaxy is studied. The second presented system are CdSe NWs which are grown by wet chemical methods. These 1D structures have gained much interest in the last years, because of their unique properties that stem from their anisotropic geometry (e. g. polarization anisotropy [23]). The last system under investigation are organic iridium complexes, i. e. tris-(2-phenylpyridine)iridium(III) ($Ir(ppy)_3$). $Ir(ppy)_3$, when embedded in thin layers of a host material, shows great potential for highly efficient organic light emitting diodes [24]. The ability to excite luminescence of single $Ir(ppy)_3$ molecules is promising for the realization of for example single photon emitters which could find applications for example in quantum cryptography.
The thesis is organized as followed: In chapter 2 the used experimental techniques are described. Chapter 3 deals with spectroscopic investigations of InAs/GaAs(001) QDs and the shape evolution of the QDs during controlled material removal. The local electronic as well as local optical properties of CdSe NWs are discussed in chapter 4. In chapter 5, single $Ir(ppy)_3$ molecules which are deposited onto metal surfaces as well as onto ultrathin insulating layers are investigated. Finally, a detailed summary is presented together

with possible future experiments.

Chapter 2

Experimental Techniques

The investigation of the morphological structure and the optical and electronic properties of individual objects at the nanoscale requires very sensitive characterization techniques. Suitable methods that allow for the electronic and morphological characterization of surfaces with atomic precision are scanning probe techniques. In this thesis the two commonly used scanning probe techniques are utilized: Atomic force microscopy (AFM) is used for the structural characterization of larger sample areas in order to obtain statistical information on e. g. height distribution and size distribution of nanoscale objects. Furthermore, scanning tunneling microscopy (STM) measurements provide detailed insight into the structure on the atomic scale. Besides the structural investigation, scanning tunneling spectroscopy (STS) and tunneling current induced luminescence are used to locally probe the electronic and optical characteristics of different systems. In addition to these scanning probe techniques standard methods for the optical characterization like photoluminescence (PL) spectroscopy and Raman spectroscopy are utilized. The use of several different techniques allows to get complementary information and leads to a comprehensive understanding of the investigated systems. In this chapter, the different scanning probe techniques employed are described in detail, followed by an overview of the used optical methods.

2.1 Atomic Force Microscopy

A powerful method for the structural characterization on the nano- and micrometer scale is AFM [25]. This technique makes use of the forces between

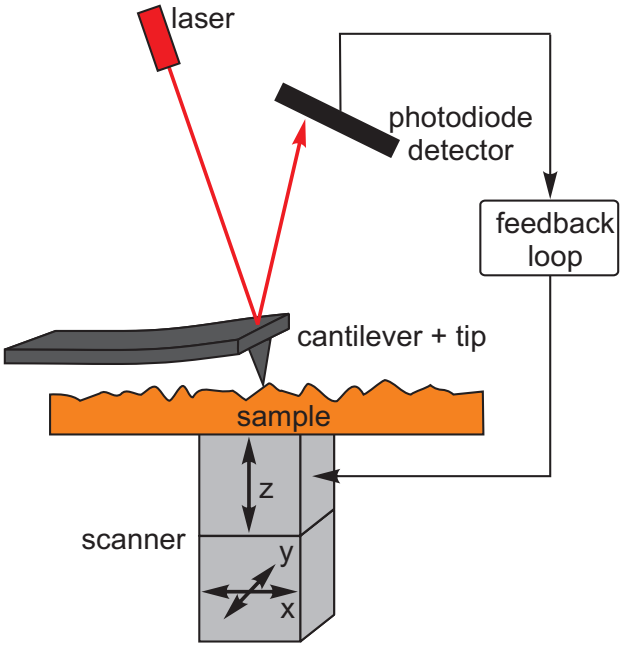

Figure 2.1: Schematic representation of AFM.

a sharp tip and a sample surface and enables the possibility to obtain a topographic image of the surface structure. The interaction between tip and sample is determined by a variety of different forces, i. e. electrostatic, magnetic, Van der Waals, chemical and meniscus forces. AFM can be applied to conducting and to nonconducting samples, like insulators, biological samples or polymers [26]. The tip with a radius of only several nanometer is mounted at the end of a cantilever. The interaction between the tip and the surface leads to an attraction or repulsion of the tip depending on the distance between the tip and the sample which results in a bending of the cantilever (Figure 2.1). This bending is detected with a laser beam which is directed on the cantilever and reflected to a photodiode. The feedback loop keeps the cantilever deflection constant by adjusting the vertical position of the sample by means of a piezo motor. By scanning across the sample surface and monitoring the z-piezo movement a topographic image of the surface is obtained. Another possibility to obtain the surface structure is to record the laser deflection without the adjustment of the vertical position, which is suitable for very flat surfaces. In general, it can be distinguished between static and dynamic operation modes:

- In the static mode the deflection of the cantilever is kept constant by adjusting the distance between tip and sample. The resulting image shows a contour of constant force. Usually, in this mode, the tip is in close contact to the sample and strong repulsive forces between tip and sample atoms are used as the feedback signal. This is why this mode is often called **contact mode**. The main drawback of this mode is that softer samples (e. g. biological samples) can be easily damaged by the tip.

- In contrast to the static mode, the tip is forced to oscillate close to its resonance frequency in the dynamic operation modes. If the cantilever comes closer to the surface the oscillation amplitude, frequency and phase are modified depending on the forces between tip and sample. Two major dynamic modes exist: frequency modulation AFM and amplitude modulation AFM. In the frequency modulated mode the amplitude of the oscillation is fixed, while the frequency shift is measured. In contrast, the frequency is kept constant and changes in the amplitude are measured in the amplitude modulated mode. A frequently used amplitude modulated mode under ambient conditions is the so called **tapping mode**, where the tip is forced to oscillate with a high amplitude ($\sim$100 nm) at a fixed frequency. In every oscillation the tip slightly interacts with the surface, but the high amplitude prevents the tip to stick on the surface and the intermittent contact avoids tip or sample damage [27].

Because of the above mentioned advantages of the tapping mode, this is the mode of operation of the *Digital Instruments Nanoscope IIIa Multimode* AFM used in this work.

2.2 Scanning Tunneling Microscopy

STM ist the ultimate technique to characterize the structure and the electronic properties of conducting surfaces on the atomic scale in real space. Even though it was originally used for obtaining topographic information, a variety of further techniques have evolved from its initial use, e.g. STS, local luminescence excitation or spin polarized STM [22, 28]. In this section the basic principle of STM with respect to obtaining topographic and electronic

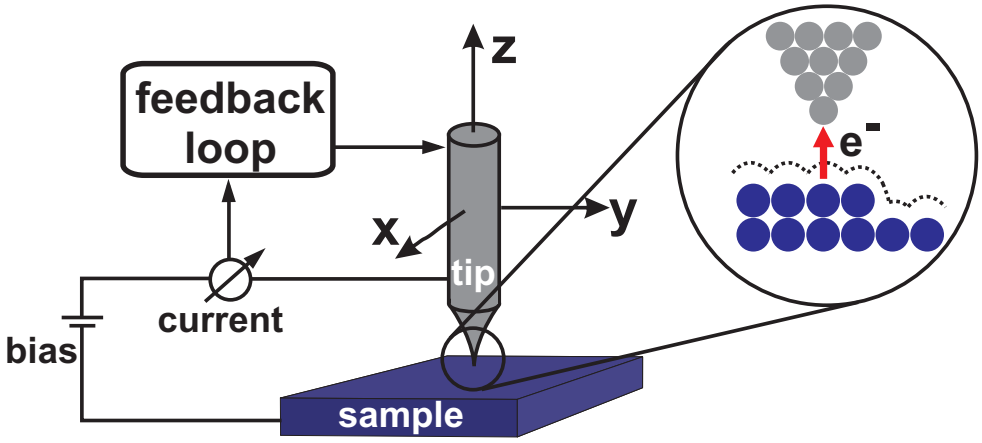

Figure 2.2: Schematic illustration of a scanning tunneling microscope.

information as well as local photon excitation by means of the tunneling current will be discussed. Finally, the experimental setups of the STMs used in this work are described.

2.2.1 Topography

STM is based on the quantum mechanical tunneling effect. The basic operation principles are sketched in Figure 2.2. A metallic tip is positioned extremely close (several Å) above a conductive or semiconductive sample, which is mounted on a piezoelectric scanner. Because of the small tip to sample distance, the wavefunctions of the sample and the tip overlap. By applying a bias between sample and tip, electrons can tunnel through the vacuum barrier. In order to calculate the tunneling current it is necessary to know the wave functions of the tip and the sample. However, details of the electronic structure of the tip are usually not known. In a simple approximation one can model the tip as a spherical potential well, whose electronic structure can be described by a s-wave approximation. Tersoff and Hamann [29,30] used this simplification to describe the relation between the tunneling current $I(V)$ and the local density of states (LDOS) of the tip ρ_t and the sample ρ_s leading to the following expression:

$$I(V) \propto \int_{-\infty}^{\infty} \rho_s(E)\rho_t(E-eV)\tau(E,V,z)(f(E-eV,T)-f(E,T))dE. \quad (2.1)$$

$f(E-eV,T)$ and $f(E,T)$ are the Fermi distributions of tip and sample at a temperature T and an energy E which lead to a broadening of the states. V is the applied bias between tip and sample and $\tau(E,V,z)$ is the transmission coefficient of the tunneling gap and is given by [31]:

$$\tau(E,V,z) = \exp(-2z\sqrt{\frac{m_e}{\hbar^2}(\Phi_s + \Phi_t - 2E + eV)}) \tag{2.2}$$

where z is the width of the tunneling gap (i e. the distance between tip and sample), m_e is the electron mass and Φ_s and Φ_t are the workfunctions of the sample and the tip, respectively. At low temperatures the Fermi distribution can be simplified to a step function which yields for 2.1:

$$I(V) \propto \int_0^{eV} \rho_s(E)\rho_t(E-eV)\tau(E,V,z)dE. \tag{2.3}$$

If $V \ll \Phi_s, \Phi_t$ the transmission coefficient can be further simplified by:

$$\tau(z) = \exp(-2z\sqrt{\frac{m_e}{\hbar^2}(\Phi_s + \Phi_t)}) \tag{2.4}$$

Thus, expression 2.3 can be rewritten by

$$I(V) \propto \tau(z) \int_0^{eV} \rho_s(E)\rho_t(E-eV)dE. \tag{2.5}$$

The first factor shows that the tunneling current depends exponentially on the tip-sample distance and the second factor shows the dependence on the LDOS of tip and sample. It should be mentioned that approximation 2.4 is not valid for high voltages (>1 V). However, high voltages are often required to perform STM measurements on semiconductors. As a consequence, the transmission coefficient can not be separated from the integral, as it was done to obtain equation 2.5, which leads to a weighting of the LDOS by $\tau(E,V,z)$. As illustrated in Figure 2.2, the x-y-piezo scanner is used to scan over the sample surface to measure the tunneling current as function of the lateral position of the tip. In the constant current mode the electronic feedback control keeps the tunneling current constant by readjusting the height of the tip by means of the z-piezo scanner. In contrast, in the constant height mode, the height is kept constant and the current is recorded in dependence on the sample position. All the STM measurements shown in this work are performed in constant current mode.

2.2.2 Spectroscopy

In STS the current $I(V)$ or the differential conductance $dI(V)/dV$ is recorded as a function of the voltage at a fixed position on the surface and under open feedback loop. Thus, the distance between tip and sample remains constant and the initial position is defined by a setpoint current $I_{setpoint}$ and voltage $V_{setpoint}$. Using the simplified expression of Equation 2.5 (Tersoff-Hamann model) and assuming that ρ_t and $\tau(z)$ are independent of V, the differential conductance can be expressed by

$$\frac{dI}{dV} \propto \rho_s(eV)\rho_t(0). \tag{2.6}$$

Given that the LDOS of the tip does not have any strong features and only small voltages are used, the dI/dV signal is proportional to the LDOS of the sample. The shape of the spectra strongly depends on the selected distance between tip and sample (i.e. on $I_{setpoint}$ and $V_{setpoint}$), which is caused by the distance dependency of the transmission coefficient. For semiconductors it is not possible to map the LDOS across a wide energy range with one $V_{setpoint}$ and $I_{setpoint}$ since the DOS in a semiconductor strongly varies between the bandgap (no DOS, no tunneling current) and in the band (high DOS, high current) [28]. Two extreme cases can be distinguished: First, setpoint voltages close to the bandedge allow to identify the beginning of the bandgap but complicate the analysis at large voltages since the increase of the voltage leads to tunneling into the band and an exponentially increasing current that can lead to tip or sample damage. In contrast, higher setpoint voltages enable to record the conductivity deeper in the band, but complicate the measurement of small conductivities close to the beginning of the bandgap since the current is too small. Hence, a large dynamic range can be only achieved by using several different tip-sample separations. In order to eliminate the effects of distance dependency, one can normalize the spectra by dividing the differential conductance dI/dV by the total conductance I/V. However, for semiconductors with larger bandgaps (>0.5 eV) the expression $\frac{dI/dV}{I/V}$ diverges in the bandgap, caused by the fact that the current close to the bandedge decreases much faster than the differential conductance. This can be circumvented by adding a small offset to the denominator I/V.
Typically, the dI/dV signal is measured directly via a lock-in amplifier. An AC signal with a typical amplitude of several tens of mV is used to modulate the ramped bias voltage. The differential conductance is then recorded directly, which enables an improved signal to noise ratio.

2.2.3 Luminescence

STM is not only the ultimate tool to locally obtain atomic scale information in both topographic and spectroscopic measurements at surfaces, but can also be employed to stimulate local photon emission. In this technique the tip is used to inject low energy electrons in order to locally excite photon emission. Thus, also information about the optical properties on the atomic scale can be obtained. The first experiments regarding scanning tunneling current induced luminescence (STL) go back to Gimzewski et al., who describe observations of light emission from a tunneling junction by using Si(111)7×7 and polycristalline Tantalum [32]. During the last decades tunneling current induced photon emission was performed in a broad variety of systems, like metal substrates [33], metal nanoclusters [34, 35], semiconductors [36, 37], semiconductor nanostructures [38–40] and molecules [41–45]. The excitation of photon emission in the STM is a pure inelastic process and can be generated in different ways. Depending on the system under investigation and the used tunneling parameters, different mechanisms play the key role in the light excitation process.
In the following, the different origins of light excitations by a tunneling current will be briefly discussed (see Figure 2.3). Firstly, inelastic tunneling from a metallic tip into a metallic substrate can lead to the radiative decay of a tip induced surface plasmon (TIP) (Figure 2.3 (a)). TIPs are localized charge oscillation waves in the tip and the sample. This is caused by the close proximity of the tip to the surface which generates a strong electric field in the tunneling cavity by applying a bias voltage [46]. It could be shown that the photon emission intensity and energy strongly depend on the applied voltage as well as on the shape and composition of the tip apex and the substrate [33, 47]. A second possible photon excitation mechanism requires a nanoscale object (e.g. quantum dot (QD) or molecule) in the cavity of the tunneling junction, and the decoupling of the nanoobject from the metallic substrate by a thin insulator, which still allows tunneling. In this way, a double tunneling barrier is formed, which can allow for the simultaneous injection of holes and electrons from the substrate and the tip followed by their radiative recombination, as illustrated in Figure 2.3 (b). The light emission can then be related to the intrinsic properties of the object, e. g. the bandgap. The insulating layer can be realized e.g. by a thin salt layer [45, 48] or an oxide film [43] that needs to be sufficiently thin to still allow tunneling. It is noteworthy, that the first and the second mechanism can not be strictly separated: The coupling of surface plasmon modes to the nanoobject can induce or amplify the light emission from the object in the tunneling gap [49]. Another light generation process can be observed in

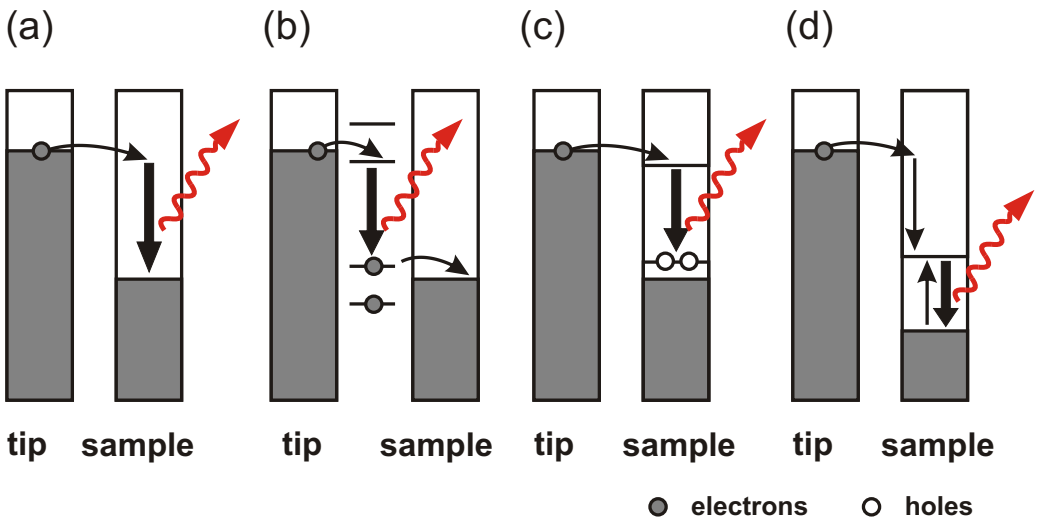

Figure 2.3: Light excitation mechanism in the STM (fat arrows indicate the radiative recombination path): (a) Surface plasmon excitation and emission by inelastic tunneling. (b) Light excitation by the simultaneous injection of electrons and holes enabled by a double tunneling barrier. (c) Injection of minority carriers followed by the recombination with the majority carriers (here holes) in the sample. (d) Injection of high energy electrons which loose their energy by exciting electron-hole-pairs.

semiconductor heterostructures where the injection of minority carriers from the tip and their subsequent recombination with the majority carriers in the sample can lead to photon emission (see Figure 2.3 (c)). This has been intensively employed to investigate the local properties of III-V semiconductor heterostructures, wherein quantum wells [37, 50, 51], quantum wires [52] or QDs [53–55] are embedded in a larger bandgap material to achieve carrier confinement. Finally, if charge carriers are injected with a sufficiently high energy into a semiconductor, impact ionization mediated emission can occur, which is illustrated in Figure 2.3(d). The injected high energetic electrons (so-called hot electrons) loose their energy by exciting electron-hole-pairs which then recombine radiatively [38, 56]. This mechanism is similar to cathodoluminescence spectroscopy, where a focused high energy electron beam scans across a surface in order to excite electrons which relax by emitting light. However, the resolution in cathodoluminescence is mainly determined by the penetration depth of the impinging electrons, which leads to a typical resolution in the μm range. In contrast, in STL spectroscopy the charge carriers are injected with a much lower energy (few eV) and, thus, a smaller pene-

tration depth. As a consequence, the resolution in STL is not limited by the penetration depth, but by the diffusion length of the charge carriers only.

2.2.4 Experimental Setup

The STM investigations were carried out in two different STM setups: While for the measurements presented in section 3.4 an home-built room temperature STM (RT-STM) was used, all other STM investigations were performed using an home-built low-temperature STM (LT-STM) working at liquid helium temperature. The LT-STM consists of two main chambers: the preparation chamber and the STM chamber, both under ultrahigh vacuum (UHV) conditions ($p < 1 \times 10^{-10}$ mbar). The preparation chamber provides the possibility of annealing the sample by electron bombardment from a filament close to the backside of the sample. Ar^+ sputtering can be used for cleaning the sample and the tip. Two evaporators with several cells are attached and allow the evaporation of different materials. A small adjacent load-lock chamber enables the transfer of samples and tips into the preparation chamber without breaking the vacuum. Furthermore, a transfer mechanism is included, which can be used for transferring samples and tips into the STM chamber. The two chambers are separated by a gate valve. The STM chamber is equipped with a liquid helium bath cryostat surrounded by a radiation shield held at liquid nitrogen temperature. The coarse approach of tip and sample is realized by a "Pan design" using a "slip-stick" piezo system. The sample can be moved several millimeters [57]. For scanning, a cylindrical piezo connected to eight electrode segments is employed: four segments for the horizontal motion and four for the vertical movement.

Over the past years a photon detection setup has been integrated in the LT-STM which was the subject of an earlier PhD thesis [58]. Three independent optical light paths are focused to the tunneling gap. This is realized by three adjustable aspheric lenses (numerical aperture of each lens 0.42) which are mounted at an azimuth angle of 90° from another (see Figure 2.4 (a) and (b)). The adjustment of the lenses with respect to the tip is realized by piezo motors which allow a movement of the lenses in all three dimensions. The light collected by the lenses is then directed out of the vacuum. This is done by guiding the light onto three flat mirrors and, subsequently, into three vertical light paths. Holes in the helium and nitrogen radiation shields let the light pass out of the cryogenic part (see Figure 2.4 (c)). Finally, the light leaves the UHV chamber via three UHV viewports, where it can be analyzed by the desired detector (web cameras for lens adjustment, spectrometer, photomultiplier tube or avalanche photodetector). For the spectral light analysis

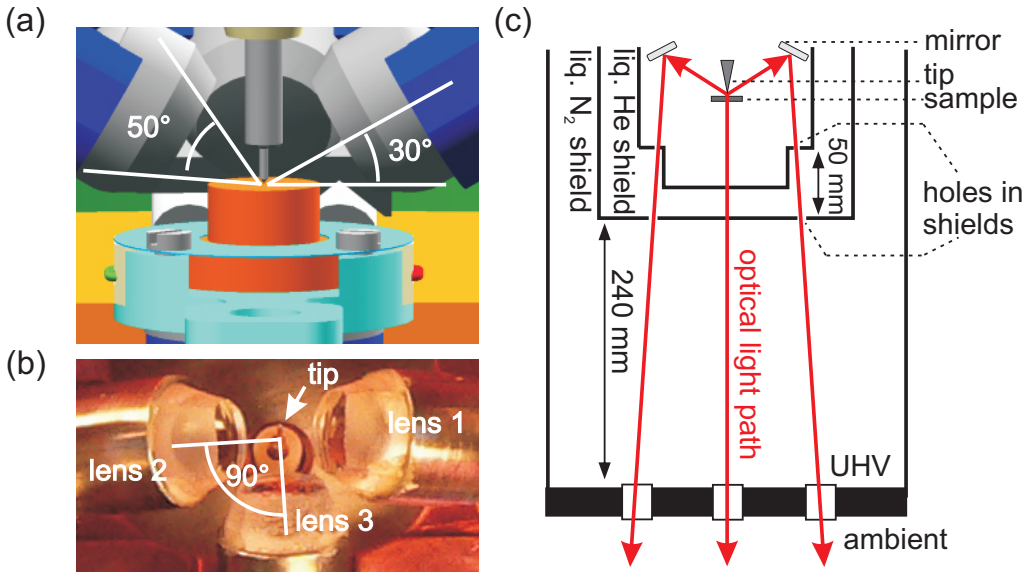

Figure 2.4: (a) Illustration of the arrangement of the tip, the sample and the three lenses. The lenses are tilted by 30° from the surface plane, the acceptance angle of each lens is 50°. (b) Bottom view photograph of the tip and the three lenses mounted at an azimuth angle of 90° from another. (c) Schematic sketch of the scanner part of the STM, the cryostat and the bottom part of the UHV chamber. The light paths are indicated by the red arrows (Figure adapted from [59]).

an *Acton Research Spectra Pro 300i Spectrograph* was used. It is equipped with a 150 lines/inch blazed grating and a Peltier-cooled CCD camera behind a light intensifier. Moreover, in order to collect the total photon yield as a function of tip position, a silicon avalanche photodetector (*SPCM-AQRH-15*, from *PerkinElmer*) can be connected to the light path. The dark count rate is 50 counts per second and enables single photon detection.

The tip is the most important part of the STM since it essentially affects the topographic as well as the spectroscopic measurements. For this study tungsten (W), platinum-iridium (PtIr) and gold (Au) tips were used. W- as well as Au-tips can be prepared by electrochemical etching [60], e.g. NaOH and HCl solution, respectively, and PtIr tips are simply cut off from a wire. Prior to the transfer into the UHV chamber the W-tips are HF etched in order to remove the native oxide layer. Several additional methods allow further tip preparation in UHV, e.g. sputtering, annealing or in-situ coating with Ag. Furthermore, the tip can be prepared on a clean metallic substrate.

2.3 Photoluminescence Spectroscopy

PL spectroscopy allows the investigation of the optical properties of semiconductors. In PL a material is excited by light exposure followed by the relaxation via transitions of different electronic states [61]. The relaxation occurs either nonradiatively or radiatively. In the latter case the emitted light can be detected and analyzed spectrally. In semiconductors, electrons are excited from the valence band into the conduction band by using an appropriate photon energy. Their subsequent recombination and thus the resulting luminescence spectrum provides insight into the bandgap, surface levels, impurity and defect states. The spatial resolution of PL is determined by the size of the diffraction limited laser spot (typically several hundreds of nm) and the carrier diffusion in the sample. In order to improve the spatial resolution, confocal PL spectroscopy is used which detects only photons originating from the focal plane of the exciting laser spot. In addition, the investigation of single nanoscale objects can be performed by a sufficient local separation of the objects (i. e. a low density ($\sim 1\,\mu\mathrm{m}^{-2}$)) to avoid ensemble averaging.
In this study a confocal laser scanning microscope was used which can be operated at liquid Helium temperature. By using an excitation wavelength of 532 nm and a microscope objective of numerical aperture 0.7 a spatial resolution of around 500 nm can be achieved.

2.4 Raman Spectroscopy

Raman spectroscopy gives information about the vibrational properties of a system by detecting and analyzing inelastically scattered photons [61]. The difference in energy of the illuminated monochromatic light and the scattered light can be related to the excitation of the optical modes of lattice vibrations in the sample. The data presented in this work were taken in the so-called backscattering geometry using a *Labram (Jobin Yvon)* single grating spectrometer, equipped with a Notch-filter. The 532 nm line was used for excitation. The resolution of our spectrometer was better than $3\,\mathrm{cm}^{-1}$. In order to avoid severe damage of the sample surface, the power of the incident laser was kept below 3 mW with a laser spot of 15 μm in diameter. The sample can be cooled to liquid Helium temperature.

Chapter 3

Growth, Spectroscopy and Etching of InAs/GaAs(001) Quantum Dots

Because of their potential applications in optoelectronics and quantum computation [62], self-assembled semiconductor quantum dots (QDs) grown by lattice mismatched heteroepitaxy have been studied extensively in the last years [12]. The electronic properties of QDs strongly depend on their size, density, shape, composition and homogeneity which in turn can be influenced by the growth parameters. In order to design QDs with specific properties, it is thus necessary to achieve a comprehensive insight into the relation between the growth process and the properties of the QDs. Besides empirically determined dependencies on the experimental parameters, this requires a detailed understanding of both, the growth and possible post-growth modification. InAs/GaAs(001) is the most frequently used QD material system as it is interesting for optoelectronic applications due to its direct bandgap in the near infrared region. Its growth mode is of the Stranski-Krastanov type, where the formation of three-dimensional (3D) islands proceeds after the completion of a two-dimensional (2D) wetting layer (WL) [12]. The shape of the 3D islands changes as their size increases. The early stage of the 3D growth exhibits small flat platelets. With increasing island size these platelets first transform into shallow pyramidal islands and subsequently into bigger islands of higher aspect ratio when a critical size is reached [63–69]. Most of the theoretical models use thermodynamic equilibrium conditions to describe the growth process of the islands [70]. However, there are controversial discussions about the validity of these theories since several studies also stress the importance of kinetic factors [71, 72]. Recently, by comparing the shape of large QDs with theoretical predictions, it could be shown that

the use of appropriate deposition parameters (e.g. low deposition rates), allows to achieve growth conditions close to thermodynamic equilibrium [73]. One possibility to further verify the validity of thermodynamic descriptions is to remove material in a controlled way after the growth of the QDs and to investigate the shape transition of the QDs as will be shown in section 3.4.

In this chapter, first, the experimental aspects of QD sample preparation by molecular beam epitaxy (MBE) are described. Second, the general concepts of thin film growth are illustrated, followed by a detailed description of the island shape transitions, where the focus lies on the InAs/GaAs(001) system. Third, scanning tunneling microscopy (STM) and scanning tunneling spectroscopy (STS) investigations of fully developed QDs are utilized to provide insights into their morphologic and electronic properties. These results can be regarded as a starting point for the following section where it is shown how one can tune the size and shape and, hence, also the optical and electronic properties of QDs by the controlled removal of material. It will be shown that several observations accompanying the material removal indicate a reversal of the shape transition that occurs during growth.

3.1 Sample Preparation: Molecular Beam Epitaxy

One possible technique to create semiconductor nanostructures on surfaces is MBE. MBE allows the growth of high purity epitaxial layers of semiconductors by the evaporation of material in front of a substrate. In order to avoid contamination and to guarantee that the atoms/molecules of the beam can reach the sample surface, the MBE growth should be carried out in ultra high vacuum (UHV) environment. This allows the production of novel materials with excellent atomic-level control of surfaces and interfaces [74]. Under certain conditions this method offers the possibility of forming strain-induced nanoscale islands (dimension $\sim$10 - 100 nm) with high crystalline quality, so-called QDs [12].
The source materials are placed in different effusion cells which can be heated independently in order to generate an appropriate flux of molecules or atoms needed for the desired growth process. By opening a shutter, this flux can pass the UHV chamber and reach the surface of a substrate placed in front of the beam. The substrate can be heated in order to provide enough surface mobility of the impinging atoms. One advantage of MBE is that each growth

step can be controlled in-situ by reflection high energy electron diffraction (RHEED) which allows to determine the flux rate, the surface quality and the surface reconstruction. This analysis method uses a high energy (∼20 keV) electron beam which strikes the sample surface at a glancing angle and is then reflected to a fluorescent screen imaging the diffraction pattern. In spite of the used high electron energy, the length of the penetration depth perpendicular to the sample surface is only a few monolayers (MLs) due to the grazing incidence of the electron beam. This leads to a very high surface sensitivity. If the surface is perfectly flat, the intensity of the spots in the diffraction pattern will be very high. With the beginning of the layer-by-layer growth the intensity of the spot decreases, due to the formation of steps, which are formed during the growth of the first ML and which scatter the incoming electrons. Further growth completes the 2D islands to one ML and increases again the spot intensity, resulting in an oscillatory behavior of the intensity. That means that the time between two maxima of this oscillation is needed to grow one ML, thus, allowing to calibrate the growth rates of the cells. In addition to that, the surface morphology can be qualitatively determined by the analysis of the shape of the diffraction spots: For typical non perfectly flat surfaces the RHEED pattern appears 'streaky'. This can be explained by the broadening of the radius of the Ewald sphere and of the reciprocal lattice rods parallel to the surface due to a slight angular and energetic variation of the electron beam and due to the non idealness of the surface (e. g. phonons and defects) [75]. As a consequence the intersection of the reciprocal lattice rods with the Ewald sphere forms streaks [76]. In contrast to the appearance of a 'streaky' pattern in the case of a flat surface, small crystalline islands on the surface lead to bulk scattering in these islands and thus to 'spotty' diffraction spots. This can be utilized to notify the formation of islands in the Stranski-Krastanov growth mode (see section 3.2). Finally, the periodicity of the diffraction pattern indicates the surface reconstruction (as detailed below). Since the geometry of the RHEED setup does not affect the growth process, it represents a powerful instrument for the in situ analysis and control of the sample.

Because of their technological importance and their role as a model system for various physical phenomena III-V compound semiconductors (e.g. GaAs, AlGaAs, InAs) are one of the most frequently used MBE materials. In the following we will restrict the description to the case of GaAs(001) substrates. Complementary to the growth of well-defined layers, III-V-MBE chambers equipped with an in situ etching gas system can be employed to remove material in a highly controlled way. The etching gas (e.g. $AsBr_3$ or $AsCl_3$) can be introduced into the chamber via a mass flow controller. In case of $AsBr_3$ the impinging molecules form $GaBr_x$ ($InBr_x$) molecules on the GaAs (InAs)

substrate and desorb [77]. The etching mechanism occurs in a layer-by-layer fashion which offers the possibility of being controlled by RHEED oscillations as well. While for low substrate temperatures ($\leq 420\,^{\circ}\mathrm{C}$ for GaAs) the etching rate is reaction-rate limited, the etching rate is supply-rate limited for GaAs substrate temperatures above $420\,^{\circ}\mathrm{C}$. In this regime the etching rate increases linearly with increasing flux rate [78]. Furthermore, etching is also material selective: the etching rate of pure InAs is approximately 1.3 times higher than the etching rate of pure GaAs [79].
The low growth rate (typically 0.1 - 1.0 ML/s) and the UHV environment make the MBE technique complex and time consuming. However, these pretended disadvantages represent also the power of this deposition method: First, MBE provides an excellent control of interfaces due to the low and highly controlled growth rate. Second, the UHV environment allows the in situ control of the surface by surface characterization methods (e.g. RHEED, Auger electron spectroscopy [75]), the growth of high-purity samples and the growth of clean and well-defined surfaces [74].
All the samples discussed in this chapter were grown by a commercial *Riber* MBE system equipped with an $AsBr_3$ etching unit. The base pressure is $1 \times 10^{-11}\,\mathrm{mbar}$. Heavily doped GaAs(001) substrates were deoxidized in-situ prior to the growth of a several hundreds of nm thick GaAs buffer layer at $610\,^{\circ}\mathrm{C}$ in order to provide a smooth surface for QD growth. The substrate temperature calibration was achieved by the transition of the (2×4) to (4×4) surface reconstruction monitored in the RHEED pattern. This change in the surface reconstruction corresponds to a substrate temperature of $500\,^{\circ}\mathrm{C}$. In Figure 3.1 (a) and (b) the structural models of the GaAs(001) (2×4) and (4×4) surface reconstructions (detailed in section 3.2) and the corresponding RHEED patterns in the $[\bar{1}10]$ azimuth are shown. After the temperature calibration the substrate temperature was lowered to $470\,^{\circ}\mathrm{C}$ and 1.8 MLs of InAs were deposited at a growth rate of 0.008 ML/s and an As_4 beam equivalent pressure of $\sim 1 \times 10^{-5}\,\mathrm{mbar}$. After a growth interruption of 30 s, either the samples were cooled down immediately with a cooling rate of $1\,^{\circ}\mathrm{C/s}$ or $AsBr_3$ was introduced at a nominal etching rate of 0.04 ML/s (for planar, unstrained InAs). For the samples, which were investigated by means of STM, the GaAs buffer layer was Si n-doped by the simultaneous evaporation of Si during the growth of the GaAs buffer in order to facilitate stable tunneling. The resulting doping concentration was $\sim 10^{18}\,\mathrm{cm}^{-3}$.
The experimental STM studies require clean and well-defined structures and therefore must be transferred from the MBE system to the STM chamber without breaking the vacuum. This can be achieved by the usage of a vacuum suitcase which can be attached to the MBE chamber as well as to the STM. The suitcase is pumped independently via ion pumps and reaches a

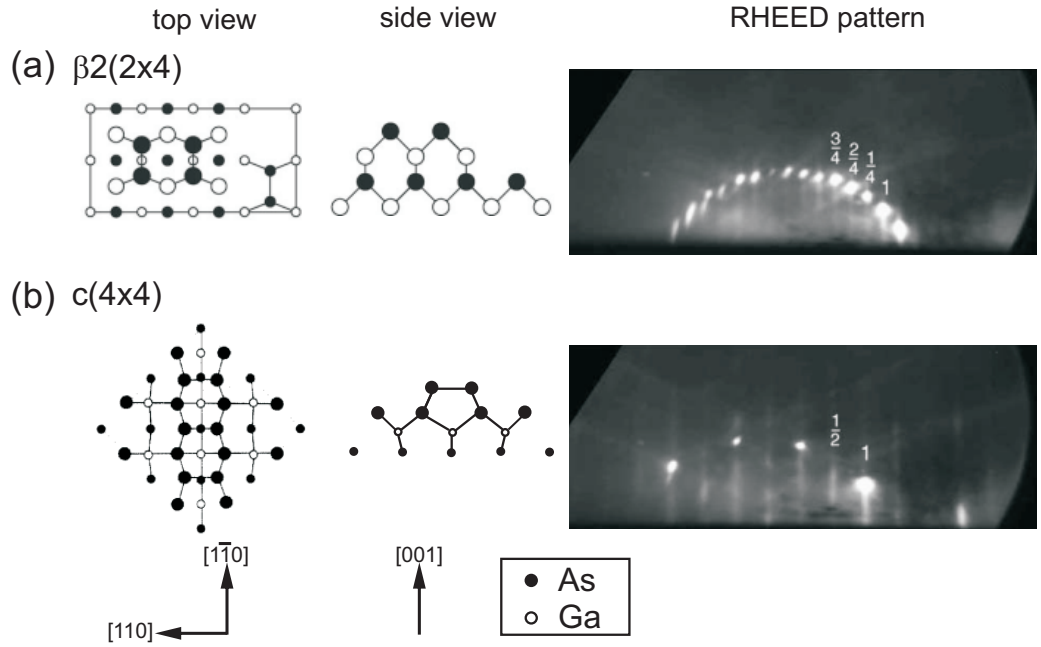

Figure 3.1: Structural models of the (a) $\beta(2\times4)$ and (b) c(4×4) GaAs (001) surface reconstructions and the corresponding RHEED patterns in the [$\bar{1}$10] azimuth, respectively. Figures adapted from [76, 80].

base pressure of 1×10^{-10} mbar.

3.2 General Concepts in Epitaxial Growth of InAs/GaAs Islands

MBE enables the epitaxial growth of crystalline material as described in the previous section. If the deposited material is different from the substrate material, this is called heteroepitaxial growth, if both materials are the same homoepitaxial growth. In the following the influence of thermodynamic as well as kinetic factors on the growth process is discussed, followed by the characterization of the three different main growth modes: layer-by-layer growth mode (or Frank-van der Merwe), island growth mode (or Volmer-Weber) and layer-plus-island growth mode (or Stranski-Krastanov). Subsequently, a

simple thermodynamically based theoretical approach to nucleation is presented and the evolution of islands in case of InAs deposition on GaAs(001) is described.

3.2.1 Growth of Thin Films

The consideration of thermodynamic as well as kinetic factors are essential for the description of thin film growth [11]. There are different important growth parameters favoring either thermodynamic or kinetic processes. One is the surface diffusivity D, which describes the ability of the deposited atoms to move around on the surface. This thermally activated process can be controlled via the substrate temperature during the growth. Another important parameter is the deposition rate F specifying the number of atoms or molecules that reach the surface per unit time. The ratio between D and F plays a key role in the growth process. If the material flux is large or the surface temperature is low (i. e. D/F small) the absorbed atoms agglomerate before they reach the surface potential minima, because the number of impinging atoms per time interval is high. Then the growth process is controlled by kinetic mechanisms [81]. In contrast, a low deposition rate and a high substrate temperature result in a system close to thermodynamic equilibrium [82]. While the deposition rate F enters the ratio controlling thermodynamic versus kinetic processes in a linear way, the substrate temperature T enters exponentially and has, thus, a much stronger impact. During the deposition of thin films different growth modes can occur depending on the change of the surface free energy $\Delta\gamma$ of a surface before and after deposition [83]. For a deposition process $\Delta\gamma$ can be described by the following equation:

$$\Delta\gamma = \gamma_F + \gamma_{S/F} - \gamma_S \tag{3.1}$$

γ_F is the surface free energy of the film-vacuum interface, γ_S is the surface free energy of the substrate-vacuum interface and $\gamma_{S/F}$ is the interface free energy between the substrate and the film. This equation characterizes the interaction between the substrate and the adsorbates. Two limiting cases can be considered: First, the interaction between the substrate and the adsorbate adatoms is higher than the interaction between the adatoms among themselves, i. e. $\Delta\gamma \leq 0$, resulting in a layer-by-layer growth mode or **Frank-van der Merwe** growth. Second, if the adatoms are more strongly bound to each other than to the substrate ($\Delta\gamma > 0$), 3D islands will form on the surface. This is called island growth or **Volmer-Weber** growth. If the sign of $\Delta\gamma$ changes from a negative to a positive value with the number of deposited film layers, a mixed growth mode takes place (**Stranski-Krastanov** growth

mode). This means that after a critical thickness the growth changes from layer-by-layer mode to the formation of islands on top of the grown layers. The most common reason for Stranski-Krastanov growth is a moderate lattice mismatch between the substrate and the deposited material. The two most studied material systems are the growth of Ge on Si(001) (lattice mismatch $\sim 4\%$) and of InAs on GaAs(001) (lattice mismatch $\sim 7\%$), leading to the well-established growth of semiconductor QDs.

3.2.2 Three Dimensional Island Formation and Morphological Transition

Capillary Model for Island Growth

In order to describe the process of 3D island nucleation, the capillary model of nucleation can be used, which only includes the thermodynamically defined surface and interface energies [70]. Equilibrium conditions can be achieved by having a minimum of the Gibbs energy G. To this end one considers the change in the Gibbs energy ΔG when a deposited particle is integrated in the film. For the formation of a 3D island ΔG can be described by the following expression in dependence on the number of deposited atoms n [75]:

$$\Delta G = -\alpha \cdot n + \beta \cdot n^{2/3} \tag{3.2}$$

α describes the bulk energy difference between the atoms in the film and the islands (elastic strain energy) and β contains the surface energy of the island and the interface between island and film (surface energy). In Figure 3.2 the Gibbs energy variation is plotted as a function of the number of atoms in the island. The fact that the two terms in Equation 3.2 have different signs results in a change of the sign of the slope of ΔG with increasing number of atoms. At a certain critical number n^* the change of ΔG becomes negative ($\partial \Delta G / \partial n < 0$). That means that any further increase of the number of atoms leads to a reduction of the Gibbs energy after a critical energy barrier ΔG^* had overcome. As a result, islands with a volume $n > n^*$ grow while in the opposite case ($n < n^*$) islands tend to decay. The existence of this theoretical predicted critical number of atoms has been also verified experimentally in several material systems (e. g. Hg and Ag on Pt, Ag on NaCl [84]). One should mention that, firstly, this classical thermodynamical approach is only valid for perfect defect free substrates and, secondly, its applicability is questionable for very small islands, since then the definition of surface and interface energies is not more applicable.
The model described above is a pure thermal-equilibrium picture of the QD growth. It should be noted that there are several studies which stress the

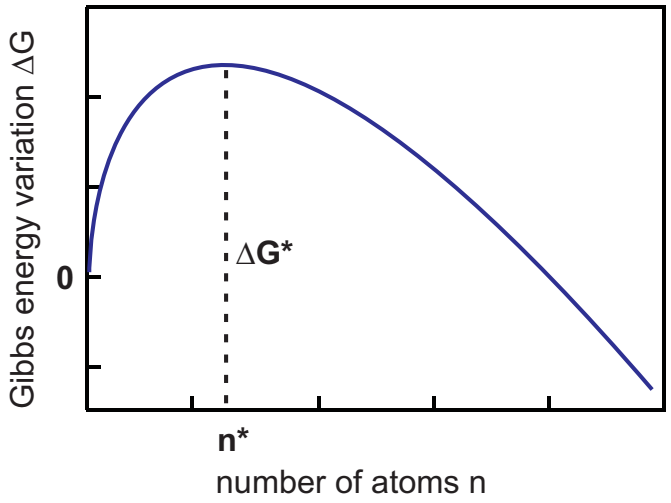

Figure 3.2: Gibbs free energy as a function of the number of atoms.

importance of kinetic factors [71, 72]. These models consider microscopic processes (e.g. diffusion of adatoms, deposition of atoms, attachment and detachment of adatoms to nuclei), that can be described by using so-called rate equations. However, the comparison of the theoretical determined equilibrium shape of the islands [85] with experimental studies [73] showed that it is possible to grow islands very close to thermodynamic equilibrium by choosing the right growth parameters.

Growth of InAs on GaAs(001)

In the following, the evolution of the GaAs(001) surface as a function of In coverage will be described briefly by reviewing the results of several studies. As already described in the previous section the growth process strongly depends on the growth parameters and significantly different results have been reported as a consequence of different growth conditions. Therefore, we will mainly focus on describing the nucleation process for growth parameters very similar to the ones we used for the studies in the following sections. The growth parameters are chosen such that the island formation is close to thermodynamic equilibrium as it could be shown in reference [73]. This has the advantage that the growth process is less sensitive on small parameter variations and, furthermore, easier to be described by theoretical models. In particular, a deposition rate of 0.008 ML/s for InAs, a substrate temperature between 470 and 500 °C and an As_4 beam equivalent pressure of $\sim 1\times10^{-5}$ mbar were chosen.

The crystal structure of GaAs is of the zincblende type, which is formed by a cubic face-centered lattice with a diatomic base and has a bandgap of 1.43 eV at room temperature [86]. Since the lattice planes in the [001] direction are alternatively formed by layers of Ga or As, the (001) surface is either Ga- or As-terminated, depending on the growth parameters (substrate temperature and As flux). All the samples in this study are grown under As-rich conditions and, therefore, As-terminated surfaces are formed. In the case of As-rich conditions, there are two relevant surface reconstructions, the (2×4) and the (4×4) reconstruction, the former developing at higher substrate temperatures ($> 500\,^{\circ}\mathrm{C}$) and the latter at lower temperatures ($< 500\,^{\circ}\mathrm{C}$) under high As flux (see Figure 3.1) [87, 88]. Since the desorption temperature of In is approximately 520 °C, the sample temperature is limited to this value. As a consequence, the samples grown for this study involve the (4×4) reconstruction of GaAs.

The deposition of InAs on GaAs(001) starts with the formation of a WL. In order to reduce the compressive stress in the WL, the deposited InAs is significantly alloyed with the atoms of the GaAs substrate, thus forming an $In_xGa_{1-x}As$ alloy. Depending on the InAs coverage and the substrate temperature a variety of different surface reconstructions can be formed [89]. For the growth conditions used in this study, the surface reconstruction of the $In_xGa_{1-x}As$ alloy is a mixture of domains with (1×3), (2×3) and (2×4) periodicity and different local stoichiometry [89,90]. Interestingly, it could be shown that on a perfect $In_{2/3}Ga_{1/3}As$ alloy In diffusion is strongly enhanced and highly anisotropic along the $[1\bar{1}0]$ direction [90].

After reaching a critical thickness of the film (between 1.65 and 1.7 MLs), the layer-by-layer growth becomes unfavorable, because of an increased strain between the substrate and the film induced by the different lattice constants. Thus, the 2D to 3D transition starts [91]. First, very small precursor islands appear (so called platelets), having a height of only 1 to 3 MLs [92]. Further deposition of InAs leads to a rapid growth of 2 to 5 nm high islands, which are characterized by well-defined {137} facets (so called huts and pyramids). Finally, at an InAs coverage of 1.8 MLs another type of island can be identified: big multifaceted islands, which we refer to as domes. Domes have an height of approximately 7 to 15 nm and consist of a variety of steep facets, among them the {137}, {101}, and {111} facets. These two well-defined types of islands coexist and could be observed in several studies for the InAs/GaAs(001) system [69, 93] (see Figure 3.3 (a) and (b)). In order to qualitatively investigate the shape transition, one can make use of the so-

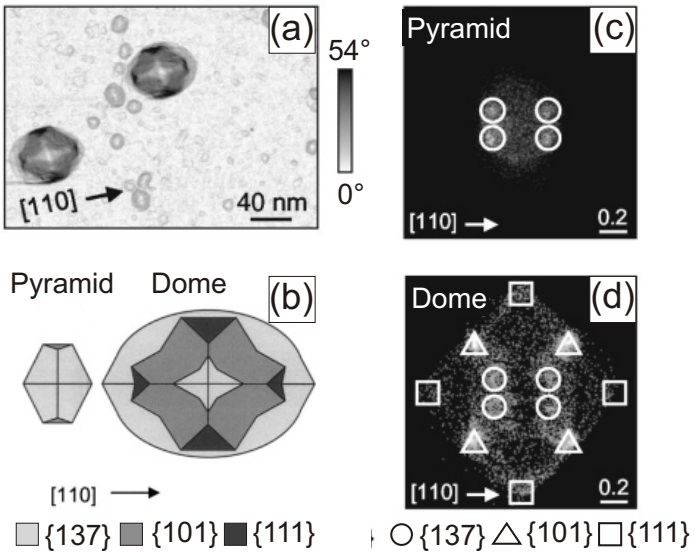

Figure 3.3: (a) STM image of 1.8 ML deposited InAs on GaAs(001) where pyramids and domes can be identified (the grayscale corresponds to the local surface slope). (b) Structural models of the two types of islands to illustrate the presence of different facets. (c) and (d) corresponding FPs. Figure taken from [69].

called facet plot (FP) which is applicable to STM and high quality atomic force microscopy (AFM) images [94, 95]. STM or AFM images are described by the height z at each lateral position (x, y) (i. e. $z = f(x, y)$). FPs represent a two dimensional histogram of the local surface gradient: All N points $(x_i, y_i)_{i=1...N}$ in the STM image which have the same value of surface slope (ξ_F, η_F) contribute to the intensity of the (ξ_F, η_F) pixel. The orientation of the facet is given by the direction of the vector connecting the center of the FP with the point of coordinates (ξ_F, η_F). The slope of a facet (tangens of inclination) is given by the length of this vector (see Figure 3.4). For example, the (001) surface of the sample having zero slope would give rise to a bright spot in the center (origin) of the FP. The FPs of pyramid and dome islands are presented in Figure 3.3 (b) - (d) [69]. The bright spots in the plots can be related to the different types of facets discussed above.
A detailed study done by Kratzer et al. [65] investigated the pyramid to dome shape transition of InAs/GaAs(001) islands both experimentally by STM measurements and theoretically by analyzing the thermodynamic stability of such a transition. It was found that for small islands flat {137} facets can effectively lower the overall energy. This leads to the flat pyramidal shaped islands described above. For islands with larger volumes, strain relaxation

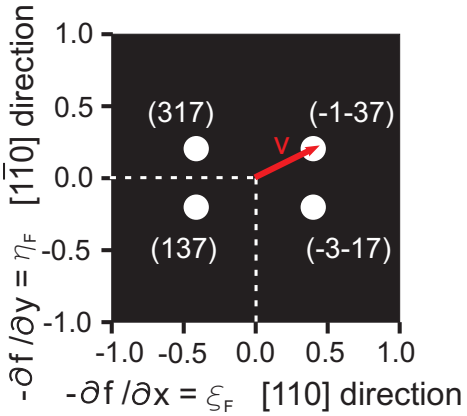

Figure 3.4: Schematic illustration of a FP. As an example, white spots corresponding to {137} facets are indicated. Orientation of the facets: $\nabla f(x,y) = (\frac{\partial f}{\partial x}, \frac{\partial f}{\partial y}) = -(\xi_F, \eta_F)$. Slope of the facets: $|v| = \sqrt{(\xi_F^2 + \eta_F^2)}$. The different Miller indices are explicitly labeled.

can occur more effectively for high structures with steep facets. The observed shape transition is shown in Figure 3.5 in the upper row: (a) shows a small pyramid with {137} facets, in (b) the island starts slowly to develop small steeper facets. In Figure 3.5 (c) the island exhibits four extended {101} facets and two small {111} facets. At last, a completely developed dome is shown in Figure 3.5 (d) which consists of extended {101} and {111} facets and small {137} facets at the island top. The shape transition is clearly illustrated in Figure 3.5 lower row by use of the FPs . The formation of the steep facets can be understood by the incomplete layer-by-layer growth of the {137} facets: the facets grow from the top of the island to the bottom stopping at a certain point. The growth of several layers of incomplete facets leads to step bunching and to the formation of steeper facets. The agreement between the experimentally observed islands and the calculated equilibrium shape of the islands gives evidence that there is a thermodynamic driving force for the formation of the dome-like islands.

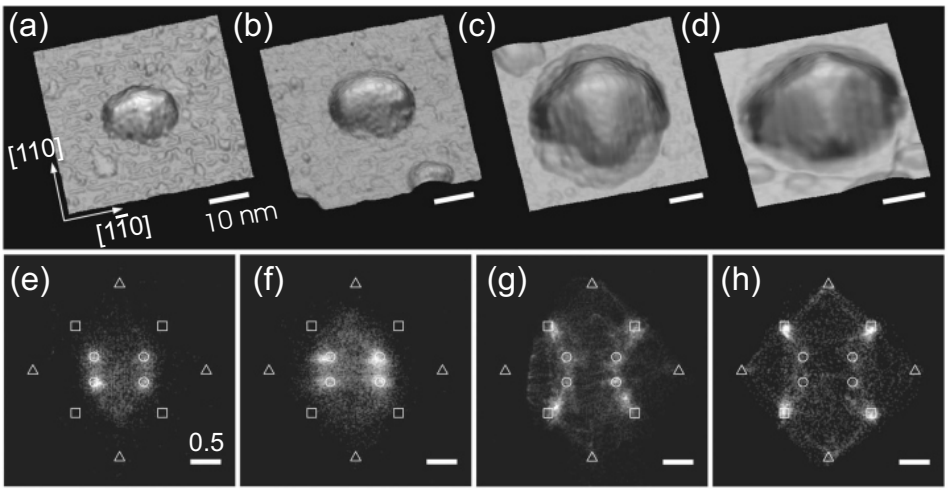

Figure 3.5: Upper row: STM images illustrating the shape transition for InAs/GaAs(001) QDs: (a) pyramid, (b) pyramid that already developed small stepper facets, (c) island after the shape transition towards extended {101} facets and (d) fully developed dome. Lower row: FPs of the shown STM images demonstrating quantitatively the shape transition. Different facets are indicated by symbols: ◯ {137}, □ {101}, and △ {111}. Figure taken from [65].

3.3 Morphologic and Spectroscopic Characterization of QDs by STM

Besides the investigation of the size and the shape of the QDs, the study of their electronic properties is of great interest. The low dimensionality of QDs leads to confinement of the charge carriers in all three dimensions and to the development of discrete electronic states [96–98]. Due to the small dimensions of the QDs (they consist only of several 10^3 atoms) the effect of single impurities, defects or structural inhomogeneities are more pronounced than for bulk crystals. Thus, the study of the electronic properties and their correlation to structural characteristics of individual QDs is highly desirable. In contrast to optical methods, STS offers the possibility to measure the discrete electronic structure directly and, additionally, spatially resolved [99–102]. In order to investigate the morphology and the electronic states in fully developed QDs, InAs QDs were grown under the conditions described in section 3.1, but with two modifications: Firstly, in order to perform STM measurements, the buffer layer needs to be strongly n-doped ($N_D = 4 \times 10^{18}\,\mathrm{cm}^{-3}$). Secondly, the states in the QDs need to

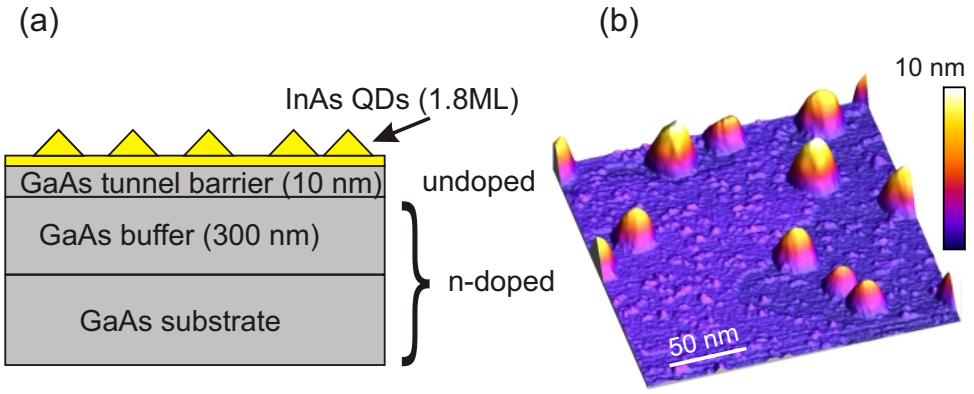

Figure 3.6: (a) Schematic sketch of the sample structure. (b) STM topography image at a coverage of 1.8 ML InAs (I_{tunnel}=0.1 nA, U_{tunnel}=-3 V).

be decoupled from the doped substrate. This was realized by a 10 nm thick undoped GaAs layer. The width of this barrier is a crucial parameter, since on the one hand, it has to be thick enough to electronically decouple the QD effectively from the substrate, but, on the other hand, it should still allow stable tunneling. A schematic illustration of the sample structure can be seen in Figure 3.6 (a). Figure 3.6 (b) shows an overview STM image of the sample taken at 4 K. Since the heights of the islands vary between 4 and 9 nm, we conclude that most of the islands are domes or not fully developed domes (transition domes).

In order to study the electronic properties of an individual QD, we now focus on one single dome. A high resolution STM image of a dome with an apparent height of 7.5 nm is shown in Figure 3.7 (a). The steep {101} and {111} factets that are characteristic of this island shape can be clearly observed (compare with Figure 3.3 (b)). Figure 3.7 (b) shows the comparison between a normalized STS spectrum on the center of the QD and on the WL. The presence of peak- and shoulder-like features in the spectrum of the QD is indicative of discrete energy states (approximately at voltages of -0.7 V, 0.6 V, 0.8 V and 1.3 V) even though the peak width is quite broad. This width suggests a short lifetime of the electrons in the QD, probably caused by a high tunneling rate through the undoped tunneling barrier. The analysis of the STS spectrum allows us to extract a lower bound of the bandgap of about 0.48 eV on the QD. Since the bulk bandgap of InAs at 4 K is lower (0.42 eV) [103], our measured bandgap is a further indication of the confinement of the charge carriers in the QD. In contrast, the spectrum assigned to the WL does not show any features in the bandgap (Figure 3.7 (b)). It

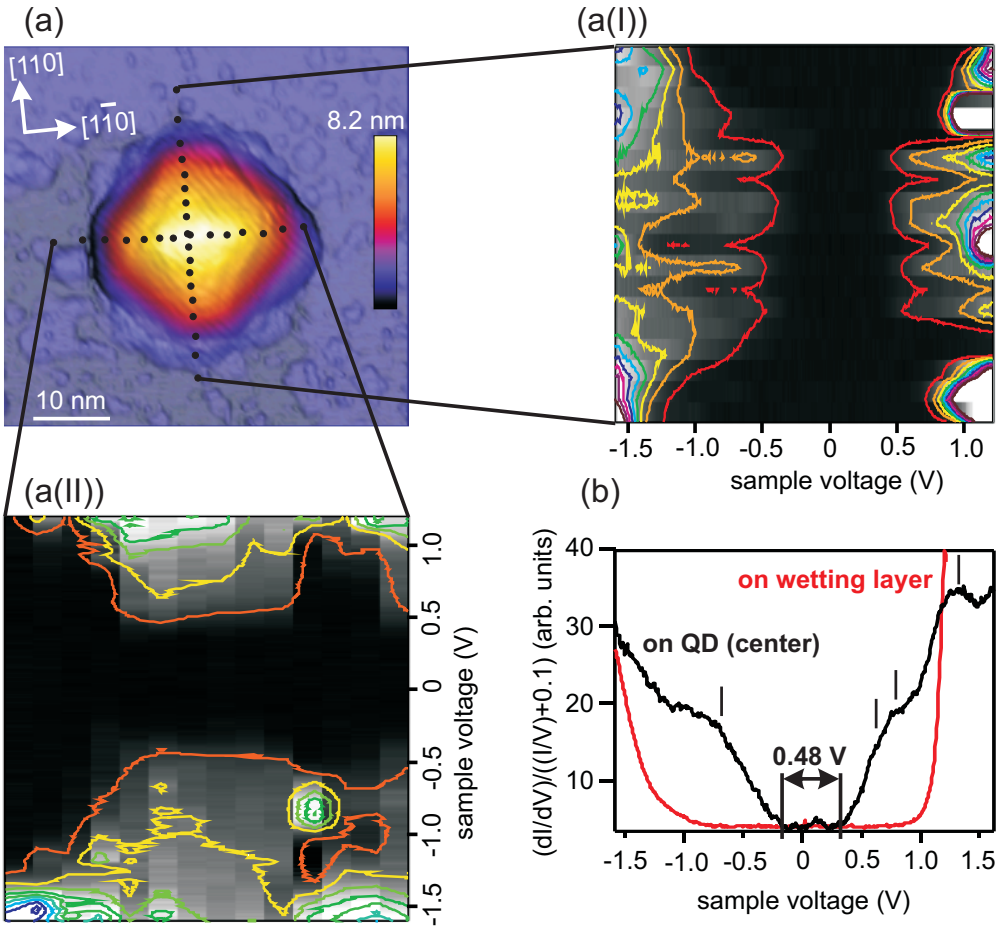

Figure 3.7: (a) STM image of a dome (I_{tunnel}=0.1 nA, U_{tunnel}=-3 V). (a(I)) and (a(II)) Differential conductance spectra (arbitrary units) along the dotted lines shown in (a) ($I_{setpoint}$=0.05 nA, $U_{setpoint}$=-1.6 V). (a(I)) shows spectra along the [110] direction and (a(II)) along the [1$\bar{1}$0] direction. The colorscale corresponds to a superposition of a grayscale (black means low conductance) and a contour plot, illustrating levels of constant differential conductance. (b) Comparison between the normalized differential conductance on the center of the QD and on the WL ($I_{setpoint}$=0.05 nA, $U_{setpoint}$=-1.6 V). The small lines roughly indicate the positions of possible confined states.

should be mentioned that the contribution of tip induced band bending might slightly affect the accuracy of the observed bandgap [104], thus leading to an overestimation. The lateral variation of the bandgap along the [110] and the [1$\bar{1}$0] directions is shown in Figure 3.7 (a(I)) and (a(II)). The spectra are recorded along the dotted lines in Figure 3.7 (a). While in the center of the

QD the bandgap is small and apparently constant, the bandgap increases to approximately 1.5 eV in the corners of the island. Two explanations can be given for this observation: First, it is known that the In concentration increases towards the center of the QD and that the border is more affected by intermixing of In and Ga atoms from the substrate in order to reduce the strain [105–107]. An decrease in the In concentration leads to an increase of the bandgap and thus could explain the observed bandgap variation. A similar behavior could be observed by Dasika et al. who performed cross-sectional STM investigations on buried InAs QDs [108]. They also observed a variation of the bandgap with an bandgap decrease toward the QD center which they ascribed to an In composition gradient. Second, even though we are not able to identify clear peaks in the spectra, the appearance of an apparently constant bandgap in the core of the QD (see Figure 3.7 (a(I)) and (a(II))) might be an indication of a circular symmetric state in the QD similar to what could be observed in other systems [99–101]. A possible reason for the absence of separated peaks in the spectra might be the thickness of the tunneling barrier as already mentioned above.

3.4 Reversing the Shape Transition by Etching-Induced Lateral In Segregation

In section 3.2.2 it was shown that the early stages of the 3D growth exhibit small flat platelets that at first transform into shallow pyramidal islands and finally into bigger islands with a higher aspect ratio when a critical size is reached. This growth transition raises the question whether a symmetric backward transition occurs if material is removed from the fully developed QDs, as has been recently observed for SiGe islands on Si(001) [109]. This would be a further evidence that the growth and also the etching are determined by thermodynamic factors. Furthermore, besides the choice of the growth parameters, material removal presents another possibility to tailor the size and shape of the islands and, thus, also the electronic properties.
A controlled removal of material can be either achieved by In desorption [110] or by $AsBr_3$ in-situ etching [79]. The former method has the disadvantage that high substrate temperatures are required. In contrast, $AsBr_3$ in-situ etching provides control on the atomic scale without the need for high temperatures. For planar structures, the etching occurs in a layer-by-

layer fashion and the rate can be controlled by the flow of supplied etching gas [79]. Thus, it represents a flexible method for the controlled removal of material. The integration of in-situ etching into the growth process has been used to fabricate a large variety of novel nanostructures, e.g. nanoholes [111], or GaAs/AlGaAs QDs [112]. For these purposes, etching rates of about 0.2 ML/s are used, which lead to etching conditions typically far away from thermodynamic equilibrium. In the present study $AsBr_3$ in-situ etching at low rates is applied to systematically change the size and shape of InAs/GaAs(001) QDs. At the etching rate used here (0.04 ML/s), which is comparable to the In deposition rate during growth, our system is closer to thermodynamic equilibrium. AFM and STM allow us to gain detailed insight into the shape evolution of the islands. Thus, this study provides information on the etching mechanism and the rearrangement of the atoms on the surface. It is found that the island size decreases much faster than expected for a direct removal of InGaAs and that the island shape changes during etching. These observations can be ascribed to In migration away from the islands as the WL is being etched as well. The main driving force for this 'lateral segregation' is the tendency of InAs to wet the GaAs substrate, because of its lower surface energy.
The starting QD nanostructures were grown with the parameters described in section 3.1. After the deposition of 1.8 ML InAs and a growth interruption of 30 s, $AsBr_3$ was introduced and etching times of 0 s, 12 s, 16 s and 20 s were used, followed by an immediate cooling of the samples to room temperature to freeze the surface morphology. Sample characterization was performed by both AFM measurements under ambient conditions and with the UHV RT-STM. The UHV suitcase was used in order to transfer the samples into the STM without breaking the vacuum.

3.4.1 Backward Transformation of InAs Islands

Figure 3.8 (a) shows representative AFM images of the as-grown and etched samples; the grayscale in these images corresponds to a combination of the local surface height and slope. As expected, with increasing etching time the dots become smaller until they lose their well-defined shape and only small 2D islands and small mounds remain on the surface. Scatter plots, where the aspect ratio of individual dots is plotted against their volume (see Figure 3.8 (b)), provide a quantitative description of the shape transformation. These plots were determined by analyzing large range AFM images ($2 \times 2\,\mu m^2$). The aspect ratio was calculated by dividing the height by the square root of the area for each of the QDs. AFM tip convolution effects might slightly overestimate the exact island volumes and underesti-

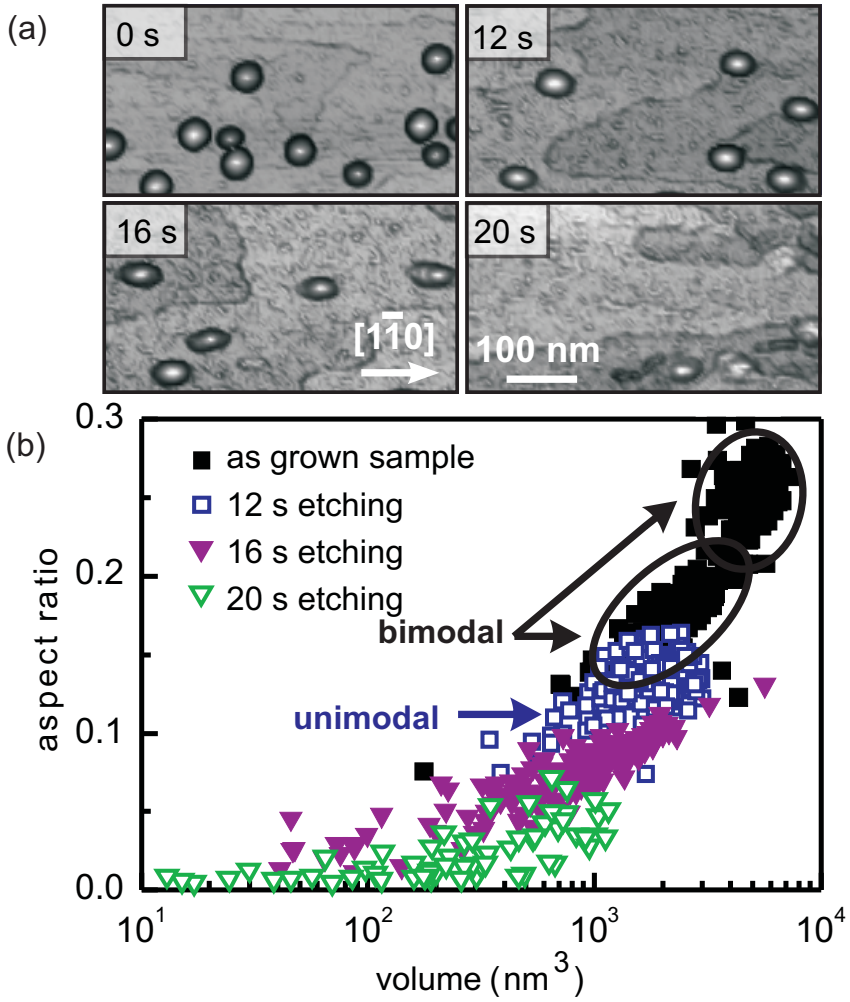

Figure 3.8: (a) AFM images of InAs/GaAs(001) islands exposed for increasing time to in-situ $AsBr_3$ etching. The grayscale corresponds to a combination of surface height and slope to enhance small scale details. (b) Scatter plot of the islands' aspect ratio (height divided by square root of the base area) versus island volume extracted from $2 \times 2\,\mu m^2$ AFM images for different etching times.

mate the aspect ratios but their relative changes should not be significantly affected. The as-grown islands are characterized by a typical bimodal size distribution [64, 93], which, however, changes to unimodal upon etching (see Figure 3.8 (b)). A similar but reverse transition (unimodal to bimodal) is observed during growth [64]. In the course of etching, the QDs shrink and change their shape from high to low aspect ratio until they finally disappear. The absence of islands with high aspect ratio on the etched samples indicates

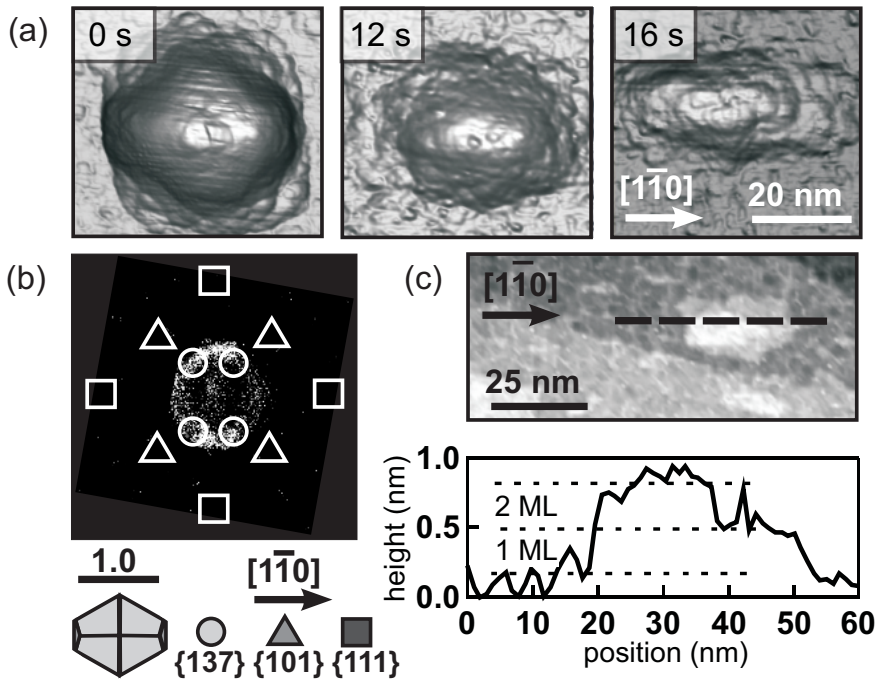

Figure 3.9: (a) STM images of InAs QDs etched for different etching times. (b) FP corresponding to an STM image of a 12 s etched sample. The main surface orientations are indicated. A structural model of a pyramid is also shown. (c) STM image of a 16 s etched sample. The graph shows the profile of a 2D island along the dashed line. The grayscale of the shown STM images corresponds to a combination of surface height and slope.

that domes disappeared completely. Both observations give a first indication that a backward shape transition with respect to the growth process takes place during etching. In addition to their size reduction, the islands become elongated in the [1$\bar{1}$0] direction (see Figure 3.8 (a)).

While the AFM images provide insight into the size distribution of a larger ensemble of islands, the analysis of single islands by means of STM offers the possibility to gain direct information on their shape. Figure 3.9 (a) shows STM images of the QDs after etching times of 0, 12, and 16 s, respectively. The as-grown sample reveals the presence of domes with the typical multifaceted shape with steep {101} and {111} facets [69]. After an etching time of 12 s the steep facets disappear and the islands seem to be much flatter. In order to obtain quantitative information on the shape of the islands we make use of the FP. Figure 3.9 (b) shows the FP of an STM image of a sample that was etched for 12 s. The intensity is enhanced at four differ-

ent positions close to those expected for {137} facets. No steeper facets are visible, making the FP in Figure 3.9 (b) very similar to the typical FP of a pyramidal island. These facets are not as well-defined as for the pyramids that develop during growth. This could be due to a strong redistribution of material that occurs during the etching process. The reason for this material rearrangement will be explained later in detail. Figure 3.9 (a) shows that further etching (etching time of ∼16 s) results in an irregular island shape and the disappearance of the {137} facets. This is not surprising since precursors of InGaAs pyramids can also be expected to be partially unfaceted, similar to the SiGe/Si(001) case [113]. All the etched samples, particularly the 16 s and 20 s ones, reveal the presence of small 2D islands only a few MLs high (see Figure 3.9 (c)). As already mentioned in 3.2.2, it has been reported that the 3D island growth starts from such small platelets [92, 114], which thus represent the early precursors of pyramids during the growth process. That means that the surface morphology after long etching is similar to what can be observed directly before the 2D to 3D transition during growth. Thus, the results in Figure 3.9 strongly indicate that a low etching rate leads to an island shape evolution that resembles the reversal of the growth process.

3.4.2 Indirect Material Removal by Lateral In Diffusion

For a more detailed understanding of how the material removal occurs, the size evolution of the dots is compared with the nominal amount of etched material. Since the volume of the dots, as determined by the AFM images, is not very accurate because of the tip convolution, the much more reliable measurement of the height of the islands is used. For this reason the evolution of the average height as a function of the nominal amount of etched InAs is measured by analyzing several AFM images for each etching time (Figure 3.10 (a)). After 20 s the average island height is less than 1 nm, which means that the islands have almost disappeared. Although one would clearly expect that the QDs' height decreases with the etching time, the measured height reduction is much larger than what would be derived if the material was etched uniformly all over the surface (dashed line in Figure 3.10 (a)). For example after etching for 20 s at a rate of 0.04 ML/s the total amount of material removed is 0.8 ML. If this was taken uniformly from the whole surface, the height of the QDs should have reduced by less than 1 ML, while the actual measured height reduction is almost 7 nm (∼20 ML). Thus, the experimental data can not be explained by a uniform, layer-by-layer removal of the material. On the other hand, the measured height reduction fits bet-

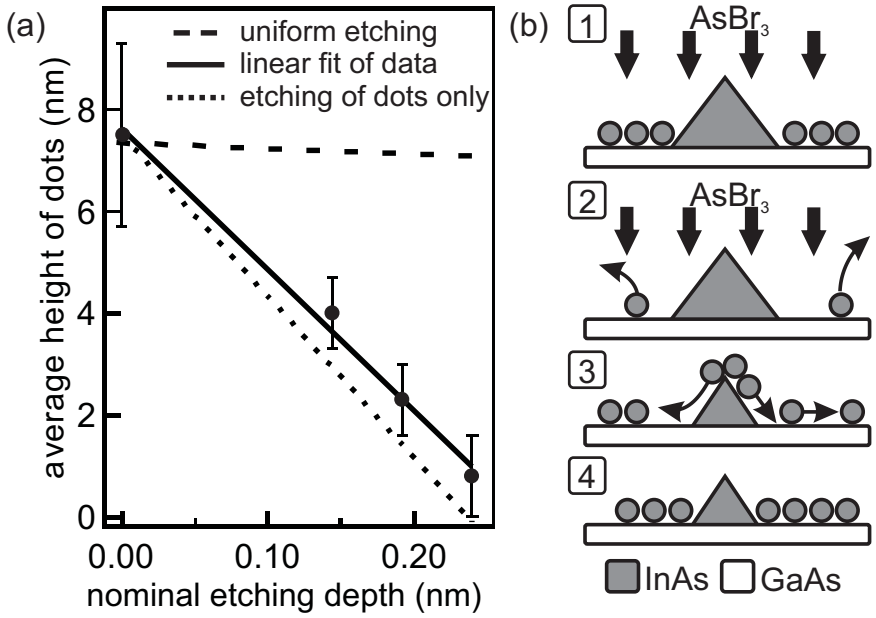

Figure 3.10: (a) Evolution of QD height as a function of the nominal etching depth. The data points represent average values obtained from the analysis of several AFM images; the error bars show the corresponding standard deviation. The straight line is a linear fit to the experimental data. The dashed and dotted lines illustrate the expected height evolutions if the etching occurred layer-by-layer or from the QDs only, respectively. (b) Schematic illustration of the etching mechanism: The etching of the WL (1, 2) drives In away from the islands to rewet the surface (3) and produces the observed island size reduction (4).

ter to a scenario where the whole amount of material is taken exclusively from the QDs, even if these occupy approximately only 10 % of the surface (QD density $\sim 75\,\mu\mathrm{m}^{-2}$). In fact, by assuming a simplified cone shaped geometry for the islands this model would result in a height reduction of ~ 8 nm after 20 s, which is quite close to what is observed (dotted line in Figure 3.10 (a)). In order to identify the origin of this drastic height decrease, the relevant mechanisms which might take place during the etching process are considered. The etching step goes along with an additional growth interruption that might result in In desorption and intermixing. Since a low substrate temperature is used and the etching times are comparatively short, the amount of desorbed In is more than an order of magnitude smaller than the material removed during etching [115, 116]. Moreover, the short etching times also prevent strong intermixing [117]. Thus desorption and intermixing can not be considered to play a key role during etching and one must

focus on the reaction of $AsBr_3$ with Ga and In surface atoms and on their subsequent desorption. Different factors have to be taken into account when evaluating the interaction between the etching gas and the substrate. Firstly, the etching is slightly material- and strain-selective (the etching rate of pure InAs is approximately 1.3 times as high as the one for GaAs [79] and strain-enhanced etching was argued in reference [111]), but this cannot properly explain the above mentioned massive size reduction of the dots. Secondly, considering that the WL is very thin compared to the dots (about 1 ML after dot formation) we would expect the WL to be removed almost completely after 20 s etching. However, STM images of the planar surface far away from the QDs are still characterized by a typical In-rich (3×n) reconstruction and also photoluminescence (PL) measurements still show the characteristic peak of the WL even after 20 s etching (data not shown). Furthermore, the PL peak ascribed to the QDs disappeared prior to the disappearance of the WL peak. Thus, it can be concluded that the progressive removal of material from the WL is accompanied by In migration from the QDs onto the bare substrate to compensate for the In depletion (see Figure 3.10 (b)). Because of the lower surface energy of InAs with respect to GaAs, this latter process lowers the free energy of the system and, as a consequence, the dots start to shrink. Since the etching occurs at a low rate, i.e. sufficiently close to thermodynamic equilibrium, the shape transition of the QDs is reversed. A similar process, i.e. wetting of the GaAs surface by InAs provided by islands, has been discussed also by Wang et al. [118] in the case of islands which are annealed after partial capping with GaAs. With this approach, which is used to adjust the height of dots after their growth [119, 120], the lack of a WL of the partially covered islands leads to their dissolution in favor of the formation of a new WL. This means that the WL cannot be removed by in-situ etching in presence of QDs, even if its thickness is much smaller than the QD height. Finally, the strong material redistribution described above might also be the reason for the observed elongation of the islands (due to anisotropic diffusion on In atoms), the increase of their base in the $[1\bar{1}0]$ direction and an enhanced alloying. In fact, once In atoms have left the QDs' top, they might redeposit together with Ga at the base of the islands [121]. It should be mentioned that these findings could also be used as an alternative explanation for similar experiments performed at higher $AsBr_3$ etching rates [111].

Chapter 4

Morphology and Spectroscopy of Individual Semiconducting CdSe Nanowires

An alternative method for the fabrication of semiconductor nanostructures relies on wet chemical processes [122]. This technique is characterized by its simple and cheap processes and allows the production of large amounts of nanostructures in solution. In contrast to heteroepitaxially grown quantum dots (QDs), here one is not restricted to certain surfaces which activate the island formation by the lattice mismatch, as described in the previous chapter. Hence, with wet chemical methods it is possible to transfer the nanostructures to different substrates or to change certain parameters after the growth (e. g. the density of nanostructures on the substrate). Furthermore, it is possible to synthesize particles of various sizes, shapes (e.g., spheres, rods, wires, and multibranches) and from a wide range of materials (e.g., CdSe, InAs, InP, and Si). This leads to an excellent tunability of their electronic and optical properties during the growth process. Therefore, they present valuable building blocks for electronic and photonic devices like lasers or light emitting diodes [123]. The successful implementation of such light emitting circuit elements requires a detailed understanding of the underlying physical mechanisms in the nanostructures, e.g., charge transport properties, as well as the involved electron hole pair creation, and photon generation processes. To this end, local probing of individual semiconductor nanostructures, with the aim of identifying the correlation between the emitted light and the structural properties, e. g. influence of impurities, defects and different crystal lattice structures, gains increasing importance.
Among the II-VI semiconductors CdSe is one of the most investigated material systems. Nanocrystals [124], nanowires (NWs) [125], and nanostructures

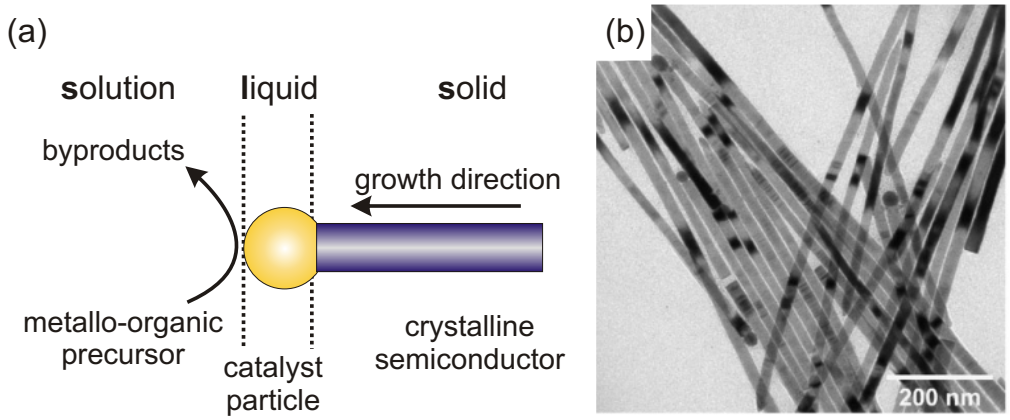

Figure 4.1: (a) SLS growth mechanism (Figure adapted from [130]). (b) Transmission electron microscopy (TEM) image of crystalline CdSe NWs (Figure taken from [131]).

with more complex shapes have been grown by precisely modifying the reaction parameters, e. g. leading to branched NWs [126] or tetrapods [127]. In this chapter the morphology as well as the electrical and optical properties of individual CdSe NWs are studied. In the first part the fabrication method of the wires is illustrated followed by a description of the deposition technique of NWs onto a substrate suitable for scanning tunneling microscopy (STM) measurements. In section 4.2 the structural properties of the NWs are shown and section 4.3 deals with their local electronic characteristics. Finally, in the section 4.4 the NWs are investigated by tunneling current induced luminescence.

4.1 Growth and Sample Preparation

One promising method for the wet chemical fabrication of nanostructures is the solution-liquid-solid (SLS) approach which is named after the three phases that are involved: the desired precursor molecules in solution, the liquid catalyst particles, and the grown crystalline structure [128]. The growth process in the SLS approach is similar to the vapor-liquid-solid (VLS) approach [129], where the growth of a solid wire is catalyzed by a supersaturated metal particle on a substrate. In SLS growth, metal catalyst particles (e.g. In, Bi, Au) in a solution serve as an adsorption and decomposition site

for precursor molecules and induce an unidirectional crystallization process, resulting in the growth of NWs (Figure 4.1) [130]. Surface ligands can be incorporated which passivate the surface of the nanostructures and render the NWs solvable in solution.
The NWs used for this study were provided by the group of A. Mews at the University of Hamburg. A highly reactive precursor (dimethyl cadmium ($CdMe_2$)) is used in order to prepare very thin NWs [131]. The synthesis is made by injecting a mixture of Bi and $CdMe_2$ into a trioctylphosphine oxide (TOPO) solution containing the Se precursor. The NWs are capped with TOPO for surface passivation.
For the experimental investigations performed in this thesis the wires were dispersed in chloroform by ultrasonication, and then deposited via spin coating onto a clean substrate under ambient conditions. The substrates consisted of a 55 nm thick gold film evaporated onto a Si substrate capped with a 300 nm thick, thermally grown SiO_2 layer. Prior to the STM measurements the samples were annealed to 420 K in ultra high vacuum (UHV) for 5 min to remove contaminants (e.g. water).

4.2 Morphologic Characterization

According to TEM and X-ray analysis, the obtained single-crystalline CdSe wires consist of alternating zincblende and wurtzite structure units. While wurtzite structure consists of a hexagonally close packed (hcp) lattice structure with a diatomic base, zincblende has a cubic face-centered lattice with a diatomic base. The relative contribution of zincblende is smaller than 10 % [132]. A TEM image of a single NW is shown in Figure 4.2 (a). The wurtzite, zincblende and transition regions (mixture of wurtzite and zincblende) are marked with 'W', 'ZB' and 'T', respectively. The difference in the crystal structure between zincblende and wurtzite is only the stacking periodicity which is 'A B A B' for wurtzite and 'A B C' for zincblende (Figure 4.2 (b)) [127]. A consequence of this lattice structure inhomogeneity is a corrugation of the electronic potential along the long axis (i. e. growth direction) of the NW. Different electron affinities as well as different bandgaps lead to an offset between the conduction bands and the valence bands between the two phases. The conduction band as well as the valence band of zincblende lie below the one of wurtzite, leading to a type II band alignment (see Figure 4.2 (c)) [133].

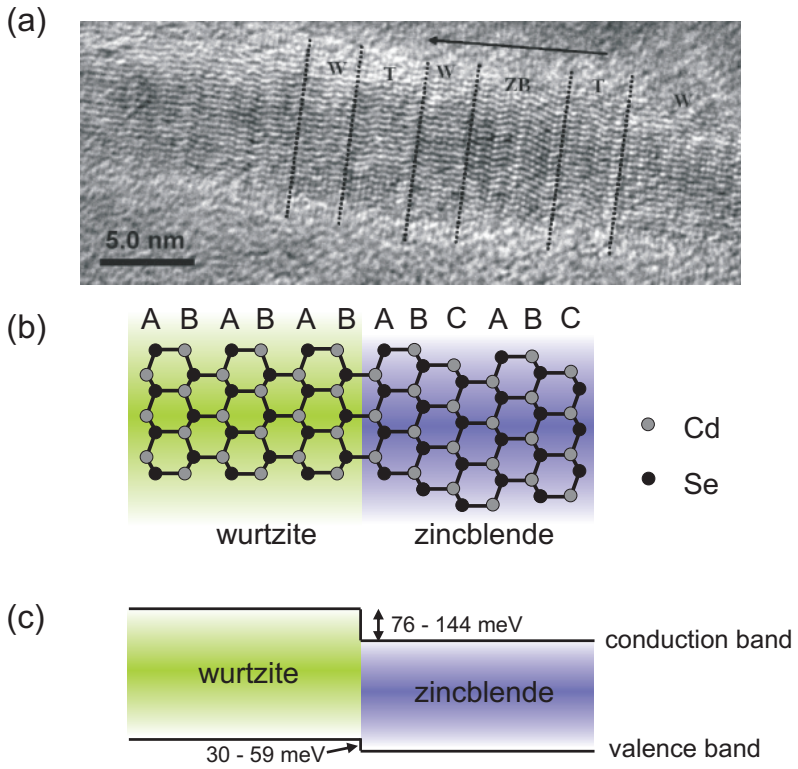

Figure 4.2: (a) High resolution TEM image of a single NW with wurtzite ('W'), zincblende ('ZB') and transition ('T') regions (Figure taken from [132]). (b) Illustration of the different stacking periodicity of wurtzite and zincblende lattice structure. (c) Schematic illustration of the type II band alignment of wurtzite and zincblende CdSe. The energy offsets of the conduction and valence bands are indicated [133].

Before transferring the samples into the STM the density of the NWs on the Au-SiO_2/Si substrate was controlled by atomic force microscopy (AFM) measurements. Figure 4.3 (a) shows an overview AFM image of a typical sample. Most of the NWs have lengths of several micrometers and heights between 7 and 22 nm. Since the scan range of the STM is $\sim 1\,\mu m^2$ the density of the NWs on the substrate should also be approximately $1\,NW/\mu m^2$ in order to guarantee effective STM measurements. This is basically achieved by varying the amount and concentration of the chloroform solution containing the NWs. Additionally, huge bundles of NWs should be avoided which is done by exposing the NW solution to ultrasound. A typical STM image of an individual CdSe NW is displayed in Figure 4.3 (b) together with the corresponding height profile shown in the inset. While the measured height

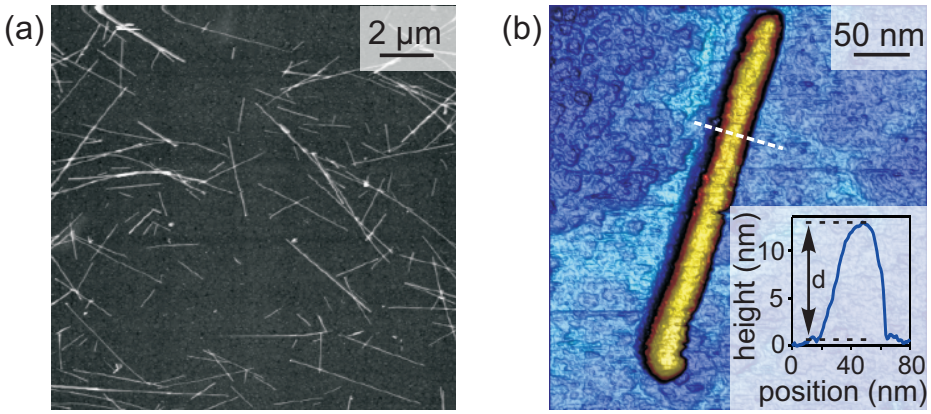

Figure 4.3: (a) Overview AFM image of a typical sample. (b) STM image of a single NW; inset shows the height profile along the dashed line.

of the wires is reliable within the limits of the surface roughness, the apparent wire width is strongly increased due to the convolution of NW and tip shape, as exemplified by the width of approximately 40 nm determined for the approximately 12 nm thick CdSe wire in Figure 4.3 (b). Atomic resolution of the NW surface could not be achieved, most likely due to residuals of the capping ligands that could not be removed during sample annealing, as well as other contaminations originating from the sample preparation under ambient conditions.

4.3 Mapping the Local Electronic Properties

Figure 4.4 shows three different types of typical scanning tunneling spectroscopy (STS) spectra which were recorded at different positions on the NW (($I_{setpoint}$=0.04 nA, $U_{setpoint}$=-2.3 V)). It has to be emphasized that the presence of the TOPO molecules and the existence of impurities inserted by the sample preparation under ambient conditions are expected to strongly complicate the analysis of the recorded spectra. Since STS measurements are highly surface sensitive, the characterization of the NWs by STS is challenging due to the contaminants. Despite these limitations, we will try to discuss the obtained results: The spectrum which is labeled with '1' in Figure 4.4 reveals a bandgap of approximately 1.9 eV. This value is in good agreement with the literature values for the two different lattice structures (wurtzite

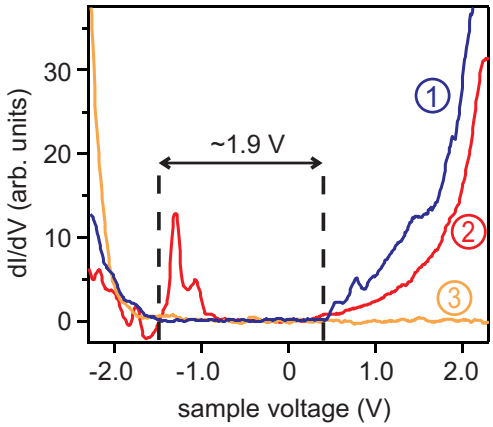

Figure 4.4: Typical tunneling spectra recorded at different positions on a NW; details are explained in the text.

structure: $E_{gap} = 1.85\,eV$, zincblende structure: $E_{gap} = 1.76\,eV$ [134]) and, thus, can be assigned to the CdSe NW. It has to be mentioned that the chosen voltage range does not allow to easily distinguish between the above mentioned different crystal structures and, thus, the mentioned electronic potential variations between wurtzite and zincblende type structures. This can be easily seen by comparing the voltage range of the spectrum with the energy offsets of the staggered bandstructure of wurtzite and zincblende: Reference [133] refers to a conduction band offset between the two lattice structures of 76 to 144 meV and a valence band offset of 30 to 59 meV (see also Figure 4.2 (c)). However, the intensity of the conductance onsets close to the bandgap is very weak, because of the used high setpoint voltage, as described in section 2.2.2. Thus, the energetic differences of the valence band and the conduction band of zincblende and wurtzite structures are too small to be observable in the chosen voltage range. Consequently, it is not possible to assign the spectrum to one of the two different crystal structures. Apart from these 'normal' spectra a second type of spectra can be identified which exhibits peaks in the bandgap (marked with '2' in Figure 4.4). These peaks indicate the existence of surface states, defects or impurities. While the former (surface states and defects) are probably caused by an imperfect passivation of the NW surface and imperfections in the lattice structure, the latter (impurities) might originate from the sample preparation under ambient conditions (e.g. impurities in the chloroform solution). Finally, the width of the extracted bandgap from the tunneling spectra is larger on some positions on the NW; a typical spectrum is shown in Figure 4.4 (labeled with '3'). According to the discussion above, this can not be ascribed to

the different lattice structures. A possible explanation for the observation of apparent large bandgaps in the tunneling spectra could be the existence of surface states deep in the bandgap: In contrast to shallow surface states, where electrons tunneling into theses states can quickly escape, the tunneling rate out of surface states lying deep in the bandgap is smaller. The close proximity of the tip to a region where the surface state is present might lead to a local charging and discharging of the surface state in dependence on the polarity of the tip, similar to what could be observed on GaAs in reference [135]. In general, it is remarkable that all three types of spectra are slightly shifted to negative voltages, leading to a conduction band onset at approximately 0.4 V. This early conduction band onset indicates n-type doping which is in agreement with previous studies: N-type doping of CdSe is well documented for, e.g., thin evaporated films of CdSe [136–138], for which electron concentrations of up to $10^{18}\,\mathrm{cm}^{-3}$ are reported. In addition, electrical transport measurements on single CdSe NWs have clearly revealed n-type behavior [139]. Moreover, in our experiments, n-doping may be further promoted by the sample annealing under UHV conditions, whereupon selenium vacancies are likely to be introduced into the NW [140]. In order to obtain information on the spatial variation of the electronic properties along the NW, one can map the spectra as a function of the position. This is illustrated in Figure 4.5 (b), where spectra along one complete NW are shown. This 1D conductance map has a length of ∼340 nm and consists of 1350 spectra. The electronic properties are highly inhomogeneous along the wire. Different types of spectra can be identified, whereas most of them can be ascribed to the three different types mentioned above. The spectra displayed in Figure 4.4 are highlighted by black arrows labeled with '1', '2' and '3' in Figure 4.5 (b). It is noticeable that spectra of type '2' mainly appear at the ends of the NW. The reason for that could be an incomplete passivation of the surface that leads to surface states in the bandgap which appear at around -1 V (red arrow in Figure 4.5 (b)). Since the expected length of the NWs is in the micrometer range [131], the preferential appearance of type '2' spectra at both ends of the NW can be caused by breaking of the NW after growth which causes an incomplete passivation. In the center of the NW an electronically more homogeneous region is visible with spectra resembling that of type '1'. Furthermore, it can be clearly seen in the 1D conductance map that the spectra do not show symmetric behavior for negative and positive voltages: Instead, most of the spectra are shifted to the negative voltage range, indicating n-type doping as already mentioned above. Except the accumulation of spectra with states in the bandgap at the ends of the NW, a direct correlation of the features in the spectra to the topography could not be observed. This is not surprising, since, first, due to the surface passivation

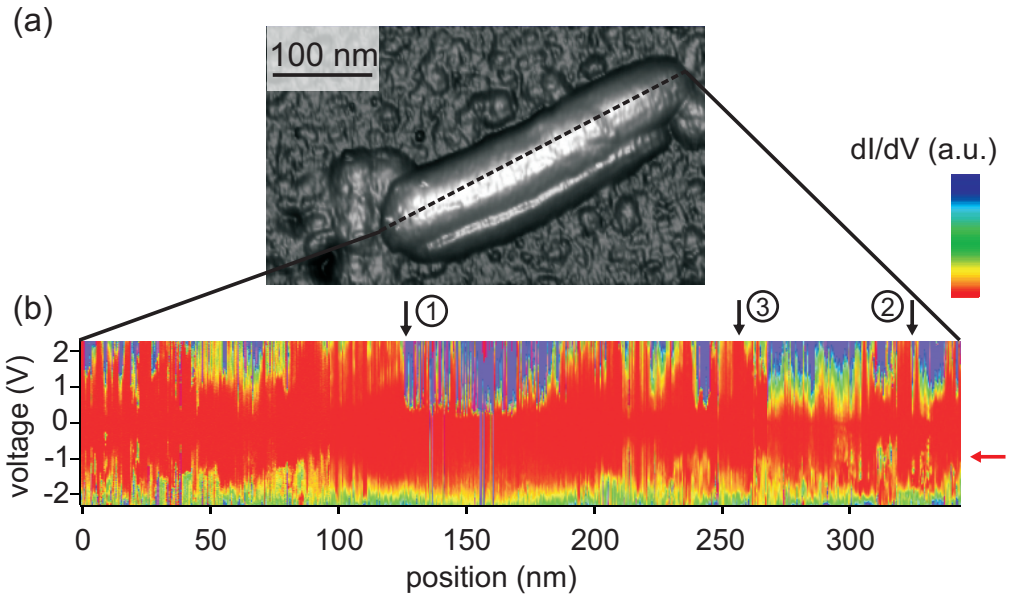

Figure 4.5: (a) STM image of a single NW. (b) 1D-STS map along the dashed line shown in (a) ($I_{setpoint}$=0.04 nA, $U_{setpoint}$=-2.3 V). Black arrows mark the position of the spectra extracted for Figure 4.4; the meaning of the red arrow is explained in the text.

with TOPO, atomic resolution on the NW could not be achieved (as already mentioned). Second, the features do not have to originate from the tip facing surface but from states in the volume of the NW.

4.4 Tunneling Current Induced Luminescence from Individual CdSe NWs

STM has been intensively employed to explore tunneling current induced luminescence in III/V semiconductor heterostructures, wherein the quantum structure is embedded in a larger bandgap material to achieve carrier confinement. However, there are only a few reports on STM-induced light emission from free-standing semiconductor nanostructures deposited on a metal substrate [39, 40, 49]. In these studies on CdSe/ZnS core-shell QDs, the light

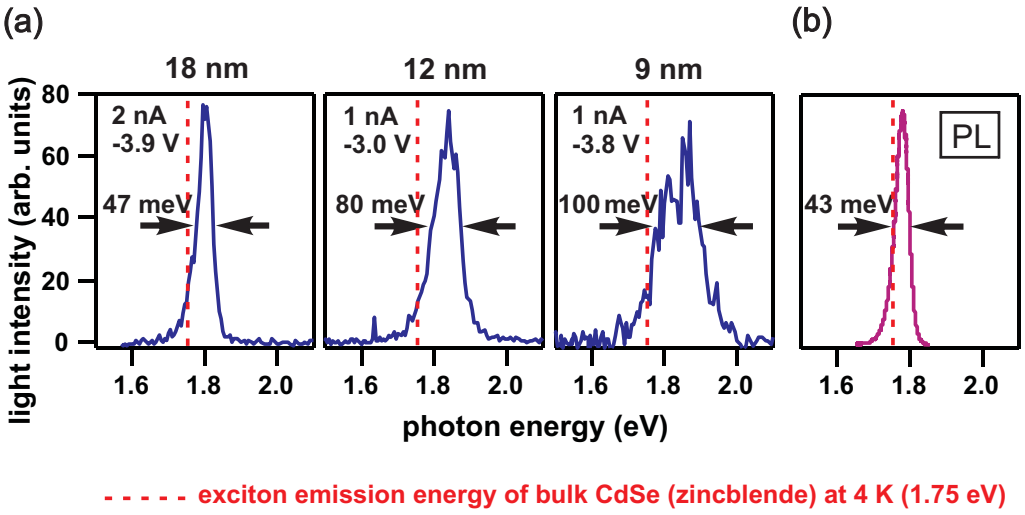

Figure 4.6: (a) Tunneling current induced luminescence spectra for NWs of three different diameters: 18 nm, 12 nm and 9 nm. (b) PL spectrum at 4 K.

emission couples to surface plasmons excited by the STM tip in the underlying metal substrate. However, since the existence and the spectral intensity of tip-induced plasmons strongly depend on the shape and composition of the tip and the substrate, it is rather difficult to control this type of emission [33, 47]. In contrast, STM-induced excitation of luminescence in individual CdSe NWs does not require the simultaneous presence of tip-induced plasmons as will be shown in this section. This is possible by ensuring an intimate electronic coupling between the NWs and the gold substrate, such that charge injection into the wires can easily occur.

Scanning tunneling current induced luminescence (STL) could be detected from individual NWs upon applying tunneling currents between 1 and 3 nA and bias voltages between -2 to -4 V (the tip potential is defined as 0 V). Light emission occurred exclusively in the negative bias range, corresponding to the injection of holes from the STM tip into the sample. Figure 4.6 (a) shows STL spectra recorded on three NWs with different diameters, which exhibit a prominent peak around 1.8 eV. In each case, no other luminescence features could be observed (in the detection range of 1.5 eV to 3.5 eV), including surface plasmons of the gold substrate which would emerge as a broad feature approximately from 1.4 eV to 2.5 eV [141]. The absence of plasmon coupling in these experiments is different from most other STL measurements on free-standing nanoscale objects [39, 40, 49]. Further proof that the light emission stems from the CdSe NWs can be gained from the similar-

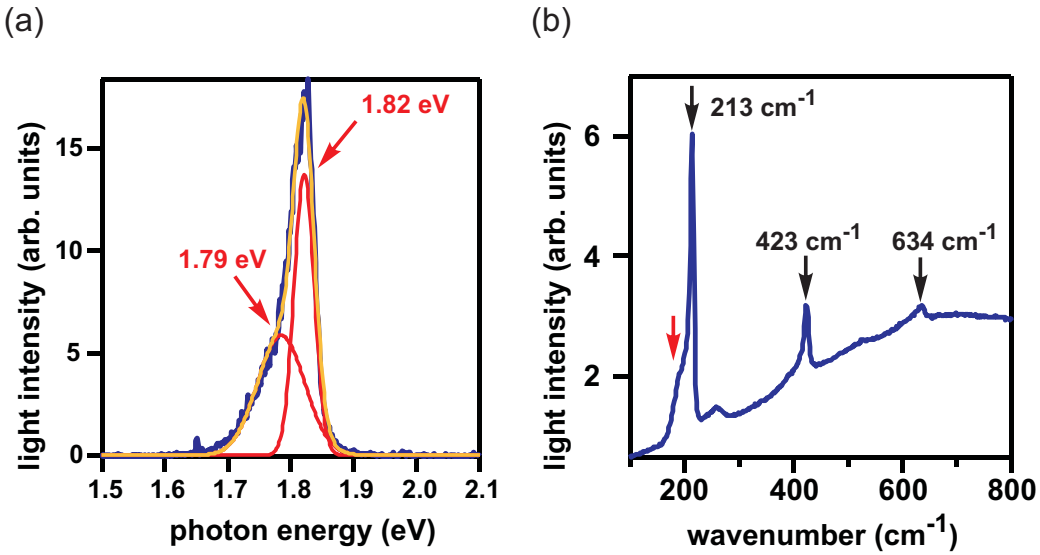

Figure 4.7: (a) STL spectra for a larger NW (diameter = 18 nm). The spectra can be fitted with two Gaussian functions (red lines); the orange curve represents the sum of the two Gaussian functions. (b) Raman spectra of a bundle of NWs (the red arrow is explained in the text).

ity between the STL spectra and those recorded by photoluminescence (PL) (Figure 4.6 (b)). In particular, comparison of the PL spectrum with the STL spectrum of the 18 nm wire reveals almost identical peak shape and width. This characteristic distinguishes the present STL spectra from typical other methods in which the light emission relies on the injection of charge carriers. For example electroluminescence (EL) spectra of single CdSe NWs [139, 142] display much broader emission peaks that stem from surface states introduced during the device fabrication. While local charge injection into one NW is a feature of STL, there is no definite evidence that the PL spectrum in Figure 4.6 (b) originates from a single wire, although the position of the laser spot (500 nm in diameter) was carefully chosen. The position of the PL peak (1.78 eV) indicates that the spectrum is dominated by a NW with larger diameter (>20 nm). The relation between diameter and emission energy derived by the STL measurements will be discussed later in detail.
We now turn to a more detailed description of the shape of the spectra. In Figure 4.6 (a) it can be seen that the peaks are asymmetric and that their energy depends sensitively on the wire diameter. In general, the peaks can be well fitted by a sum of two Gaussian functions, as demonstrated for the 18 nm wire spectrum in Figure 4.7 (a). The two Gaussian functions are shifted with

respect to each other by ∼30 meV. In order to identify the origin of this asymmetry, Raman measurements are presented in Figure 4.7 (b). The first order Raman band at 213 cm^{-1} (26 meV) can be attributed to the longitudinal optical phonon [134]. Consequently, the peaks at 423 (52 meV) and 634 cm^{-1} (79 meV) are assigned to the second and third order Raman band, respectively. Thus, the shoulder on the low energy side of the main STL peak in Figure 4.7 (a) is assigned to exciton-phonon coupling. It should be mentioned that in the Raman spectra an additional low energy shoulder (marked by a red arrow in Figure 4.7 (b)) of the first order band can be identified. This shoulder can be related to surface optical phonons [143, 144]. A further peak appearing at approximately 260 cm^{-1} might be related to impurities since it was not visible in all Raman spectra.
Some spectra showed the clear presence of two peaks, as can be seen in Figure 4.6 (a) for the 9 nm wire. This can be explained by the mentioned corrugation of the electronic potential along the NW axis caused by alternating zincblende and wurtzite sections which leads to a type II band alignment. The distance of the peaks in such spectra is approximately 50 meV as expected for the difference in energy of the indirect transition at the intersection of zincblende and wurtzite regions [133]. Further non dominant contributions to the low energy side of the peak might arise from additional recombination pathways involving shallow surface traps located in the bandgap. In Figure 4.8 (a) the high energy peak component is plotted as a function of the wire diameter. The emission energy increases with decreasing diameter indicating quantum confinement of the charge carriers. Recent studies have revealed that the bandgap of semiconductor NWs do not scale exactly with the inverse square-diameter as expected from the simple particle-in-a-box model. Instead, the bandgap of CdSe NWs was predicted to follow a $1/(\text{diameter})^{1.36}$ dependency [125, 145]. This dependency also accounts very well for the present higher energy peak component, as demonstrated by the plot in Figure 4.8 (b) where the red line represents the least square linear fit to the data, from which an emission peak minimum in the bulk limit $d \rightarrow \infty$ of E_{gap}^{bulk} ∼1.75 eV is derived. The resulting bulk bandgap of ∼1.75 eV is in excellent agreement with the free exciton energy reported for CdSe zincblende crystals at 4 K [134]. In comparison, the bandgap of wurtzite type CdSe crystals is considerably larger (∼1.83 eV) [134]. This means, that the excited light emission seems to originate from zincblende type structures and that the wurtzite type sections remain dark. In order to verify whether there are regions on the NW which do not emit, the intensity of the excited light is recorded as a function of the lateral position. This is illustrated in Figure 4.9 where an STM image of a NW (Figure 4.9 (a)) is compared to a photon map (Figure 4.9 (b)). The convolution of the NW and the STM tip causes the NW

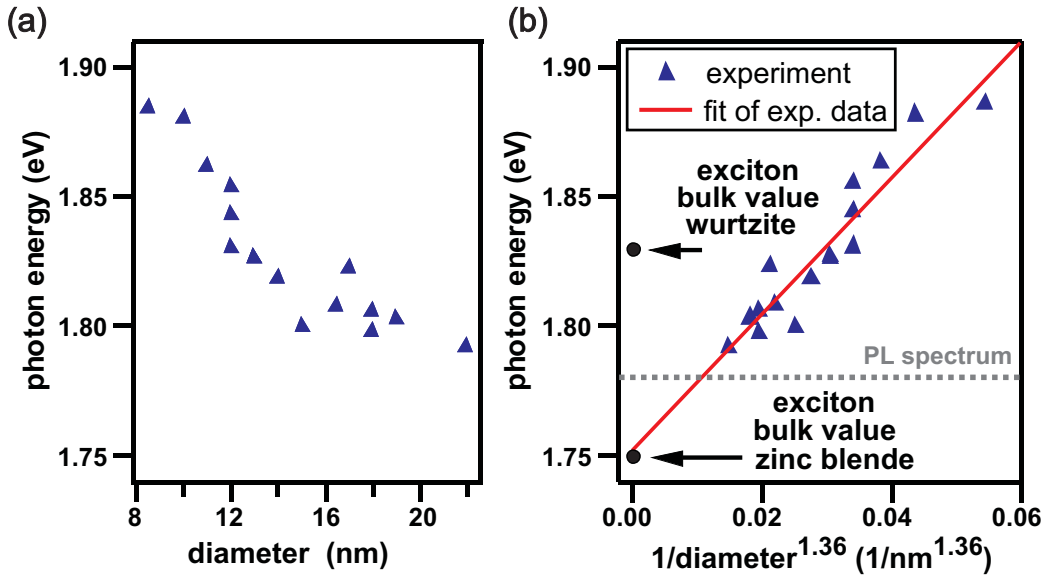

Figure 4.8: (a) Dependence of the photon energy on the diameter of the NWs. (b) Photon energy as a function of $1/(\text{diameter})^{1.36}$. The gray dotted line shows the energy of the PL peak of Figure 4.6 (b), which can be related to a NW with larger diameter (>20 nm).

to appear much broader (∼100 nm) than its nominal width (∼20 nm). This convolution complicates the analysis of the photon map. Nonetheless, we can conclude that some regions on the NW remain completely dark, while the emission could be reproducibly observed on other NW sections. Because of the diameter dependence of the photon energy (see Figure 4.8), we attribute the segments that lack light emission to wurtzite type CdSe segments. It should be mentioned that the photon map shown in Figure 4.9 (b) only illustrates the regions where charge injection leads to radiative recombination, which can also occur after diffusion and thermalization of the injected charge carriers. That means that even if charge carriers are injected into a wurtzite structure they can diffuse few tens of nanometers and recombine radiatively if a zincblende region lies within the diffusion path [146]. This is possibly the reason why the light emitting regions in Figure 4.9 (b) are wider (up to 50 nm) than the typical width of zincblende regions (few nanometers). The optical inactivity of the wurtzite type sections will be rationalized below.
It is furthermore worthwhile to compare the fitted slope of the diameter dependence of the peak energy to literature values [125]. According to both theory and experiments, the slope reflects the dimensionality of the system [147],

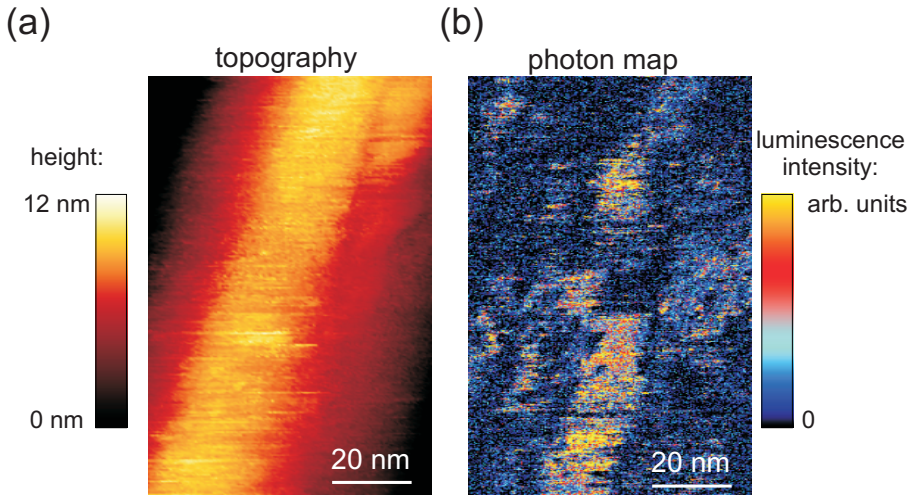

Figure 4.9: (a) STM image of a NW and (b) corresponding photon map (tunneling parameters: 1.5 nA, -3.5 V).

and the slope decreases with increasing dimensionality. Our measured slope of 2.6 eV $nm^{1.36}$ is larger than the value of 1.8 eV $nm^{1.36}$ documented in reference [125] for CdSe NWs, suggesting that in our measurements QD-like zincblende segments are responsible for the light emission. This assumption is in accord with the small segment length typical of the zincblende sections of just a few nanometers, as observed by TEM measurements (see Figure 4.2 (a)) [132]. Nonetheless, in Figure 4.8 (b) we have used the exponent of 1.36 established for NWs, since for CdSe QDs no values determined by luminescence studies are available, and previous studies on similar systems have revealed only a small difference between the exponents for the zero dimensional (0D) and the one dimensional (1D) case [147].
Regarding the mechanism underlying the STL generation from the NWs, the coupling of TIP modes to the wires [40, 49] can be ruled out, since we do not observe plasmonic emission on the gold substrate directly before and after the luminescence measurements. We ascribe the suppression of plasmon excitation on the substrate to the fact that tungsten tips are generally not capable of generating strong plasmonic emission [148, 149] and furthermore that surface adsorbed contaminations resulting from the sample preparation under ambient conditions are able to inhibit light emission [150]. Moreover, even if plasmons could be excited, their coupling to excitons in the NWs is unlikely, since the electric field of the plasmon (perpendicular to the substrate) is perpendicular to the transition dipole of the NW (parallel to the

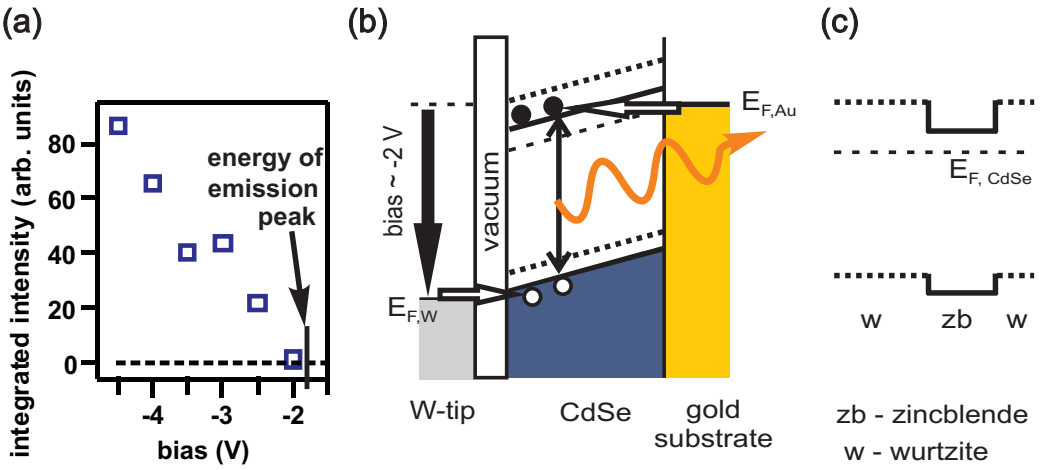

Figure 4.10: (a) Integrated luminescence intensity as function of sample voltage. (b) Schematic model of the excitation mechanism; $E_{F,Au}$, $E_{F,W}$ and $E_{F,CdSe}$ are the Fermi levels of the Au substrate, the W-tip and the CdSe NW, respectively; the conduction and valence band of wurtzite and zincblende type CdSe are indicated by the dashed and solid line, respectively. (c) Schematic sketch of the zincblende and wurtzite type bandstructure in the direction parallel to the CdSe NW.

wire axis) [151]. Likewise, impact ionization is unlikely to play a role, since this process usually sets in at voltages much larger than 2 V, and is furthermore polarity-independent [152]. However, all the STL characteristics observed in our experiments can be consistently explained by carrier injection from both, the gold substrate and the STM tip into the NW. Light emission from the NWs occurs only in the negative bias range for voltages below approximately -2 V (see Figure 4.10 (a)), i.e., for voltages exceeding the photon emission energy by more than 0.2 eV. In the positive bias range, no luminescence could be detected even for voltages as high as +10 V. This asymmetry can be explained by a combination of two aspects: First, the n-doping of the CdSe wires, which was already discussed in section 4.3. Second, the direct contact between the NW and the substrate and, hence, an intimate electronic coupling between wire and gold substrate which results in a pinning of the Fermi level of the NW to that of the substrate. The pinning might be further promoted by the sample annealing under UHV conditions which is expected to remove some of the TOPO molecules on the NWs. As a consequence of these two aspects, hole injection from the gold substrate into the NW is suppressed and attainable only from the tungsten tip (Fig-

ure 4.10 (b)).
In the scenario shown in Figure 4.10 (b), electrons would tunnel from the gold substrate into the conduction band of the NW, from where they recombine with holes injected from the tip into the NW. Such mechanism could explain why the light emission is restricted to the zincblende sections, as its conduction band edge lies approximately 100 meV below that of the wurtzite phase (Figure 4.10 (c)) [133], and therefore much closer to the Fermi level of the gold substrate. The Fermi level pinning inhibits a relative shift of the Fermi level of the gold substrate with respect to the conduction bands of the CdSe NW and thus injection into the wurtzite type segments is suppressed. This can be further supported by a recent theoretical study of Zhang et al. [153] who showed that for small InP NWs a type II to type I band alignment transition takes place leading to an accumulation of holes as well as electrons in the zincblende type segments. A similar transition might also occur in the case of CdSe NWs. Another contributing factor could be the strong permanent dipole inherent to the wurtzite sections, which is aligned along the NW axis [154–156]. This dipole may induce a spatial separation of the injected charge carriers, thus preventing their radiative recombination. However, since in both types of segments (wurtzite and zincblende) light emission can be suppressed by local non-radiative recombination of charge carriers via defect sites deep in the bandgap [157], one can not conclude that nonradiative sections are entirely composed of wurtzite sections.

Chapter 5

Topographic and Spectroscopic Studies of Iridium (III) Complexes on Metals and Thin Insulating Layers

The electronic properties of organic semiconductors have been receiving increasing attention in the last years. Although the semiconductor technology today is still dominated by single crystalline inorganic materials (e. g. Si, GaAs), semiconductor devices made from organic materials might present an attractive alternative mainly due to the advantages provided by chemical synthesis methods [10]. These sophisticated methods allow to precisely arrange an enormous variety of available organic building blocks and, hence, to tune their properties with a high degree of freedom. Most of the possible applications lie in the fields of electronic and optoelectronic devices such as organic field effect transistors [16,158] or organic light emitting diodes [15,159]. Here, one advantage of the use of organic semiconductors is, that some of them show high absorption coefficients and a large difference in emission and absorption energy due to the large exciton binding energy. As a result, very thin devices with high efficiencies can be fabricated. In addition, organic semiconductors can be deposited at low substrate temperatures, which allow the use of flexible substrates that enable the realization of novel devices, e. g. foldable displays.
Organic light emitting devices rely on thin organic layers that are sandwiched between two electrodes supplying the organic system with charge carriers. The subsequent recombination of the charge carriers in the organic thin film leads to luminescence. The further development of organic semiconductors in organic light emitting diodes requires a fundamental understanding of

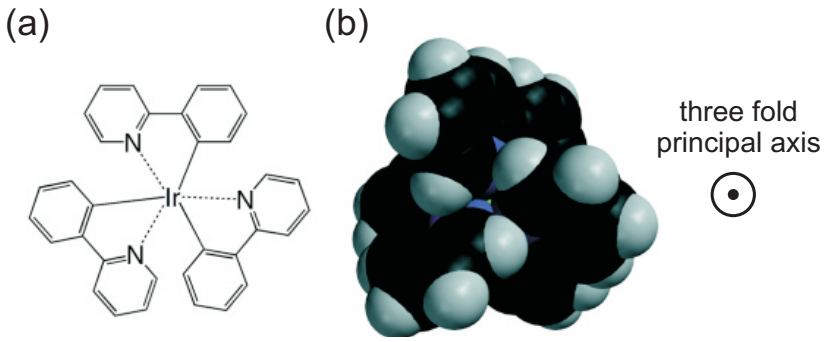

Figure 5.1: (a) Molecular structure of Ir(ppy)$_3$. (b) Space filling model. The direction of the three fold principal axis is perpendicular to the drawing plane as indicated on the right side. Figures adapted from [166].

the light excitation processes in thin organic layers down to the molecular level. Furthermore, by decreasing the size of the optically active part of the devices, the influence of individual molecules and their interaction to the metallic electrodes become more important [160]. Thus, a detailed understanding of the interaction between the molecular system and the adjacent metallic electrode at the interface is required. Moreover, the study of the ability of single molecules to emit light is of great interest, because molecules are single photon sources, which means that they only emit one photon at a certain time. Single photon sources could have a high potential in future application in quantum information technology [161,162]. A suitable tool for these investigations is scanning tunneling microscopy (STM)
In this chapter, dipolar iridium complexes (tris-(2-phenylpyridine)iridium(III)) (Ir(ppy)$_3$) [163–165] are investigated by means of scanning tunneling techniques. These iridium complexes are well suited for organic light emitting diodes, because, embedded in an appropriate matrix, their photoluminescent quantum yield reaches almost 100 % by effectively using singlet and triplet excitons [24]. Besides the structural characterization of the molecules the electronic properties as well as their ability to emit light excited by a tunneling current is studied. Figure 5.1 (a) and (b) shows the chemical structure and the space filling model of the used fac-Ir(ppy)$_3$ molecules. Three 2-phenylpyridine ligands are bound to an iridium ion in a propeller-like fashion.

5.1 Sample Fabrication

In order to investigate single molecules in a well-defined environment atomically flat surfaces are needed. Thus, ultra high vacuum (UHV) conditions are required for the sample preparation which is done in the preparation chamber attached to the low temperature STM (LT-STM) chamber. Single Au(111) and Rh(111) crystals were utilized as substrates. Clean and flat surfaces were prepared by standard UHV techniques using several cycles of Ar^+ sputtering and annealing. The preparation of Au(111) crystals was performed by Ar^+ sputtering for ∼20 min with an ion energy of 900 eV and an ion current of 19 μA detected at the sample. An annealing temperature of 850 K was used; for the subsequent cycles the annealing temperature was lowered to ∼830 K and ∼810 K to avoid that impurities originating from the bulk crystal reach the surface. $Ir(ppy)_3$ molecules were deposited onto the clean substrates by organic molecular beam epitaxy making use of sublimation of the molecules from a uniformly heated crucible. During deposition the substrate was kept at low temperatures (∼100 K - 140 K) to minimize surface diffusion of the molecules. The coverage of the substrate by the molecules was controlled by the deposition time and the crucible temperature and was checked by STM. For some samples the direct coupling of the molecules to the metallic substrates should be avoided. Therefore, two different types of insulating layers were used: KCl and a thin film of hexagonal boron nitride (h-BN). KCl was evaporated by electron bombardment. We deposited 1 to 2 monolayers (MLs) of crystalline KCl onto the clean Au(111) substrate held at room temperature. In order to prepare a complete ML of the h-BN-nanomesh the clean Rh(111) crystal is heated up and kept constant at 1100 K [167]. Subsequently, the Rh(111) substrate is exposed to borazine $(HBNH)_3$ at a vapor pressure of 3×10^{-7} mbar for 30 s. The samples are then cooled down followed by the deposition of the organic molecules.
A shutter which can be rotated above the sample during deposition offers the possibility to deposit the molecules as well as the KCl film only on one side of the sample surface. This results in a clean metallic part on the other half of the sample. On this clean metallic side, one can easily prepare the tip by carefully dipping it into the surface or by applying voltage pulses up to 10 V.

Prior to the STM investigation one has to identify the right evaporation temperature for the molecules under vacuum conditions. Furthermore one has to ensure that the molecules do not decompose during evaporation. This can be done by depositing the molecules onto test substrates at various evaporation temperatures; the coverage as well as the intactness of the

deposited molecules can then be investigated by laser desorption ionization (LDI) [168]. This analytical technique makes use of a pulsed laser which is directed onto the sample in order to transfer large molecules into the gas phase for mass spectrometry analysis. The sample consisting of the analyte absorbs the energy of the laser pulse, gets ionized and can be extracted by an electric field and analyzed by a mass analyzer (e. g. a time-of-flight (TOF) mass analyzer).

In the experiments performed in this thesis, $Ir(ppy)_3$ molecules were first evaporated in UHV onto several test substrates using different evaporation temperatures (T_{evap} between 220 and 400 °C). Afterwards the deposited material was analyzed by LDI. Additionally, the remains in the crucible after heating up to 400 °C were studied. Figure 5.2 (a) shows the mass spectrum of $Ir(ppy)_3$ molecules evaporated at $T_{evap} = 220$ °C. The quantity of the x-coordinate of the spectrum is mass m divided by charge z: m/z. The unit of this mass-to-charge-ratio is Thomson: $[m/z]$ =Th= u/e; u is the atomic mass unit and e the electron mass. Because of the utilization of electric fields for ion extraction, mass spectra can be either sensitive to negative or positive ions. All the experiments shown here were done in the positive mode. The appearance of the Na^+ and K^+ peaks at 23 Th and 39 Th, respectively, confirms that the spectrum is adequately calibrated. The main peak at around 655 Th can be assigned to the singly charged intact $Ir(ppy)_3$ molecule with an additional H atom (see also enlarged region shown in Figure 5.2 (b)). The splitting of this peak into several peaks lying close to each other ($\sim$654 - 658 Th) can be explained by the presence of different isotopes of Iridium. It is noteworthy that in addition there are signals around 502 Th and $\sim$530 Th, which imply the existence of some decomposed molecules consisting of $Ir(ppy)_3$ with one missing 2-phenylpyridine ligand with and without an additional Na atom. The comparison of the peak intensities shows that the amount of decomposed material is small. Finally, as demonstrated in Figure 5.2 (c) the remains in the crucible were analyzed after using an evaporation temperature of $T_{evap} = 400$ °C. The peak at 655 Th, indicating the presence of intact molecules, is hardly visible. Instead, the peak at around 503 Th gives evidence that by using high evaporation temperatures ($\sim$ 400 °C) only decomposed molecules remain in the crucible. As a result, this analysis allows to specify an upper limit for the evaporation temperature ($<$ 320 °C) and verifies that, by using a temperature below this limit, the majority of the molecules are still intact.

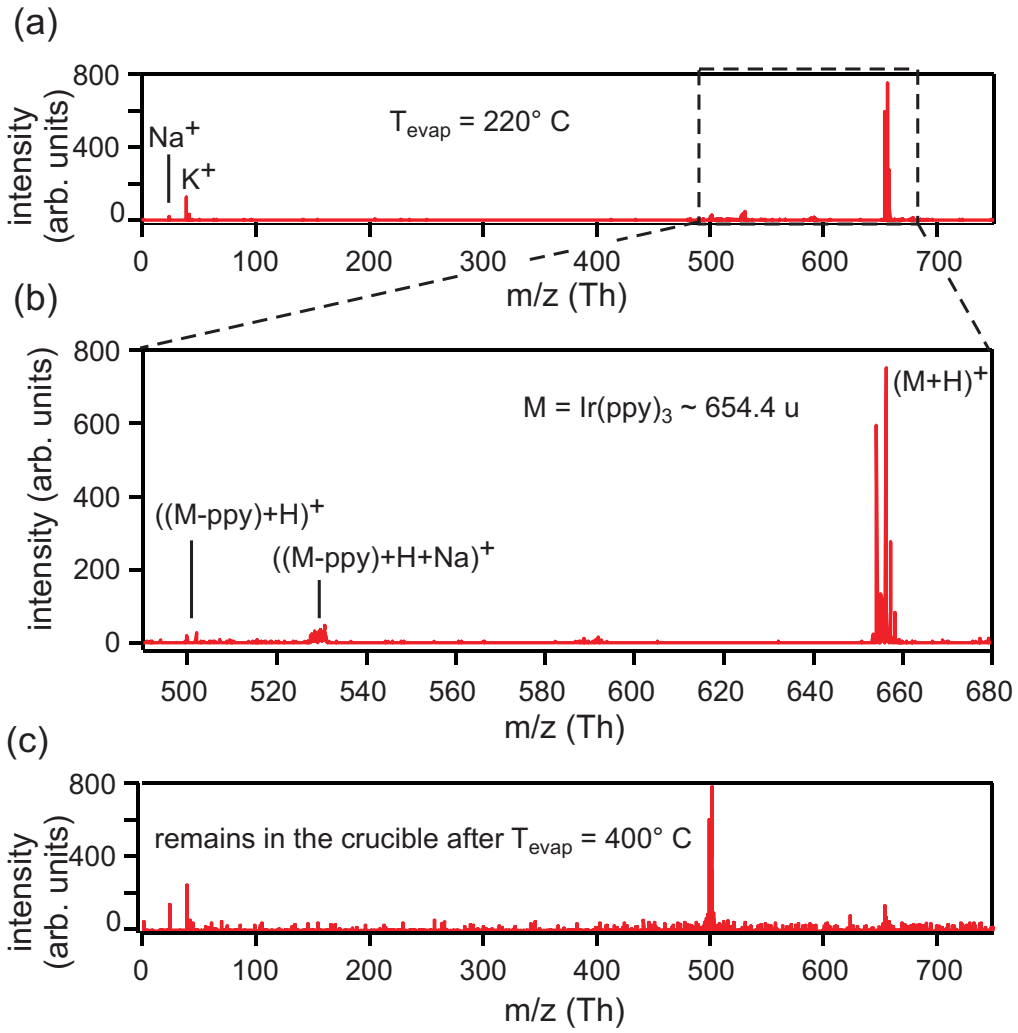

Figure 5.2: (a) LDI-TOF mass spectrum of Ir(ppy)$_3$ molecules evaporated at T_{evap} = 220 °C. (b) Detail of the mass spectrum shown in (a). The origins of some peaks are indicated. (c) Mass spectrum of Ir(ppy)$_3$ molecules left in the crucible after evaporation at T_{evap} = 400 °C.

5.2 Ir(ppy)$_3$ on Au(111) Substrates

In order to systematically analyze the structure and electronic as well as optical properties of the molecules, Ir(ppy)$_3$ molecules were first evaporated onto metallic single crystals. Even though light emission from the molecule on the metal substrate is not expected because of the close vicinity of the metal substrate [169], one can get fundamental information about the structural and

electronic properties, before moving to the more complex molecule-insulator system. In this section the structural arrangement of $Ir(ppy)_3$ on Au(111) will be investigated. First, this section describes the structural arrangement of the molecules followed by a discussion about the electronic and optical properties of single molecules on Au(111). The reason for choosing Au(111) as a substrate is its high plasmonic emission that will be of interest for the STL investigations, as well as its chemical inertness.

5.2.1 Structural Arrangement

The preparation conditions are specified in section 5.1 (deposition of $Ir(ppy)_3$ at T_{evap} between 220 and 230 °C for 30 min). Prior to the transfer into the STM the sample was annealed to ∼ 190 K for a few minutes. Figure 5.3 (a) and (b) show typical STM images. Small elongated protrusions (apparent height ∼1.5 Å) arranged in small clusters can be identified. In addition, one can sporadically observe larger islands, with apparent heights of approximately 5 Å (see Figure 5.3 (b)). In Figure 5.3 (c) high resolution STM images of these different types of structures and the corresponding line profiles are shown. In the following we refer to them as structures of type 'A' and type 'B', respectively. Most of the structures appear at the elbow sites of the fcc domains, only a few are situated at the hcp domains of the Au(111) substrate similar to what could be observed in reference [170]. Since the LDI experiments have shown mainly intact $Ir(ppy)_3$ molecules we assign each elongated protrusion in the STM image to one single molecule as depicted in Figure 5.4. It is remarkable that the structures of type 'A' tend to form small flower-like ensembles (formed by up to five molecules) as can be seen in the two images on the left side of Figure 5.3 (c) for two and four molecules. Figure 5.4 illustrates the formation of these structures for different numbers of molecules. While for a small number of molecules (< 5) flower-like structures can be observed, disordered ensembles of molecules are found for higher numbers of assembled molecules (see Figure 5.3 (a) and (b)). Isolated molecules are hardly observed on the surface. This clearly indicates an attractive interaction between the molecules. In order to explain the elongated shape of the structures of type 'A', we compare the observed shape in the STM measurements with the molecular model. A possible absorption geometry is shown in Figure 5.4: The 3-fold principal axis (illustrated in Figure 5.1) of the molecule stands parallel to the surface. The elongated shape might be explained by the adsorption of two of the 2-phenylpyridine ligands to the surface resulting in one 'visible' protruding ligand. Because of the tendency of the molecule to adsorb with the phenyl rings close to the surface the shape of the molecule might be slightly deformed. Furthermore, one has to note that the molecular

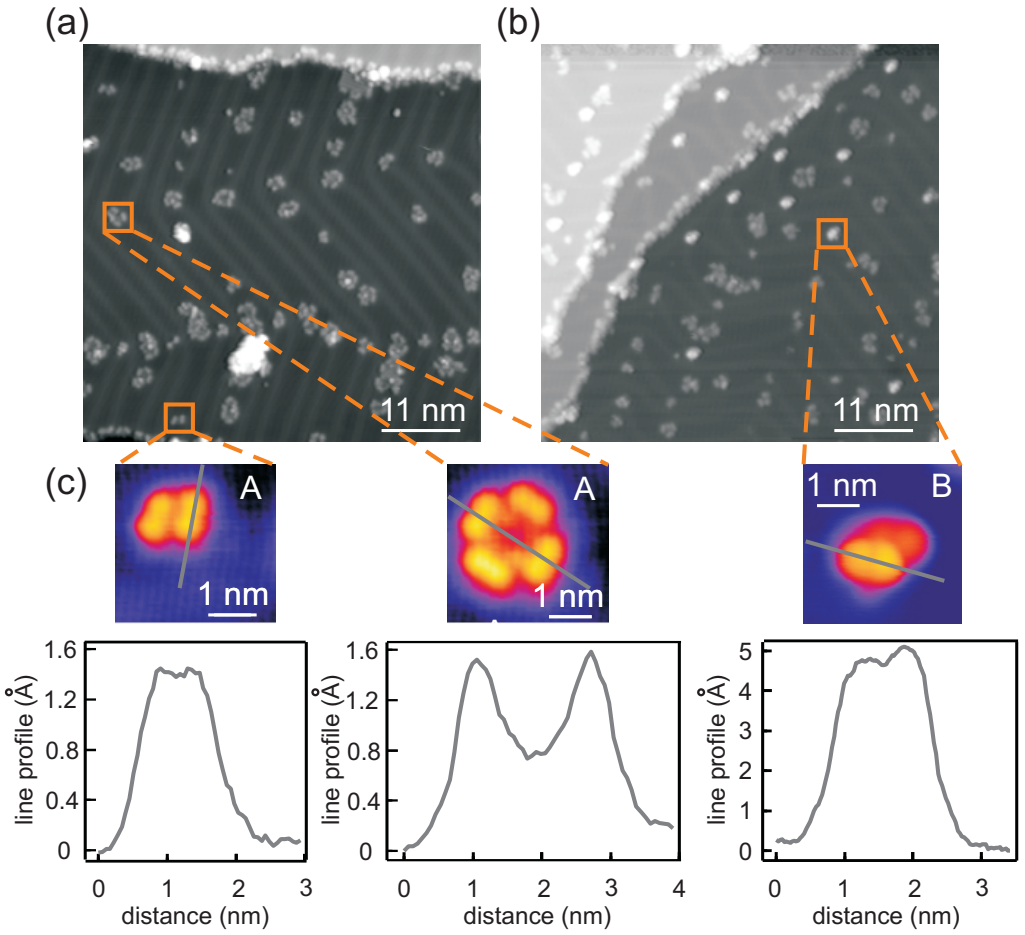

Figure 5.3: (a) Overview STM image of Ir(ppy)$_3$ molecules on Au(111) (I_{tunnel}=10 pA, U_{tunnel}=-0.9 V). (b) Overview STM image from a different position illustrating the additional presence of higher islands (type 'B') (I_{tunnel}=6 pA, U_{tunnel}=2 V). (c) High resolution images of some of the structures of type 'A' and type 'B'; the corresponding line profiles are shown in the lower row (I_{tunnel}=6 pA, U_{tunnel}=1 V).

structure in its gaseous form has been used for the molecular model shown in Figure 5.4 and interactions of the molecules with the surface have been neglected. By comparing the dimensions of the larger islands of type 'B' (see Figure 5.3 (c), right image) with the dimensions of single molecules we assume that islands of type 'B' might represent several molecules lying close to each other, forming small three dimensional (3D) clusters.
However, the analysis of the STM images does not allow to unambigu-

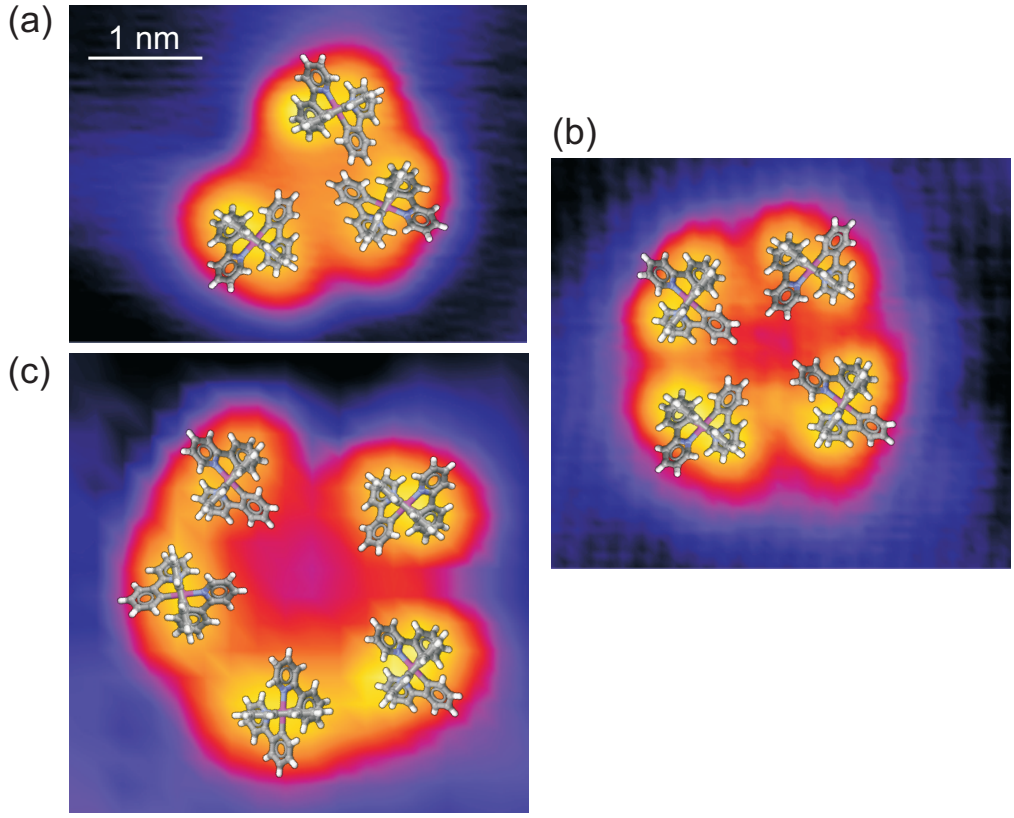

Figure 5.4: Ensembles of the structures of type 'A' as a function of the number of molecules for (a) three, (b) four and (c) five molecules, respectively; a possible adsorption geometry of a gas phase model is indicated (the molecular model is simulated with *Mercury* [171]).

ously identify the molecular structure. Thus, we can not exclude completely that the observed structures are fragments of the decomposed molecule even though the molecules are expected to be highly robust caused by the presence of the donor-acceptor properties of the 2-phenylpyridine ligands which is expected to stabilize the complex [172]. In a similar study, Gersen et al. [172] investigated the dissociation of an Iridium(III) complex containing 2-phenylpyridine ligands and one acetylacetonate ligand ($Ir(ppy)_2(acac)$) on Cu(110). They observed the dissociation of the complex on the Cu(110) surface and relate it to the removal of the acetylacetonate ligand. However, no explicit proof was given that the dissociation of the molecules had not already occurred in the crucible. Thus, in order to unambiguously assign the observed

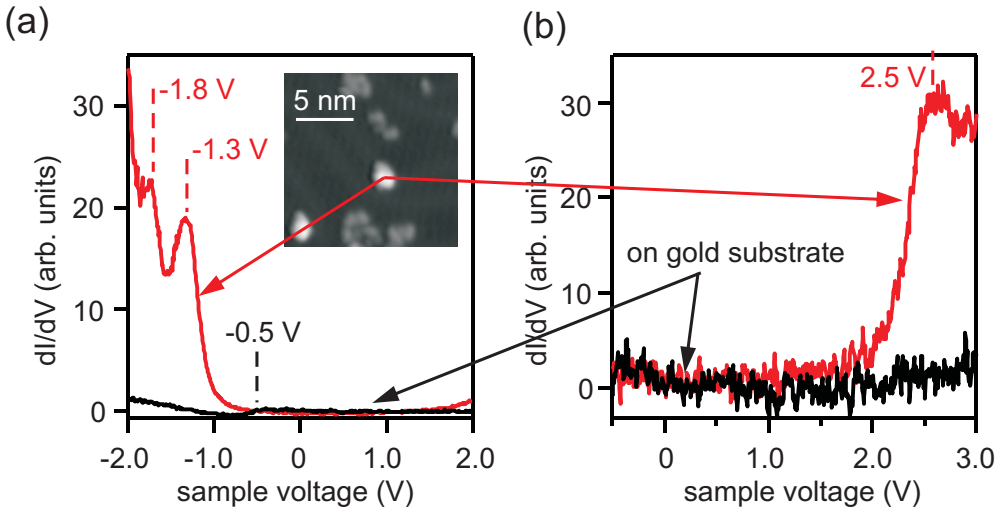

Figure 5.5: Tunneling spectra taken on the bare Au(111) substrate (black line) and on a small cluster of Ir(ppy)$_3$ (corresponding to structures of type 'B'). (a) Spectra in the negative voltage range; the labeled peaks are discussed in the text. The position of the spectrum is shown in the STM image in the inset ($I_{setpoint}$=40 pA, $U_{setpoint}$=2 V). (b) Spectra in the positive voltage range ($I_{setpoint}$=40 pA, $U_{setpoint}$=3 V).

structures to intact or dissociated molecules further experiments would be required. Finally, we compare the arrangement of Ir(ppy)$_3$ on Au(111) as shown in this thesis with the work of others [166] where the molecules had been deposited onto Cu(111). In this previous study, the authors observe only single structures by STM measurements and assign them to individual isolated molecules. In contrast, as shown above, only ensembles of molecules have been observed in this thesis. This ambiguity between the results on Cu(111) and ours calls for further studies.

5.2.2 Electronic Properties

In Figure 5.5 the electronic properties of Ir(ppy)$_3$ molecules are presented. Figure 5.5 (a) and (b) compares the differential conductance on the bare Au(111) substrate with that on the molecules. In the inset of Figure 5.5 (a) the position of the scanning tunneling spectroscopy (STS) spectra in the STM image is indicated. The probed structure can be attributed to a type 'B' structure as it was discussed in the last section. The spectrum recorded on the Au(111) substrate does not show any distinct features, only a small

step at around -0.5 V below the Fermi level is visible. It represents the Au(111) surface state [173]. The spectra on the molecule show several distinct features: For negative voltages (Figure 5.5 (a)) two peaks at around -1.8 and -1.3 V can be observed. For the unoccupied states at positive voltages a dominant feature at 2.5 V can be detected. Even though the interaction of the metal substrate and the molecule is expected to influence the highest occupied molecular orbital (HOMO) and lowest unoccupied molecular orbital (LUMO) orbitals of the free $Ir(ppy)_3$ molecule, the appearance of peaks in the spectrum indicates tunneling into discrete states of the molecule. Since tunneling through the LUMO and HOMO states leads to charging of the molecule, the observed peaks correspond to the negative (NIR) and positive ion resonances (PIR) of the absorbed molecule. Thus, the peaks at negative voltages might be related to the PIR (-1.3 V) and to the subsequent state (-1.8 V). The peak at 2.5 V is assigned to the NIR. This yields an energy difference between the PIR and NIR of ~ 3.8 eV. The PIR-NIR gap appears higher than the known HOMO-LUMO gap of the molecule in the gas phase (~ 3.5 eV [15, 174]). This is expected due to the additional charging of the molecule caused by the STS measurement. The fact that discrete levels are observed in STS indicates that the top molecule probed by STS is decoupled from the metal surface by the underlying molecules. In contrast, spectra on structures of type 'A' do not show any distinct features in this voltage range.

5.2.3 Optical Properties

In Figure 5.6 scanning tunneling current induced luminescence (STL) spectra of the bare Au(111) substrate and of the molecule are shown. Broad plasmonic emission can be detected on the Au(111) surface for negative and positive sample voltages (black lines in Figure 5.6 (a) and (b), respectively). In contrast, the spectra recorded on a structure which was assigned to a structure of type 'B' (similar to the structure shown in the inset of Figure 5.5 (a)) show much weaker emission, but still a similar spectral appearance (red lines in Figure 5.6 (a) and (b), respectively). As expected, luminescence attributed to transitions in the molecular states can not be observed, because of the close proximity of the metallic substrate, which favors nonradiative light emission [169, 175]. Instead, the weaker plasmonic emission compared to the Au(111) substrate can be explained by the increased distance between the tip and the metallic substrate [42]. On the Au(111) substrate the distance between tip apex and metal substrate is smaller, whereas on top of the island the distance is larger.

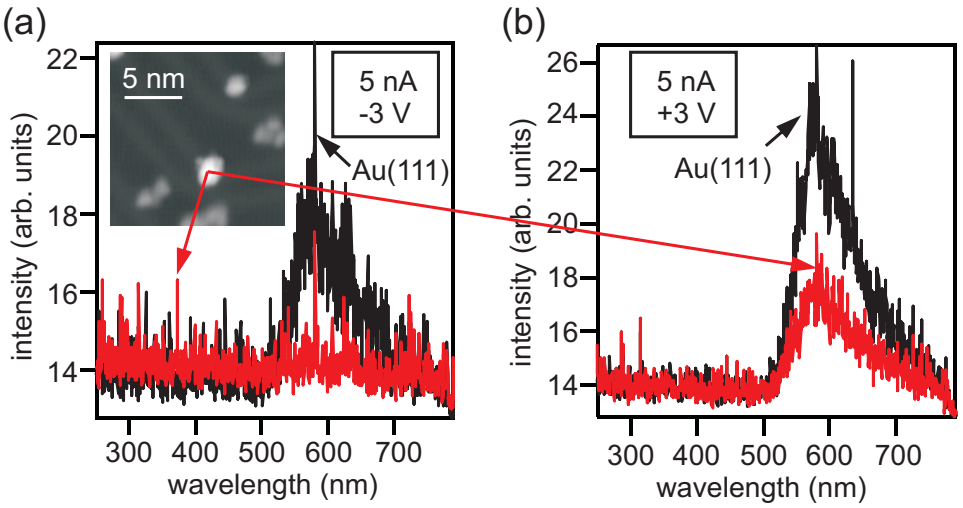

Figure 5.6: STL spectra for (a) negative and (b) positive sample voltage, recorded on the bare Au(111) substrate (black line) and on the structure assigned to a structure of type 'B' (red line) (the STM image in the inset of (a) shows the position where the spectra are recorded).

5.3 Ir(ppy)$_3$ on Thin Insulating Layers

In the previous section, it was shown that the deposition of Ir(ppy)$_3$ on metallic substrates does not allow to excite luminescence from single molecules probably caused by the strong interaction of the molecules to the substrate. A possible path to decouple the molecules from the metal is to deposit them on ultrathin insulating layers, which still allow tunneling. This will be illustrated in this section.

5.3.1 Ir(ppy)$_3$ on KCl/Au(111)

The evaporation of KCl on a metallic substrate leads to a homogeneous flat epitaxial layer. The large bandgap of bulk KCl (8.5 eV) is expected to decouple electronically the molecules from the metallic substrate similar to what was shown in reference [176]. However, it turned out, that the deposition of Ir(ppy)$_3$ molecules on KCl, leads to high molecular diffusion and to large clusters of molecules on the KCl layer. This might be explained by the interaction between the molecules and the substrate, which is expected to be decreased in the case of a thin insulator between the molecule and the metallic substrate [172,177,178]. This decreased molecule substrate interaction on

the KCl layer in comparison with the one on the bare gold surface leads to high diffusion and to the formation of large clusters of molecules.
In order to avoid the diffusion of molecules resulting in large non-ordered clusters, we have changed the substrate to an insulator that homogeneously covers the entire metal substrate and which provides intrinsic potential barriers to trap the molecules on the surface as detailed in the following section.

5.3.2 $Ir(ppy)_3$ on h-BN-nanomesh/Rh(111)

This section deals with the deposition of $Ir(ppy)_3$ on a thin film of h-BN on Rh(111). The resulting surface corrugation of the nanomesh strongly inhibits the mobilization of molecules even at room temperature [179]. In this section, first, the properties of the h-BN nanomesh will be described, followed by a characterization of the morphology after the deposition of $Ir(ppy)_3$ molecules on the h-BN nanomesh. Finally, the ability of exciting intrinsic light emission from the molecules is investigated.

The Boron Nitride Nanomesh

The h-BN nanomesh [167] is a wide bandgap material (5 - 6 eV [180]) and surfaces can be homogeneously and nearly defect free covered by one ML of boron nitride (see Figure 5.7). It shows a high stability even under exposure to ambient atmosphere and it is very inert, thus, making it an attractive template [181]. The lattice mismatch with the underlying Rh(111) substrate leads to a highly regular superstructure with a periodicity of the cavities of 3.2 nm. More precisely, the corrugated surface is the result of repelling and attracting forces between the N and B atoms and the underlying metal substrate. The cavities present regions where the nanomesh is bond strongly to the underlying Rh(111) crystal. In contrast, the areas at the ridges are only bound to neighbored nanomesh atoms by strong cohesive forces within the h-BN nanomesh [179]. This also strongly influences the electronic properties of the nanomesh [182]. The corrugation can be utilized as a periodic array to immobilize and trap molecular adsorbates due to strong confining potentials at the edges of the cavities. Berner et al. [179] found that vapor deposited naphthalocyanine molecules become immobilized even at room temperature due to the cavities of the nanomesh. Another study of Dil et al. [183] investigated the nature of this trapping mechanism by photoemission of adsorbed Xe. They proposed strong bonding sites at the rim of the cavities resulting in a ring of in plane dipoles which are expected to be responsible for the trapping of molecules. The nanomesh was grown on a clean Rh(111) surface

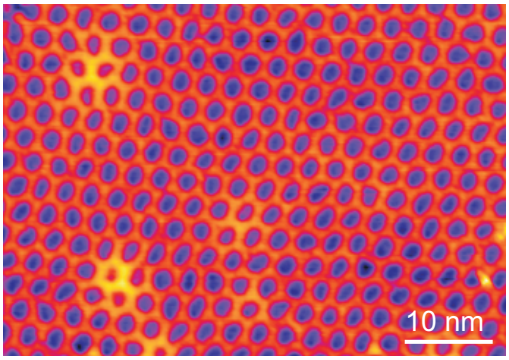

Figure 5.7: STM topography of h-BN on Rh(111) (I_{tunnel}=6 pA, U_{tunnel}=-3 V).

as already described in section 5.1 which resulted in a surface similar to the one shown in Figure 5.7. The occasional appearance of protrusions as shown in Figure 5.7 is probably caused by subsurface defects [184, 185].

Morphologic Characterization

Ir(ppy)$_3$ molecules were deposited onto the h-BN nanomesh/Rh(111) substrate at an evaporation temperature of T_{evap} = 250 °C, while the substrate was held at low temperature (135 K). Figure 5.8 (a) illustrates the topography of the sample after the evaporation. In general two types of structures can be identified on the surface which are mainly positioned in the cavities of the nanomesh. Even though the identification of these structures is not straight forward we will try to give a first insight into the relation between the STM images and the underlying molecular structure. First of all, several large islands can be observed in Figure 5.8 (a), which all show a stripe like pattern. Figure 5.8 (b) shows a high resolution image of one of these islands. Since these stripes are frequently observed on the islands and are pointing in different directions for different islands, it can be excluded that they stem from tip artifacts. The molecular model shown in Figure 5.8 (b) illustrates that the dimensions of these islands can not correspond to a single molecule. Furthermore, they have different lateral dimensions, thus, we attribute them to small clusters of several molecules. Secondly, small ring shaped structures (see Figure 5.8 (c)) can be frequently observed in the cavities of the h-BN nanomesh. The comparison of these structures with the molecular structure of Ir(ppy)$_3$ indicates that the imaged rings might represent single Ir(ppy)$_3$ molecules. A possible adsorption geometry is demonstrated in Figure 5.8 (c) using the molecular model in gas phase, where the three fold principal axis

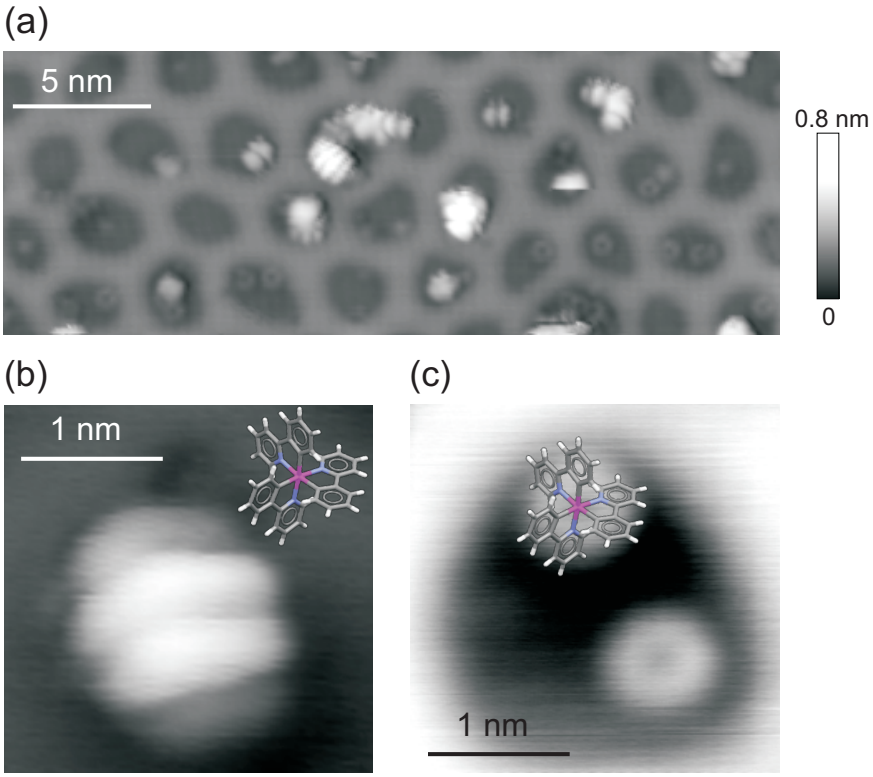

Figure 5.8: (a) STM topography of $Ir(ppy)_3$ deposited on h-BN on Rh(111) (I_{tunnel}=6 pA, U_{tunnel}=-2.0 V). (b) High resolution STM image of an islands (I_{tunnel}=6 pA, U_{tunnel}=+1.7 V). For comparison of the geometry, a molecular model is shown. (c) High resolution image of a small ring shaped structure and a possible corresponding molecular structure (I_{tunnel}=17 pA, U_{tunnel}=-1.6 V) (the molecular model is simulated with *Mercury* [171]).

of the molecule stands roughly perpendicular to the sample surface. Thus, the STM investigations demonstrate that by using the h-BN nanomesh as an insulating layer, it is possible to obtain single $Ir(ppy)_3$ molecules.

Optical Properties

One reason for the deposition of $Ir(ppy)_3$ on the h-BN nanomesh is the insulating character of the nanomesh which was expected to sufficiently decouple the molecules from the metallic substrate in order to excite STM induced intrinsic luminescence. Therefore, the STM tip was positioned on top of one of the ring shaped structures which we attributed to a single molecule (see previous section). We recorded spectra for positive and negative sample

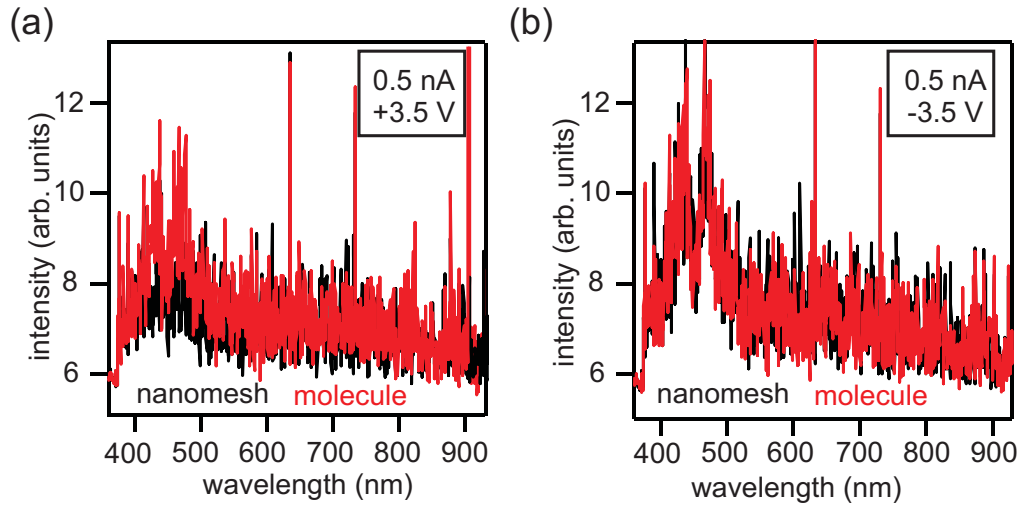

Figure 5.9: Tunneling current induced luminescence on top of Ir(ppy)$_3$ molecules deposited on the h-BN nanomesh on Rh(111): Spectra recorded at (a) positive sample voltage and (b) negative sample voltage on a nanomesh cavity (black curve) and on the molecule (red curve), respectively.

voltages as shown in Figure 5.9 (a) and (b), respectively. On the nanomesh as well as on the molecule broad spectra can be observed for positive and negative sample voltages. This broad emission is typical for plasmonic emission. The comparison of the shape of the spectra on the cavities of the nanomesh and on top of the molecules does not show any significant difference. Thus, no intrinsic emission originating from the molecule itself can be detected. The small change in the intensity of the spectra recorded on the molecule and on the bare cavity of the nanomesh might be again related to a variation of the distance between tip and metallic substrate [42]. In the cavity the tip is closer to the metallic substrate whereas on top of the molecule the distance between metal substrate and tip apex is larger. In order to further verify whether molecular luminescence can be excited or not, photon maps, which record the total intensity of emitted light as a function of the lateral position, are recorded. While Figure 5.10 (a) shows the STM topography of an individual Ir(ppy)$_3$ molecule; Figure 5.10 (b) illustrate the photon maps for positive and negative voltage, respectively. The number of counts corresponds to the number of photons detected by the avalanche photodetector. The photon maps are filtered by a Gaussian smooth to visualize small changes in the light intensity. These photon maps do not show any enhancement of luminescence on top of the molecule; in fact, for negative sample voltages the light intensity slightly decreases on top of the molecule,

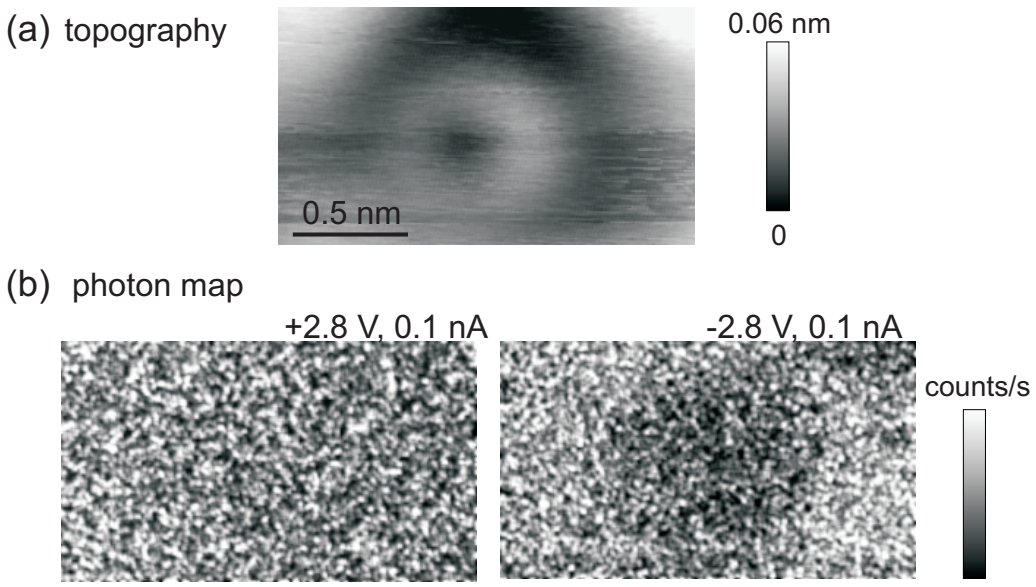

Figure 5.10: (a) STM topography of an individual $Ir(ppy)_3$ molecule (I_{tunnel}=0.1 nA, U_{tunnel}=-2.8 V). (b) Corresponding photon map for positive and negative sample voltage, respectively.

which might be again related to a possible increase in the distance between the tip and the metallic substrate. The STL spectra as well as the photon maps demonstrate that no molecular luminescence can be detected from a single molecule. A possible reason which might explain the suppression of molecular light emission could be a non sufficient decoupling of $Ir(ppy)_3$ from the substrate: Although the h-BN bulk material is an insulator, the h-BN single layer on Rh(111) shows a strong hybridization between N and B atoms with the metal atoms underneath in its bandgap [182]. Furthermore, the close vicinity of the metal substrate might effectively quench any emission [169, 175]. In fact, several STL studies document the importance of a sufficient decoupling of the investigated molecule and the metallic substrate in order to excite molecular luminescence associated with HOMO - LUMO transitions: Dong et al. [44] were able to observe luminescence of porphyrin molecules by using a molecular multilayer as a decoupling barrier. Another study [45] used an ultrathin NaCl film in combination with several molecular layers of C_{60} in order to successfully decouple the molecules from the metallic substrate. Moreover, the investigation of nanoscale pentacene crystals on thin KCl layers with STL showed that light emission only occurs in crystals exceeding a height of 1.5 nm [48]. On smaller crystals as well as on single

molecules no luminescence could be found.

5.4 Outlook: Ir(ppy)$_3$ on Multilayers of C_{60}

One possibility to increase the distance between the emitter molecule and the metallic substrate is to utilize a multilayer of a different molecule as a decoupling barrier ('host system'). The guest molecule, i. e. Ir(ppy)$_3$, could then be deposited on top of this layer. The multilayer can be realized by e. g. extended molecular layers of C_{60} molecules. By this means, a larger distance of the investigated molecule to the metallic substrate is given. In this section, preliminary results of Ir(ppy)$_3$ on a multilayer of C_{60} are presented. Several layers of C_{60} molecules were deposited on a Au(111) substrate prior to the deposition of Ir(ppy)$_3$ on top of the multilayer. The STM image presented in Figure 5.11 (a) shows Ir(ppy)$_3$ molecules (bright protrusions) on a multilayer of C_{60} molecules. The simultaneously recorded total intensity of light is illustrated in Figure 5.11 (b). It can be seen that bright spots appear on the left side of the photon map (indicated by white circles) which can be related to a high light intensity. The left spot is close to several Ir(ppy)$_3$ molecules which might indicate photon emission originating from Ir(ppy)$_3$. Even though, spectroscopic characterization is required to unambiguously assign the observed luminescence to Ir(ppy)$_3$, these preliminary results show great promise for future experiments based on light emission of 'guest - host systems' in the STM.

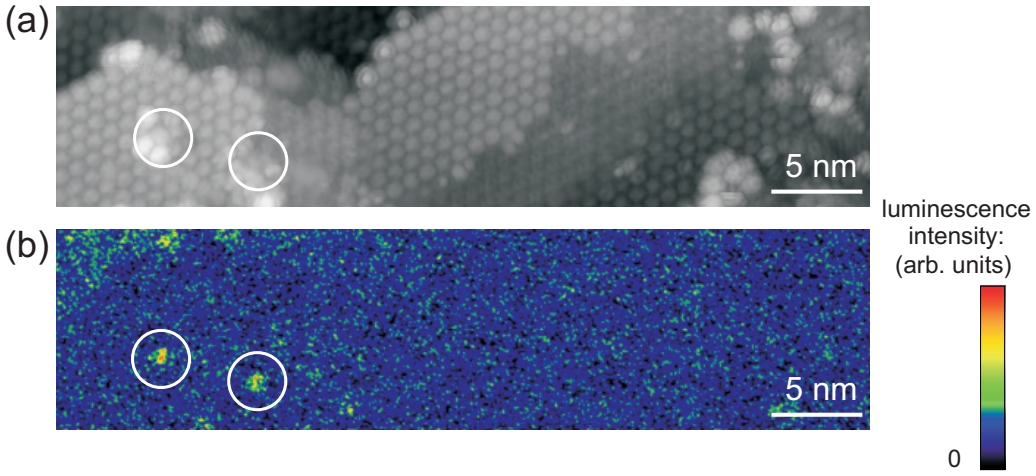

Figure 5.11: (a) STM image illustrating Ir(ppy)$_3$ molecules on multilayers of C_{60}. (b) Simultaneously detected photon map (I_{tunnel}=30 pA, U_{tunnel}=-4 V). The white circles in (a) and (b) indicate positions of high local light intensity.

Chapter 6

Summary and Outlook

In this thesis, the unique spatial resolution of scanning probe techniques is utilized in order to gain insight into the morphologic as well as electronic and optical properties of inorganic and organic semiconductor nanostructures. Three different nanoscale systems all fabricated by different methods are investigated:

- InAs/GaAs quantum dots (QDs) grown by molecular beam epitaxy (MBE) in ultra high vacuum (UHV)
- CdSe nanowires (NWs) grown by the solution-liquid-solid (SLS) method
- $Ir(ppy)_3$ molecules deposited by sublimation from an evaporation cell in UHV onto crystalline surfaces

In the first part of this thesis MBE grown InAs/GaAs(001) QDs are discussed that are investigated by atomic force microscopy (AFM) as well as scanning tunneling microscopy (STM) techniques. First, the electronic properties of large QDs are studied with scanning tunneling spectroscopy (STS). The obtained spectra show evidence of discretization of the electronic states due to quantum confinement. In addition, strong local variations of the magnitude of the bandgap on individual QDs can be observed. While the bandgap is mainly constant in the center, it increases towards the outer part of the QD. The latter increase is attributed to intermixing of In and Ga atoms. Furthermore, the symmetry of the wavefunction (s-type) of the discrete energy states might also contribute to the observed small constant bandgap in the center of the QD. Moreover, in-situ etching experiments are performed to systematically remove material from as grown InAs/GaAs(001) QDs. AFM as well as STM measurements show that in the course of the etching process, steep multifaceted islands disappear and only flat islands

exhibiting {137} facets can be observed. For long etching times small two dimensional (2D) islands appear frequently on the surface. These observations indicate that the island shape evolution during etching commences in reversed order compared to the shape evolution that occurs during growth. This reversibility confirms that the etching process is strongly influenced by thermodynamic factors. The mechanism of the material removal from the QDs is investigated as well. We find that the shape transition of the QDs is not determined by direct etching, but by the etching of the wetting layer (WL) and the subsequent diffusion of In atoms away from the QDs onto the bare GaAs(001) substrate, thus rewetting the substrate.
The presented results form the basis for more detailed etching experiments, for which it would be interesting to vary the etching rate to study the influence of kinetic and thermodynamic factors. While the low etching rate used in this study indicates a shape transition close to thermodynamic equilibrium, a faster etching might promote kinetic factors and suppress the observation of a backtransition. These experiments would reveal the interplay of thermodynamics and kinetics of heteroepitaxial grown QDs in greater detail.
Also the optical properties of individual QDs can be further investigated on the basis of the results shown in this thesis. The ability to detect local luminescence in the STM is an unique method that can be used for the characterization of single QDs. However, in order to realize luminescence measurements, the deposition of a several nanometer thick GaAs capping layer on top of the QDs is required [186]. This capping layer passivates surface states, thus avoiding the nonradiative recombination of charge carriers. This in turn smears the lateral origin of the charge carriers and is therefore detrimental for the study of the local light emission properties of individual QDs. Additionally, the MBE growth of QDs limits the possibilities for post growth modifications, for example the density of the QDs can not be modified and more complex geometries (e. g. multilayers) can not be realized. However, this would be interesting for the investigation of for example coupling effects of QDs among each other. The use of colloidal QDs, would circumvent some of the these problems, because the fabrication of the QDs is performed in a different step than the deposition. This means, that a high flexibility is given with regard to modifications at the lateral arrangement after the growth process. One possibility would be to use the h-BN nanomesh as a template for the arrangement of small nanostructures, e. g. colloidal QDs (only a few nanometer in diameter). Because of its inertness and its stability the h-BN nanomesh is an ideal template even for QD deposition under ambient conditions. Given that the QDs arrange in the cavities of the nanomesh, various but well-defined distances (integer multiples of the periodicity of the cavities of the nanomesh) between QDs and with it a change

in the inter-QD coupling could be realized. STL and STS studies could then be used to investigate the interaction of these nanoparticles as a function of the distance of the QDs.

The second part of this thesis deals with STM, STS and scanning tunneling current induced luminescence (STL) studies performed on CdSe NWs. These NWs consist of alternating zincblende and wurtzite type lattice structures in the direction of the long axis of the NW, which lead to a variation of the bandgap in this direction. By applying a sufficiently high sample voltage it is possible to directly inject electrons and holes into the NWs which lead to local light emission. Light emission can be exclusively obtained for negative sample voltages and can be attributed to an intimate coupling of the NWs to the metallic substrate. In addition, the injection of electrons from the substrate is favored by n-type doping of the NWs which is in agreement with STS measurements. In contrast to previous studies on similar systems, the simultaneous excitation of tip induced plasmons is not necessary for the generation of light. The shape of the luminescence spectra is found to be determined by exciton-phonon coupling as well as by the spatial variation of the bandgap caused by the inhomogeneous lattice structure of alternating zincblende and wurtzite type regions. In detail, the local emission spectrum of individual NWs is found to be composed of two main peaks. One can assign the lower energy peak to emission from the intersection of zincblende and wurtzite type sections and the higher energy peak to emission from zincblende type sections. The obtained energy of the high energy STL peak of different NWs show a strong dependence on the diameter of the NW, hence, indicating quantum confinement. Furthermore, the extrapolation of the emission energies to infinite NW diameters, i. e. bulk CdSe, show that the emission originates from the zincblende type structures. This can be further supported by the observation of large optically inactive areas on the NWs by recording photon maps. This means that the STL measurements enable the identification of the crystal structure by evaluating the optical properties of the NWs.
In future experiments it would be desirable to be able to resolve the topography, i. e. lattice structure, and to directly correlate it to the observed luminescence. This was not possible for the sample investigated in this thesis, because the sample preparation was done under ambient conditions. The use of an UHV compatible preparation or protection of the sample will improve the quality of the sample which would probably allow to obtain a direct correlation between lattice structure and optical properties. One possibility would be to deposit the nanoparticles by electrospray ionization ion beam deposition under UHV and transfer the sample with a vacuum suitcase

into the STM chamber. Another possibility which probably allows to achieve atomic resolution on the NWs would be to use NWs grown in an MBE chamber with the vapor-liquid-solid method. A capping layer could protect the surface of the NWs during their transfer from the growth substrate onto a metallic substrate under ambient conditions. Prior to the STM investigations this capping layer could be removed in UHV. A possible candidate for such studies would be to use GaAs NWs grown by the vapor-liquid-solid (VLS) mechanism and to cap them with an arsenic layer after their growth. As a result one might obtain an atomically clean surface of the NWs and thus, direct information about the lattice structure. Moreover, the STS analysis would give more significant information on the lattice structure of the NWs that also can be directly related to the local electronic and optical properties. Besides improvements in the sample quality, one could also investigate effects, which can only be uncovered by investigating single nanoobjects, like emission intermittency (so called blinking). The origin of these time dependent variations of the luminescence intensity of colloidal nanostructures is not completely clear, yet [21], but might be related to surface trap states [187]. The highly local injection of charge carriers in STL and the time dependent analysis (the current experimental setup allows a time resolution of 0.5 ns) of the intensity of the consequential light emission together with the simultaneous information on the morphology would be a promising tool to gain more insight into these phenomena.

The third part of this thesis is dedicated to the investigation of the organic semiconductor $Ir(ppy)_3$ (tris-(2-phenylpyridine)iridium(III)), which shows an extremely high photoluminescent quantum yield in its bulk phase. In order to answer the question whether even single molecules are able to show fluorescence excited by a tunneling current, the molecules are deposited at submonolayer coverage onto different substrates under UHV conditions and are investigated by STM. On metal substrates no STM induced light emission is observed. The formation of small ensembles of molecules on metal substrates indicates a strong molecule-molecule interaction. The use of single layers of hexagonal boron nitride (h-BN) enables the observation of single molecules, since the cavities in this nanomesh act as potential traps. The resulting h-BN nanomesh on Rh(111) decouples the molecules from the metal surface. However, it appears that the metallic substrate is still too close and suppresses the excitation of intrinsic light emission of the molecules.
In order to obtain photon emission from single molecules in the STM, one could continue with the promising experiments presented in section 5.4. The shown preliminary results of $Ir(ppy)_3$ molecules on a multilayer of C_{60} molecules indicate increased luminescence located at the position of $Ir(ppy)_3$ molecules.

Bibliography

[1] M. Grundmann. *The Physics of Semiconductors - An Introduction Including Devices and Nanophysics*. Springer Verlag, Heidelberg, 1st edition, 2006.

[2] K. v. Klitzing, G. Dorda, and M. Pepper. New Method for High-Accuracy Determination of the Fine-Structure Constant Based on Quantized Hall Resistance. *Physical Review Letters*, 45(6):494–497, 1980.

[3] L. P. Kouwenhoven, N. C. van der Vaart, A. T. Johnson, W. Kool, C. J. P. M. Harmans, J. G. Williamson, A. A. M. Staring, and C. T. Foxon. Single Electron Charging Effects in Semiconductor Quantum Dots. *Zeitschrift für Physik B*, 85:367–373, 1991.

[4] X. Duan, Y. Huang, R. Agarwal, and C. M. Lieber. Single-Nanowire Electrically Driven Lasers. *Nature*, 421(6920):241–245, 2003.

[5] T. Steiner, editor. *Semiconductor Nanostructures for Optoelectronic Applications*. Artech House, INC. , Norwood, 1st edition, 2004.

[6] D. Loss and D. P. DiVincenzo. Quantum Computation with Quantum Dots. *Physical Review A*, 57(1):120–126, 1998.

[7] T. D. Ladd, F. Jelezko, R. Laflamme, Y. Nakamura, C. Monroe, and J. L. O'Brien. Quantum Computers. *Nature*, 464(7285):45–53, 2010.

[8] K. Balasubramanian. Challenges in the Use of 1D Nanostructures for On-Chip Biosensing and Diagnostics: A Review. *Biosensors and Bioelectronics*, 2010. in press.

[9] W. Lu and C. M. Lieber. Nanoelectronics from the Bottom up. *Nature Materials*, 6(11):841–850, 2007.

[10] R. Waser, editor. *Nanoelectronics and Information Technology*. Wiley–VCH, Weinheim, 2005.

[11] J. V. Barth, G. Costantini, and K. Kern. Engineering Atomic and Molecular Nanostructures at Surfaces. *Nature*, 437(7059):671–679, 2005.

[12] D. Bimberg, M. Grundmann, and N. N. Ledentsov. *Quantum Dot Heterostructures*. Wiley, Chichester, 1st edition, 1999.

[13] D. V. Talapin, J.-S. Lee, M. V. Kovalenko, and E. V. Shevchenko. Prospects of Colloidal Nanocrystals for Electronic and Optoelectronic Applications. *Chemical Reviews*, 110(1):389–458, 2010.

[14] J. R. Heath. Molecular Electronics. *Annual Review of Materials Research*, 39:1–23, 2009.

[15] K. Walzer, B. Maennig, M. Pfeiffer, and K. Leo. Highly Efficient Organic Devices Based on Electrically Doped Transport Layers. *Chemical Reviews*, 107(4):1233–1271, 2007.

[16] H. Klauk. Organic Thin-Film Transistors. *Chemical Society Reviews*, 39(7):2643–2666, 2010.

[17] M. Schubert. Another Century of Ellipsometry. *Annalen der Physik*, 15(7-8):480–497, 2006.

[18] T. Guo. More Power to X-Rays: New Developments in X-ray Spectroscopy. *Laser & Photonics Reviews*, 3(6):591–622, 2009.

[19] G. Renaud and R. Lazzari and F. Leroy. Probing Surface and Interface Morphology with Grazing Incidence Small Angle X-Ray Scattering. *Surface Science Reports*, 64(8):255–380, 2009.

[20] Th. Basché, W. E. Moerner, M. Orrit, and H. Talon. Photon Antibunching in the Fluorescence of a Single Dye Molecule Trapped in a Solid. *Physical Review Letters*, 69(10):1516–1519, 1992.

[21] P. Frantsuzov, M. Kuno, B. Janko, and R. A. Marcus. Universal Emission Intermittency in Quantum Dots, Nanorods and Nanowires. *Nature Physics*, 4(7):519–522, 2008.

[22] R. Wiesendanger, editor. *Scanning-Probe Microscopy*. Springer Verlag, Berlin Heidelberg, 1st edition, 1998.

[23] M. Kuno. An Overview of Solution-Based Semiconductor Nanowires: Synthesis and Optical Studies. *Physical Chemistry Chemical Physics*, 10(5):620–639, 2008.

[24] Y. Kawamura, K. Goushi, J. Brooks, J. J. Brown, H. Sasabe, and C. Adachi. 100 percent Phosphorescence Quantum Efficiency of Ir(III) Complexes in Organic Semiconductor Films. *Applied Physics Letters*, 86(7):071104, 2005.

[25] F. J. Giessibl. Advances in Atomic Force Microscopy. *Reviews of Modern Physics*, 75(3):949–983, 2003.

[26] S. N. Magonov. Surface Characterization of Materials at Ambient Conditions by Scanning Tunneling Microscopy (STM) and Atomic Force Microscopy (AFM). *Applied Spectroscopy Reviews*, 28:1–121, 1993.

[27] Q. Zhong, D. Inniss, K. Kjoller, and V.B. Elings. Fractured Polymer/Silica Fiber Surface Studied by Tapping Mode Atomic Force Microscopy. *Surface Science*, 290(1-2):L688–L692, 1993.

[28] J. A. Stroscio and W. J. Kaiser, editors. *Methods of Experimental Physics: Scanning Tunneling Microscopy*, volume 27. Academic Press, Inc., San Diego, 1st edition, 1993.

[29] J. Tersoff and D. R. Hamann. Theory and Application for the Scanning Tunneling Microscope. *Physical Review Letters*, 50(25):1998–2001, 1983.

[30] J. Tersoff and D. R. Hamann. Theory of the Scanning Tunneling Microscope. *Physical Review B*, 31(2):805–813, 1985.

[31] N. D. Lang. Spectroscopy of Single Atoms in the Scanning Tunneling Microscope. *Physical Review B*, 34(8):5947–5950, 1986.

[32] J. K. Gimzewski, B Reihl, J. H. Coombs, and R. R. Schlitter. Photon-Emission with the Scanning Tunneling Microscope. *Zeitschrift für Physik B*, 72(4):497–501, 1988.

[33] R. Berndt, J. K. Gimzewski, and P. Johansson. Inelastic Tunneling Excitation of Tip-Induced Plasmon Modes on Noble-Metal Surfaces. *Physical Review Letters*, 67(27):3796–3799, 1991.

[34] A. Downes and M. E. Welland. Photon Emission from Ag and Au Clusters in the Scanning Tunneling Microscope. *Applied Physics Letters*, 72(21):2671–2673, 1998.

[35] N. Nilius, N. Ernst, and H.-J. Freund. Photon Emission Spectroscopy of Individual Oxide-Supported Silver Clusters in a Scanning Tunneling Microscope. *Physical Review Letters*, 84(17):3994–3997, 2000.

[36] R. Berndt and J. K. Gimzewski. Injection Luminescence from CdS(1120) Studied with Scanning Tunneling Microscopy. *Physical Review B*, 45(24):14095–14099, 1992.

[37] D. L. Abraham, A. Veider, Ch. Schönenberger, H. P. Meier, D. J. Arent, and S. F. Alvarado. Nanometer Resolution in Luminescence Microscopy of III-V Heterostructures. *Applied Physics Letters*, 56(16):1564–1566, 1990.

[38] J. Lindahl, M.-E. Pistol, L. Montelius, and L. Samuelson. Stark Effect in Individual Luminescent Centers Observed by Tunneling Luminescence. *Applied Physics Letters*, 68(1):60–62, 1996.

[39] M. J. Romero, J. van de Lagemaat, I. Mora-Sero, G. Rumbles, and M. M. Al-Jassim. Imaging of Resonant Quenching of Surface Plasmons by Quantum Dots. *Nano Letters*, 6(12):2833–2837, 2006.

[40] A. J. Mäkinen, E. E. Foos, J. Wilkinson, and J. P. Long. STM-Induced Light Emission from Substrate-Tethered Quantum Dots. *The Journal of Physical Chemistry C*, 111(23):8188–8194, 2007.

[41] R. Berndt, R. Gaisch, W. D. Schneider, J. K. Gimzewski, B. Reihl, R. R. Schlittler, and M. Tschudy. Photon Emission from Adsorbed C_{60} Molecules with Sub-Nanometer Lateral Resolution. *Applied Physics A*, 57(6):513–516, 1993.

[42] R. Berndt, R. Gaisch, J. K. Gimzewski, B. Reihl, R. R. Schlitter, W. D. Schneider, and M. Tschudy. Photon-Emission at Molecular Resolution Induced by a Scanning Tunneling Microscope. *Science*, 262(5138):1425–1427, 1993.

[43] X. H. Qiu, G. V. Nazin, and W. Ho. Vibrationally Resolved Fluorescence Excited with Submolecular Precision. *Science*, 299(5606):542–546, 2003.

[44] Z.-C. Dong, X.-L. Guo, A. S. Trifonov, P. S. Dorozhkin, K. Miki, K. Kimura, S. Yokoyama, and S. Mashiko. Vibrationally Resolved Fluorescence from Organic Molecules near Metal Surfaces in a Scanning Tunneling Microscope. *Physical Review Letters*, 92(8):086801, 2004.

[45] E. Ćavar, M.-C. Blüm, M. Pivetta, F. Patthey, M. Chergui, and W.-D. Schneider. Fluorescence and Phosphorescence from Individual C_{60} Molecules Excited by Local Electron Tunneling. *Physical Review Letters*, 95(19):196102, 2005.

[46] P. Johansson, R. Monreal, and P. Apell. Theory for Light Emission from a Scanning Tunneling Microscope. *Physical Review B*, 42(14):9210–9213, 1990.

[47] G. Hoffmann, J. Aizpurua, P. Apell, and R. Berndt. Influence of Tip Geometry in Light Emission from the Scanning Tunnelling Microscope. *Surface Science*, 482-485(Part 2):1159–1162, 2001.

[48] A. Kabakchiev, K. Kuhnke, T. Lutz, and K. Kern. Electroluminescence from Individual Pentacene Nanocrystals. *ChemPhysChem*, 2010. accepted.

[49] M. J. Romero and J. van de Lagemaat. Luminescence of Quantum Dots by Coupling with Nonradiative Surface Plasmon Modes in a Scanning Tunneling Microscope. *Physical Review B*, 80(11):115432, 2009.

[50] Ph. Renaud and S. F. Alvarado. Mapping Quantum-Well Energy Profiles of III-V Heterostructures by Scanning-Tunneling-Microscope-Excited Luminescence. *Physical Review B*, 44(12):6340–6343, 1991.

[51] T. Tsuruoka, Y. Ohizumi, R. Tanimoto, and S. Ushioda. Light Emission Spectra of Individual GaAs Quantum Wells Induced by Scanning Tunneling Microscope. *Applied Physics Letters*, 75(15):2289–2291, 1999.

[52] M. Pfister, M. B. Johnson, S. F. Alvarado, H. W. M. Salemink, U. Marti, D. Martin, F. Morier-Genoud, and F. K. Reinhart. Atomic Structure and Luminescence Excitation of GaAs/$(AlAs)_n(GaAs)_m$ Quantum Wires with the Scanning Tunneling Microscope. *Applied Physics Letters*, 65(9):1168–1170, 1994.

[53] S. E. J. Jacobs, M. Kemerink, P. M. Koenraad, M. Hopkinson, H. W. M. Salemink, and J. H. Wolter. Spatially Resolved Scanning Tunneling Luminescence on Self-Assembled InGaAs/GaAs Quantum Dots. *Applied Physics Letters*, 83(2):290–292, 2003.

[54] U. Håkanson, H. Håkanson, M. K.-J. Johansson, L. Samuelson, and M.-E. Pistol. Electric Field Effects in Single Semiconductor Quantum Dots Observed by Scanning Tunneling Luminescence. *Journal of Vacuum Science and Technology B*, 21(6):2344–2347, 2003.

[55] T. Tsuruoka, Y. Ohizumi, and S. Ushioda. Ground-state Interband Transition of Individual Self-Assembled InAs/$Al_{0.6}Ga_{0.4}As$ Quantum Dots Observed by Scanning-Tunneling-Microscope Light-Emission Spectroscopy. *Journal of Applied Physics*, 95(3):1064–1073, 2004.

[56] S. F. Alvarado, Ph. Renaud, D. L. Abraham, Ch. Schönenberger, D. J. Arent, and H. P. Meier. Luminescence in Scanning Tunneling Microscopy on III–V Nanostructures. *Journal of Vacuum Science and Technology B*, 9(2):409–413, 1991.

[57] S. H. Pan, E. W. Hudson, and J. C. Davis. ^{3}He Refrigerator Based very Low Temperature Scanning Tunneling Microscope. *Review of Scientific Instruments*, 70(2):1459–1463, 1999.

[58] A. Kabakchiev. *Luminescence of Organic Molecules Studied by Scanning Tunneling Microscopy*. PhD thesis, EPF Lausanne, 2010.

[59] K. Kuhnke, A. Kabakchiev, W. Stiepany, F. Zinser, R. Vogelgesang, and K. Kern. Versatile Optical Access to the Tunnel Gap in a Low-Temperature STM. *Review of Scientific Instruments*, 2010. accepted.

[60] B. Ren, G. Picardi, and B. Pettinger. Preparation of Gold Tips Suitable for Tip-Enhanced Raman Spectroscopy and Light Emission by Electrochemical Etching. *Review of Scientific Instruments*, 75(4):837–841, 2004.

[61] V. G. Bordo and H.-G. Rubahn. *Optics and Spectroscopy at Surfaces and Interfaces*. Wiley-VCH, Weinheim. 1st edition, 2005.

[62] J. Stangl, V. Holý, and G. Bauer. Structural Properties of Self-Organized Semiconductor Nanostructures. *Reviews of Modern Physics*, 76(3):725–783, 2004.

[63] D. Leonard, K. Pond, and P. M. Petroff. Critical Layer Thickness for Self-Assembled InAs Islands on GaAs. *Physical Review B*, 50(16):11687–11692, 1994.

[64] I. Mukhametzhanov, Z. Wei, R. Heitz, and A. Madhukar. Punctuated Island Growth: An Approach to Examination and Control of Quantum Dot Density, Size, and Shape Evolution. *Applied Physics Letters*, 75(1):85–87, 1999.

[65] P. Kratzer, Q. K. K. Liu, P. Acosta-Diaz, C. Manzano, G. Costantini, R. Songmuang, A. Rastelli, O. G. Schmidt, and K. Kern. Shape Transition during Epitaxial Growth of InAs Quantum Dots on GaAs(001): Theory and Experiment. *Physical Review B*, 73(20):205347, 2006.

[66] M. C. Xu, Y. Temko, T. Suzuki, and K. Jacobi. Shape Transition of InAs Quantum Dots on GaAs(001). *Journal of Applied Physics*, 98(8):083525, 2005.

[67] F. Patella, S. Nufris, F. Arciprete, M. Fanfoni, E. Placidi, A. Sgarlata, and A. Balzarotti. Tracing the Two- to Three-Dimensional Transition in the InAs/GaAs(001) Heteroepitaxial Growth. *Physical Review B*, 67(20):205308, 2003.

[68] J. Márquez, L. Geelhaar, and K. Jacobi. Atomically Resolved Structure of InAs Quantum Dots. *Applied Physics Letters*, 78(16):2309–2311, 2001.

[69] G. Costantini, A. Rastelli, C. Manzano, R. Songmuang, O. G. Schmidt, K. Kern, and H. von Känel. Universal Shapes of Self-Organized Semiconductor Quantum Dots: Striking Similarities between InAs/GaAs(001) and Ge/Si(001). *Applied Physics Letters*, 85(23):5673–5675, 2004.

[70] J. Tersoff and F. K. LeGoues. Competing Relaxation Mechanisms in Strained Layers. *Physical Review Letters*, 72(22):3570–3573, 1994.

[71] H. T. Dobbs, D. D. Vvedensky, A. Zangwill, J. Johansson, N. Carlsson, and W. Seifert. Mean-Field Theory of Quantum Dot Formation. *Physical Review Letters*, 79(5):897–900, 1997.

[72] Y. Chen and J. Washburn. Structural Transition in Large-Lattice-Mismatch Heteroepitaxy. *Physical Review Letters*, 77(19):4046–4049, 1996.

[73] G. Costantini, C. Manzano, R. Songmuang, O. G. Schmidt, and K. Kern. InAs/GaAs(001) Quantum Dots Close to Thermodynamic Equilibrium. *Applied Physics Letters*, 82(19):3194–3196, 2003.

[74] M. A. Herman and H. Sitter. *Molecular Beam Epitaxy - Fundamentals and Current Status*, volume 7. Springer, Berlin, 1996.

[75] H. Lüth. *Solid Surfaces, Interfaces and Thin Films*. Springer-Verlag, Heidelberg, 3rd edition, 2001.

[76] V. P. LaBella, M. R. Krause, Z. Ding, and P. M. Thibado. Arsenic-Rich GaAs(001) Surface Structure. *Surface Science Reports*, 60(1-4):1–53, 2005.

[77] J. Zhang, O. P. Naji, P. Steans, P. Tejedor, T. Kaneko, T. S. Jones, and B. A. Joyce. Modulated-Beam Studies of the Layer-by-Layer Etching of GaAs(001) Using $AsBr_3$: Identification of the Reaction Mechanism. *Journal of Crystal Growth*, 175(2):1284–1288, 1997.

[78] M. Ritz, T. Kaneko, and K. Eberl. The Effect of Surface Reconstructions on the Surface Morphology During in Situ Etching of GaAs. *Applied Physics Letters*, 71(5):695–697, 1997.

[79] H. Schuler, T. Kaneko, M. Lipinski, and K. Eberl. In situ Etching with $AsBr_3$ and Regrowth in Molecular Beam Epitaxy. *Semiconductor Science and Technology*, 15(2):169, 2000.

[80] N. Esser, W. G. Schmidt, C. Cobet, K. Fleischer, A. I. Shkrebtii, B. O. Fimland, and W. Richter. Atomic Structure and Optical Anisotropy of III–V(001) Surfaces. *Journal of Vacuum Science & Technology B*, 19(5):1756–1761, 2001.

[81] H. Röder, E. Hahn, H. Brune, J.-P. Bucher, and K. Kern. Building One- and Two-Dimensional Nanostructures via Diffusion Controlled Aggregation at Surfaces. *Nature*, 366(6451):141–143, 1993.

[82] J. V. Barth, J. Weckesser, C. Z. Cai, P. Günter, L. Bürgi, O. Jeandupeux, and K. Kern. Building Supramolecular Nanostructures at Surfaces by Hydrogen Bonding. *Angewandte Chemie*, 39(7):1230–1234, 2000.

[83] E. Bauer and J. H. van der Merwe. Structure and Growth of Crystalline Superlattices: From Monolayer to Superlattice. *Physical Review B*, 33(6):3657–3671, 1986.

[84] P. Hartman, W. Bardsley, D. T. J. Hurle, and J. B. Mullin, editors. *Crystal Growth: An Introduction*. North-Holland Publishing Company, Amsterdam, 1st edition, 1973.

[85] N. Moll, M. Scheffler, and E. Pehlke. Influence of Surface Stress on the Equilibrium Shape of Strained Quantum Dots. *Physical Review B*, 58(8):4566–4571, 1998.

[86] O. Madelung, U. Rössler, and M. Schulz, editors. *Gallium Arsenide (GaAs), Direct Energy Gap (Part of Landolt-Börnstein - Group III Condensed Matter Numerical Data and Functional Relationships in Science and Technology)*, volume 41A1b. SpringerMaterials, 1993.

[87] A. R. Avery, D. M. Homes, J. Sudijono, T. S. Jones, and B. A. Joyce. The As-Terminated Reconstructions Formed by GaAs(001): A Scanning Tunnelling Microscopy Study of the (2×4) and c(4×4) Surfaces. *Surface Science*, 323(1-2):91–101, 1995.

[88] L. Däweritz and R. Hey. Reconstruction and Defect Structure of Vicinal GaAs(001) and $Al_xGa_{1-x}As(001)$ Surfaces during MBE Growth. *Surface Science*, 236(1-2):15–22, 1990.

[89] J. G. Belk, C. F. McConville, J. L. Sudijono, T. S. Jones, and B. A. Joyce. Surface Alloying at InAs–GaAs Interfaces Grown on (001) Surfaces by Molecular Beam Epitaxy. *Surface Science*, 387(1-3):213–226, 1997.

[90] P. Kratzer, E. Penev, and M. Scheffler. Understanding the Growth Mechanisms of GaAs and InGaAs Thin Films by Employing First-Principles Calculations. *Applied Surface Science*, 216(1-4):436–446, 2003.

[91] S. Tsukamoto, T. Honma, G. R. Bell, A. Ishii, and Y. Arakawa. Atomistic Insights for InAs Quantum Dot Formation on GaAs(001) using STM within a MBE Growth Chamber. *Small*, 2(3):386–389, 2006.

[92] C. Priester and M. Lannoo. Origin of Self-Assembled Quantum Dots in Highly Mismatched Heteroepitaxy. *Physical Review Letters*, 75(1):93–96, 1995.

[93] H. Saito, K. Nishi, and S. Sugou. Shape Transition of InAs Quantum Dots by Growth at High Temperature. *Applied Physics Letters*, 74(9):1224–1226, 1999.

[94] A. Rastelli and H. von Känel. Surface Evolution of Faceted Islands. *Surface Science*, 515(2-3):L493–L498, 2002.

[95] M. A. Lutz, R. M. Feenstra, P. M. Mooney, J. Tersoff, and J. O. Chu. Facet Formation in Strained Si_{1-x} Ge_x films. *Surface Science*, 316(3):L1075–L1080, 1994.

[96] B. T. Miller, W. Hansen, S. Manus, R. J. Luyken, A. Lorke, J. P. Kotthaus, S. Huant, G. Medeiros-Ribeiro, and P. M. Petroff. Few-Electron Ground States of Charge-Tunable Self-Assembled Quantum Dots. *Physical Review B*, 56(11):6764–6769, 1997.

[97] L. R. C. Fonseca, J. L. Jimenez, J. P. Leburton, and Richard M. Martin. Self-Consistent Calculation of the Electronic Structure and Electron-Electron Interaction in Self-Assembled InAs-GaAs Quantum Dot Structures. *Physical Review B*, 57(7):4017–4026, 1998.

[98] O. Stier, M. Grundmann, and D. Bimberg. Electronic and Optical Properties of Strained Quantum Dots Modeled by 8-Band k · p Theory. *Physical Review B*, 59(8):5688–5701, 1999.

[99] B. Grandidier, Y. M. Niquet, B. Legrand, J. P. Nys, C. Priester, D. Stiévenard, J. M. Gérard, and V. Thierry-Mieg. Imaging the Wave-Function Amplitudes in Cleaved Semiconductor Quantum Boxes. *Physical Review Letters*, 85(5):1068–1071, 2000.

[100] T. Maltezopoulos, A. Bolz, C. Meyer, C. Heyn, W. Hansen, M. Morgenstern, and R. Wiesendanger. Wave-Function Mapping of InAs Quantum Dots by Scanning Tunneling Spectroscopy. *Physical Review Letters*, 91(19):196804, 2003.

[101] A. Urbieta, B. Grandidier, J. P. Nys, D. Deresmes, D. Stiévenard, A. Lemaître, G. Patriarche, and Y. M. Niquet. Scanning Tunneling Spectroscopy of Cleaved InAs/GaAs Quantum Dots at Low Temperatures. *Physical Review B*, 77(15):155313, 2008.

[102] J. C. Girard, A. Lemaître, A. Miard, C. David, and Z. Z. Wang. Low Temperature Scanning Tunneling Microscopy Wave-Function Imaging of InAs/GaAs Cleaved Quantum Dots with Similar Height. *Journal of Vacuum Science and Technology B*, 27(2):891–894, 2009.

[103] O. Madelung, U. Rössler, and M. Schulz, editors. *Indium Arsenide (InAs), Energy Gap, Exciton Data (Part of Landolt-Börnstein - Group III Condensed Matter Numerical Data and Functional Relationships in Science and Technology)*, volume 41A1b. SpringerMaterials, 1993.

[104] R. M. Feenstra. Tunneling Spectroscopy of the (110) Surface of Direct-Gap III-V Semiconductors. *Physical Review B*, 50(7):4561–4570, 1994.

[105] P. B. Joyce, T. J. Krzyzewski, G. R. Bell, B. A. Joyce, and T. S. Jones. Composition of InAs Quantum Dots on GaAs(001): Direct Evidence for (In,Ga)As Alloying. *Physical Review B*, 58(24):R15981–R15984, 1998.

[106] M. A. Migliorato, A. G. Cullis, M. Fearn, and J. H. Jefferson. Atomistic Simulation of Strain Relaxation in $In_xGa_{1-x}As$/GaAs Quantum Dots with Nonuniform Composition. *Physical Review B*, 65(11):115316, 2002.

[107] A. Lemaître, G. Patriarche, and F. Glas. Composition Profiling of InAs/GaAs Quantum Dots. *Applied Physics Letters*, 85(17):3717–3719, 2004.

[108] V. D. Dasika, R. S. Goldman, J. D. Song, W. J. Choi, N. K. Cho, and J. I. Lee. Nanometer-scale Measurements of Electronic States in InAs/GaAs Quantum Dots. *Journal of Applied Physics*, 106(1), 2009.

[109] A. Rastelli, M. Stoffel, J. Tersoff, G. S. Kar, and O. G. Schmidt. Kinetic Evolution and Equilibrium Morphology of Strained Islands. *Physical Review Letters*, 95(2):026103, 2005.

[110] H. Lee, R. R. Lowe-Webb, W. Yang, and P. C. Sercel. Formation of InAs/GaAs Quantum Dots by Molecular Beam Epitaxy: Reversibility of the Islanding Transition. *Applied Physics Letters*, 71(16):2325–2327, 1997.

[111] H. Schuler, N. Y. Jin-Phillipp, F. Phillipp, and K. Eberl. Size Modification of Self-Assembled InAs Quantum Dots by in situ Etching. *Semiconductor Science and Technology*, 13(11):1341, 1998.

[112] A. Rastelli, S. Stufler, A. Schliwa, R. Songmuang, C. Manzano, G. Costantini, K. Kern, A. Zrenner, D. Bimberg, and O. G. Schmidt. Hierarchical Self-Assembly of GaAs/AlGaAs Quantum Dots. *Physical Review Letters*, 92(16):166104, 2004.

[113] A. Rastelli and H. v. Känel. Island Formation and Faceting in the SiGe/Si(001) System. *Surface Science*, 532-535:769–773, 2003.

[114] S. O. Cho, Zh. M. Wang, and G. J. Salamo. Evolution of Elongated (In,Ga)As–GaAs(100) Islands with Low Indium Content. *Applied Physics Letters*, 86(11):113106, 2005.

[115] C. T. Foxon and B. A. Joyce. Surface Processes Controlling the Growth of $Ga_xIn_{1-x}As$ and $Ga_xIn_{1-x}P$ Alloy Films by MBE. *Journal of Crystal Growth*, 44(1):75–83, 1978.

[116] S. Kiravittaya, Y. Nakamura, and O. G. Schmidt. Photoluminescence Linewidth Narrowing of InAs/GaAs Self-Assembled Quantum Dots. *Physica E*, 13(2-4):224–228, 2002.

[117] T. Kaizu, M. Takahasi, K. Yamaguchi, and J. Mizuki. Modification of InAs Quantum Dot Structure during Annealing. *Journal of Crystal Growth*, 301-302:248–251, 2007.

[118] L. G. Wang, P. Kratzer, M. Scheffler, and Q. K. K. Liu. Island Dissolution during Capping Layer Growth Interruption. *Applied Physics A*, 73(2):161–165, 2001.

[119] J. M. García, G. Medeiros-Ribeiro, K. Schmidt, T. Ngo, J. L. Feng, A. Lorke, J. Kotthaus, and P. M. Petroff. Intermixing and Shape Changes during the Formation of InAs Self-Assembled Quantum Dots. *Applied Physics Letters*, 71(14):2014–2016, 1997.

[120] L. Wang, A. Rastelli, and O. G. Schmidt. Structural and Optical Properties of In(Ga)As/GaAs Quantum Dots Treated by Partial Capping and Annealing. *Journal of Applied Physics*, 100(6):064313, 2006.

[121] G. Costantini, A. Rastelli, C. Manzano, P. Acosta-Diaz, R. Songmuang, G. Katsaros, O. G. Schmidt, and K. Kern. Interplay between Thermodynamics and Kinetics in the Capping of $InAs/GaAs$(001) Quantum Dots. *Physical Review Letters*, 96(22):226106, 2006.

[122] P. D. Cozzoli, T. Pellegrino, and L. Manna. Synthesis, Properties and Perspectives of Hybrid Nanocrystal Structures. *Chemical Society Reviews*, 35(11):1195–1208, 2006.

[123] X. F. Duan, Y. Huang, Y. Cui, J. F. Wang, and C. M. Lieber. Indium Phosphide Nanowires as Building Blocks for Nanoscale Electronic and Optoelectronic Devices. *Nature*, 409(6816):66–69, 2001.

[124] C. B. Murray, D. J. Norris, and M. G. Bawendi. Synthesis and Characterization of Nearly Monodisperse CDE (E = S, SE, TE) Semiconductor Nanocrystallites. *Journal of the American Chemical Society*, 115(19):8706–8715, 1993.

[125] H. Yu, J. Li, R. A. Loomis, P. C. Gibbons, L.-W. Wang, and W. E. Buhro. Cadmium Selenide Quantum Wires and the Transition from 3D to 2D Confinement. *Journal of the American Chemical Society*, 125(52):16168–16169, 2003.

[126] J. W. Grebinski, K. L. Hull, J. Zhang, T. H. Kosel, and M. Kuno. Solution-Based Straight and Branched CdSe Nanowires. *Chemistry of Materials*, 16(25):5260–5272, 2004.

[127] L. Manna, E. C. Scher, and A. P. Alivisatos. Synthesis of Soluble and Processable Rod-, Arrow-, Teardrop-, and Tetrapod-Shaped CdSe Nanocrystals. *Journal of the American Chemical Society*, 122(51):12700–12706, 2000.

[128] T. J. Trentler, K. M. Hickman, S. C. Goel, A. M. Viano, P. C. Gibbons, and W. E. Buhro. Solution-Liquid-Solid Growth of Crystalline III-V Semiconductors - an Analogy to Vapor-Liquid-Solid Growth. *Science*, 270(5243):1791–1794, 1995.

[129] R. S. Wagner and W. C. Ellis. Vapor-Liquid-Solid Mechanism of Single Crystal Growth. *Applied Physics Letters*, 4(5):89–90, 1964.

[130] F. Wang, A. Dong, J. Sun, R. Tang, H. Yu, and W. E. Buhro. Solution-Liquid-Solid Growth of Semiconductor Nanowires. *Inorganic Chemistry*, 45(19):7511–7521, 2006.

[131] Z. Li, A. Kornowski, A. Myalitsin, and A. Mews. Formation and Function of Bismuth Nanocatalysts for the Solution-Liquid-Solid Synthesis of CdSe Nanowires. *Small*, 4(10):1698–1702, 2008.

[132] O. Kurtulus, Z. Li, A. Mews, and U. Pietsch. X-ray Investigation of CdSe Nanowires. *Physica Status Solidi A*, 206(8, Sp. Iss. SI):1752–1756, 2009.

[133] V. V. Protasenko, K. L. Hull, and M. Kuno. Disorder-Induced Optical Heterogeneity in Single CdSe Nanowires. *Advanced Materials*, 17(24):2942, 2005.

[134] S. Adachi. *Handbook on Physical Properties of Semiconductors: II-VI Compound Semiconductors*, volume 3. Kluwer Academic Publishers, Dordrecht, 1st edition, 2004.

[135] H. Hasegawa and N. Negoro and S. Kasai and Y. Ishikawa and H. Fujikuwa. Effects of Gap States on Scanning Tunneling Spectra Observed on (110)- and (001)-Oriented Clean Surfaces and Ultrathin Si Layer Covered Surfaces of GaAs Prepared by Molecular Beam Epitaxy. *Journal of Vacuum Science and Technology B* , 18(4):2100–2108, 2000.

[136] V. Snejdar and J. Jerhot. Influence of Substrate Temperature on Basic Electrical Properties of CdSe Thin Films. *Thin Solid Films*, 11(2):289–298, 1972.

[137] A. Kurokawa and J. Muto. Properties of μm-Thick CdSe Prepared by Vacuum Deposition. *Journal of Materials Science*, 14:33–35, 2003.

[138] N. G. Dhere, N. R. Parikh, and A. Ferreira. The Structure and Semiconducting Properties of Cadmium Selenide Films. *Thin Solid Films*, 44(1):83–91, 1977.

[139] Y.-J. Doh, K. N. Maher, L. Ouyang, Chun L. Yu, H. Park, and J. Park. Electrically Driven Light Emission from Individual CdSe Nanowires. *Nano Letters*, 8(12):4552–4556, 2008.

[140] H.-J. Choi, J.-K. Yang, and H.-H. Park. Effect of Surface Capping Molecules on the Electronic Structure of CdSe Nanocrystal Film. *Thin Solid Films*, 494(1-2):207–210, 2006.

[141] R. Berndt and J. K. Gimzewski. The Role of Proximity Plasmon Modes on Noble Metal Surfaces in Scanning Tunneling Microscopy. *Surface Science*, 270(Part A):556–559, 1992.

[142] M. S. Gudiksen, K. N. Maher, L. Ouyang, and H. Park. Electroluminescence from a Single-Nanocrystal Transistor. *Nano Letters*, 5(11):2257–2261, 2005.

[143] H. Lange, M. Machon, M. Artemyev, U. Woggon, and C. Thomsen. Effect of ZnS Shell on the Raman Spectra from CdSe Nanorods. *Physica Status Solidi*, 1(6):274–276, 2007.

[144] F. Comas, N. Studart, and G. E. Marques. Optical Phonons in Semiconductor Quantum Rods. *Solid State Communications*, 130(7):477–480, 2004.

[145] F. Wang, H. Yu, S. Jeong, J. M. Pietryga, J. A. Hollingsworth, P. C. Gibbons, and W. E. Buhro. The Scaling of the Effective Band Gaps in Indium-Arsenide Quantum Dots and Wires. *ACS Nano*, 2(9):1903–1913, 2008.

[146] S. Alvarado, P. Renaud, and H. Meier. High Resolution Electron Beam Injection in Semiconductors Using a Scanning Tunneling Microscope. *Journal de Physique IV*, 1:271, 1991.

[147] H. Yu, J. B. Li, R. A. Loomis, L. W. Wang, and W. E. Buhro. Two- versus Three-Dimensional Quantum Confinement in Indium Phosphide Wires and Dots. *Nature Materials*, 2(8):517–520, 2003.

[148] R. Berndt, J. K. Gimzewski, and P. Johansson. Electromagnetic Interactions of Metallic Objects in Nanometer Proximity. *Physical Review Letters*, 71(21):3493–3496, 1993.

[149] P. Johansson. Light Emission from a Scanning Tunneling Microscope: Fully Retarded Calculation. *Physical Review B*, 58(16):10823–10834, 1998.

[150] D.G. Walmsley and T.-S. Tan and P. Dawson. Light Emission from Gold and Silver Thin Films in a Scanning Tunneling Microscope: Role of Contamination and Interpretation of Grain Structure in Photon Maps. *Surface Science*, 572(2-3):497–520, 2004.

[151] J. Wang, M. S. Gudiksen, X. Duan, Y. Cui, and C. M. Lieber. Highly Polarized Photoluminescence and Photodetection from Single Indium Phosphide Nanowires. *Science*, 293(5534):1455–1457, 2001.

[152] M. Wenderoth, M. J. Gregor, and R. G. Ulbrich. Luminescence from Gold-Passivated Gallium Arsenide Surfaces Excited with a Scanning Tunneling Microscope. *Solid State Communications*, 83(8):535–537, 1992.

[153] L. Zhang, J.-W. Luo, A. Zunger, N. Akopian, V. Zwiller, and J.-C. Harmand. Wide InP Nanowires with Wurtzite/Zincblende Superlattice Segments are Type-II whereas Narrower Nanowires Become Type-I: An Atomistic Pseudopotential Calculation. *Nano Letters*, 10(10):4055–4060, 2010.

[154] R. Zhou, H.-C. Chang, V. Protasenko, M. Kuno, A. K. Singh, D. Jena, and H. Xing. CdSe Nanowires with Illumination-Enhanced Conductivity: Induced Dipoles, Dielectrophoretic Assembly, and Field-Sensitive Emission. *Journal of Applied Physics*, 101(7):073704, 2007.

[155] L.-S. Li and A. P. Alivisatos. Origin and Scaling of the Permanent Dipole Moment in CdSe Nanorods. *Physical Review Letters*, 90(9):097402, 2003.

[156] T. Nann and J. Schneider. Origin of Permanent Electric Dipole Moments in Wurtzite Nanocrystals. *Chemical Physics Letters*, 384(1-3):150–152, 2004.

[157] L. M. Smith, H. E. Jackson, J. M. Yarrison-Rice, and C. Jagadish. Insights into Single Semiconductor Nanowire Heterostructures Using Time-Resolved Photoluminescence. *Semiconductor Science and Technology*, 25(2):024010, 2010.

[158] Y. M. Sun, Y. Q. Liu, and D. B. Zhu. Advances in Organic Field-Effect Transistors. *Journal of Materials Chemistry*, 15(1):53–65, 2005.

[159] U. Mitschke and P. Bäuerle. The Electroluminescence of Organic Materials. *Journal of Materials Chemistry*, 10:1471–1507, 2000.

[160] H. Aziz, Z. D. Popovic, N. X. Hu, A. M. Hor, and G. Xu. Degradation Mechanism of Small Molecule-Based Organic Light-Emitting Devices. *Science*, 283(5409):1900–1902, 1999.

[161] A. K. Ekert, J. G. Rarity, P. R. Tapster, and G. Massimo P. Practical Quantum Cryptography Based on Two-Photon Interferometry. *Physical Review Letters*, 69(9):1293–1295, 1992.

[162] C. Brunel, B. Lounis, P. Tamarat, and M. Orrit. Triggered Source of Single Photons based on Controlled Single Molecule Fluorescence. *Physical Review Letters*, 83(14):2722–2725, 1999.

[163] K. A. King, P. J. Spellane, and Richard J. Watts. Excited-State Properties of a Triply Ortho-Metalated Iridium(III) Complex. *Journal of the American Chemical Society*, 107(5):1431–1432, 1985.

[164] A. B. Tamayo, B. D. Alleyne, P. I. Djurovich, S. Lamansky, I. Tsyba, N. N. Ho, R. Bau, and M. E. Thompson. Synthesis and Characterization of Facial and Meridional Tris-Cyclometalated Iridium(III) Complexes. *Journal of the American Chemical Society*, 125(24):7377–7387, 2003.

[165] J. Breu, P. Stssel, S. Schrader, A. Starukhin, W. J. Finkenzeller, and H. Yersin. Crystal Structure of fac-Ir(ppy)$_3$ and Emission Properties under Ambient Conditions and at High Pressure. *Chemistry of Materials*, 17(7):1745–1752, 2005.

[166] T. Yokoyama, T. Takahashi, K. Shinozaki, and M. Okamoto. Quantitative Analysis of Long-Range Interactions between Adsorbed Dipolar Molecules on Cu(111). *Physical Review Letters*, 98(20):206102, 2007.

[167] M. Corso, W. Auwärter, M. Muntwiler, A. Tamai, T. Greber, and J. Osterwalder. Boron Nitride Nanomesh. *Science*, 303(5655):217–220, 2004.

[168] M. Karas and F. Hillenkamp. Laser Desorption Ionization of Proteins with Molecular Masses Exceeding 10,000 Daltons. *Analytical Chemistry*, 60(20):2299–2301, 1988.

[169] K. Kuhnke, R. Becker, M. Epple, and K. Kern. C_{60} Exciton Quenching near Metal Surfaces. *Physical Review Letters*, 79(17):3246–3249, 1997.

[170] M. Böhringer, K. Morgenstern, W.-D. Schneider, R. Berndt, F. Mauri, A. De Vita, and R. Car. Two-Dimensional Self-Assembly of

Supramolecular Clusters and Chains. *Physical Review Letters*, 83(2):324–327, 1999.

[171] C. F. Macrae, I. J. Bruno, J. A. Chisholm, P. R. Edgington, P. McCabe, E. Pidcock, L. Rodriguez-Monge, R. Taylor, J. van de Streek, and P. A. Wood. Mercury CSD 2.0 - New Features for the Visualization and Investigation of Crystal Structures. *Journal of Applied Crystallography*, 41(Part 2):466–470, 2008.

[172] H. Gersen, R. Schaub, W. Xu, I. Stensgaard, E. Laegsgaard, T. R. Linderoth, F. Besenbacher, Md. K. Nazeeruddin, and M. Graetzel. Dissociation of Iridium(III) Phosphorescent Emitters upon Adsorption on Cu(110) Revealed by Scanning Tunneling Microscopy. *Applied Physics Letters*, 89(26):264102, 2006.

[173] W. Chen, V. Madhavan, T. Jamneala, and M. F. Crommie. Scanning Tunneling Microscopy Observation of an Electronic Superlattice at the Surface of Clean Gold. *Physical Review Letters*, 80(7):1469–1472, 1998.

[174] S.-C. Lo, C. P. Shipley, R. N. Bera, R. E. Harding, A. R. Cowley, P. L. Burn, and I. D. W. Samuel. Blue Phosphorescence from Iridium(III) Complexes at Room Temperature. *Chemistry of Materials*, 18(21):5119–5129, 2006.

[175] Z. C. Dong, A. Kar, P. Dorozhkin, K. Amemiya, T. Uchihashi, S. Yokoyama, T. Kamikado, S. Mashiko, and T. Okamoto. Tunneling Electron Induced Luminescence from Monolayered Cu-TBP Porphyrin Molecules Adsorbed on Cu(100). *Thin Solid Films*, 438-439:262–267, 2003.

[176] J. Repp, G. Meyer, S. M. Stojković, A. Gourdon, and C. Joachim. Molecules on Insulating Films: Scanning-Tunneling Microscopy Imaging of Individual Molecular Orbitals. *Physical Review Letters*, 94(2):026803, 2005.

[177] R. Otero, Y. Naitoh, F. Rosei, P. Jiang, P. Thostrup, A. Gourdon, E. Laegsgaard, I. Stensgaard, C. Joachim, and F. Besenbacher. One-Dimensional Assembly and Selective Orientation of Lander Molecules on an O-Cu Template. *Angewandte Chemie*, 43(16):2092–2095, 2004.

[178] L. Ramoino, M. von Arx, S. Schintke, A. Baratoff, H. J. Güntherodt, and T. A. Jung. Layer-Selective Epitaxial Self-Assembly of Porphyrins on Ultrathin Insulators. *Chemical Physics Letters*, 417(1-3):22–27, 2006.

[179] S. Berner, M. Corso, R. Widmer, O. Groening, R. Laskowski, P. Blaha, K. Schwarz, A. Goriachko, H. Over, S. Gsell, M. Schreck, H. Sachdev, T. Greber, and J. Osterwalder. Boron Nitride Nanomesh: Functionality from a Corrugated Monolayer. *Angewandte Chemie*, 46(27):5115–5119, 2007.

[180] C. H. Michaelis. *Local Electronic Properties of Individual Nanostructures on the Boron Nitride Nanomesh.* PhD thesis, Universität Konstanz, 2010.

[181] O. Bunk, M. Corso, D. Martoccia, R. Herger, P.R. Willmott, B.D. Patterson, J. Osterwalder, J.F. van der Veen, and T. Greber. Surface X-ray Diffraction Study of Boron-Nitride Nanomesh in Air. *Surface Science*, 601(2):L7–L10, 2007.

[182] R. Laskowski, P. Blaha, and K. Schwarz. Bonding of Hexagonal BN to Transition Metal Surfaces: An Ab Initio Density-Functional Theory Study. *Physical Review B*, 78(4):045409, 2008.

[183] H. Dil, J. Lobo-Checa, R. Laskowski, P. Blaha, S. Berner, J. Osterwalder, and T. Greber. Surface Trapping of Atoms and Molecules with Dipole Rings. *Science*, 319(5871):1824–1826, 2008.

[184] M. Gsell, P. Jakob, and D. Menzel. Effect of Substrate Strain on Adsorption. *Science*, 280(5364):717–720, 1998.

[185] A. Goriachko, Y. He, M. Knapp, H. Over, M. Corso, T. Brugger, S. Berner, J. Osterwalder, and T. Greber. Self-Assembly of a Hexagonal Boron Nitride Nanomesh on Ru(0001). *Langmuir*, 23(6):2928–2931, 2007.

[186] K. Yamanaka, K. Suzuki, S. Ishida, and Y. Arakawa. Light Emission from Individual Self-Assembled InAs/GaAs Quantum Dots Excited by Tunneling Current Injection. *Applied Physics Letters*, 73(11):1460–1462, 1998.

[187] J. J. Glennon, R. Tang, W. E. Buhro, and R. A. Loomis. Synchronous Photoluminescence Intermittency (Blinking) along Whole Semiconductor Quantum Wires. *Nano Letters*, 7(11):3290–3295, 2007.

Acknowledgement

I would like to thank Prof. Klaus Kern for giving me the opportunity to work on this exciting topic and for his support throughout the time.
My gratitude goes to Prof. Robert Schaller, Prof. Anna Fontcuberta i Morral, Prof. Alf Mews and Prof. Markus Morgenstern for being members in my PhD jury.
I am very grateful to my supervisor Prof. Giovanni Costantini for his helpfulness during the first time of my PhD, before he left to the UK, and also for his continuous support in the following. I also want to thank Dr. Klaus Kuhnke for his support and assistance. My gratitude goes to Dr. Uta Schlickum for always being available for help, for the good working atmosphere as well as for the correction of this thesis. I also want to thank Dr. Marko Burghard for his encouragements and a lot of useful discussions concerning the CdSe nanowire project.
I would especially like to thank Dr. Alexander Kabakchiev for the good working atmosphere and the good teamwork at the Photon-STM. Dr. Takayuki Suzuki I want to thank for his support and the good cooperation concerning the quantum dot project. I would also like to acknowledge Thomas Dufaux for his assistance in the preparation of the nanowire samples and Dr. Stephan Rauschenbach for the MALDI measurements. My thank goes to Christian Wolpert and Armin Schulz who performed the photoluminescence and the Raman measurements, respectively.
I would like to thank the people from the MBE group for their continuous support and advice: Prof. Oliver G. Schmidt, Dr. Armando Rastelli, Dr. Suwit Kiravittaya, Dr. Lijuan Wang and Wolfgang Winter. I want to thank Prof. Alf Mews and Zhe Wang for the cooperation and the synthesis of the CdSe nanowires.
I am also grateful to our technicians Wolfgang Stiepany, Peter Andler, Andreas Koch, Martin Siemers and Rafail Chaikevitch for all their help concerning technical questions. I want to thank Sabine Birtel for uncomplicated support with paperwork.
I would especially like to acknowledge all my colleagues in Stuttgart for the

nice and friendly atmosphere in our group. In particular, the people in our office: Nasiba Abdurakhmanova, Jakob Bork, Christopher Kley, Alexander Langner, Dietmar Payer, Gordon Rinke. Our lunch table: Jan Cechal, Tim Koppenrath, Adarsh Sagar, Sebastian Stepanow and Tzu-Chun Tseng. And: Max Assig, Jens Dormüller, Isabella Gierz, Tobias Herden, Steffen Kahle, Sören Krotzky, Christian Michaelis, Robin Ohmann, Hyeyeon Ryu, Violetta Sessi, Carola Straßer, Ulrich Stützel and Charlène Tonnoir.
Finally, I would like to say special thanks to my family and to Thomas for their unrestricted support.

Curriculum Vitae

Name	Theresa Lutz
Date of Birth	16.04.1982
Nationality	German

2007-2010	PhD student in the group of Prof. Dr. Klaus Kern at the Max Planck Institute for Solid State Research in Stuttgart, Germany
2005-2006	Diploma thesis at the Leibniz Institute of Surface Modification in Leipzig, Germany: "Ion Beam Induced Self-Organization on Pre-Patterned Substrates"
2001-2006	Studies of physics at the University of Leipzig
1992-2001	Schiller-Gymnasium, Hof, Germany
1988-1992	Primary School, Hof, Germany